DFT modelling on the effect of manganese in cobalt-based FT-catalysts

Thesis submitted in partial fulfilment for the degree of Master of Science in Engineering in Chemical Engineering at the University of Cape Town

Prepared by:
Yatheshthrao Ragoo
BSc Chemical Engineering (UCT)

Supervisor:
Professor Eric van Steen

Catalysis Institute
Department of Chemical Engineering
University of Cape Town
Private Bag X3
Rondebosch, 7701
South Africa

Keywords: Cobalt catalyst, Manganese promoter, Fischer-Tropsch, Density Functional Theory

May 2022

Plagiarism declaration

I know the meaning of plagiarism and declare that all the work in the document, save for that which is properly acknowledged, is my own. This thesis/dissertation has been submitted to the Turnitin module (or equivalent similarity and originality checking software) and I confirm that my supervisor has seen my report and any concerns revealed by such have been resolved with my supervisor.

Signature: Signed by candidate

Date: 14/08/2022

Acknowledgements

I would like to acknowledge the following individuals and institutions without whom the succesthe s of project would not have been possible.

I would like to express my deepest and sincerest gratitude to Professor Eric van Steen for providing me with the opportunity to join and contribute to your research group. Your guidance and support have been a pillar to the success of this project. Thank you for always having an open door and making time to answer my many ‘qui1-minuteute’ questions. Your constructive feedback and constant encouragement have helped me in becoming a better researchand not to restrain myself to conventional solutions. Thank you for your patience throughout my postgraduate journey.

I would like to thank past and current group members in Prof. van Steen’s group. I would like to thank Tracey van Heerden who has guided me in my early steps of computational quantum mechanical modelling and made time for valuable ‘staircase’ conversations. Many thanks to Vuyisile ‘Vuyi’ Mahlaba, for your friendship, the spontaneous food breaks, and the unorthodox discussions.

I cannot forget my Cape Town family, especially Kappy for always being ears to my rants, the conversations, ice cream trips, and all-around fun.

Additionally, I acknowledge the computational resources provided by the University of Cape Town’s ICTS High Performance Computing facility (HPC) and the Council for Scientific and Industrial Research’s Centre for High Performance Computing (CHPC) for this project. I would like to extend my thanks DST-NFT Centre of Excellence in Catalysis (c*change) for the financial support, which made this research possible.

Last but not the least, I would like to thank my parents who have always sacrificed so much and supported me in all my endeavours. My brother for supporting my unusual plans and ideas since my childhood and for all the extra smiles.

Abstract

The Fischer-Tropsch synthesis (FTS) process can be described as a combination of reactions that convert synthesis gas (essentially CO and H_2) into long chain hydrocarbons (syncrude), which in turn is refined into transportation fuels, lubricants, and other petrochemicals. Among the commercially implemented catalysts such as Fe and Co, the latter is considered as a successful candidate for catalysing FTS reactions towards long chain hydrocarbons (C_{5+}) primarily due to its high activity and longer lifespan. To further drive the selectivity towards longer chain hydrocarbons, manganese may be added to the cobalt-based catalyst as a promoter. To this date, experimental studies have suggested that Mn exists as MnO_x in the working catalyst, and it has been proposed that manganese facilitates the dissociation of CO.

To investigate the promotional effect of Mn, suitable DFT-based MnO_x models were devised on the basis of their formation under Fischer-Tropsch conditions. These were modelled on the Co(111) surface owing to it being amongst the densest surface planes of cobalt. Thermodynamically, the OMn and O_2Mn ligands, are the most likely form of Mn on a Co(111) surface under Fischer-Tropsch conditions with OMn being the ligand present at low ratios of H_2O to H_2 and O_2Mn becoming the dominant species at high conversion.
An essential feature of the Fischer-Tropsch synthesis is the adsorption and dissociation of adsorbed CO and the removal of surface oxygen. The presence of the dominant forms of the manganese complex (OMn and O_2Mn) on Co(111) on these reaction steps was probed. It was found that the presence of OMn on Co(111) stabilised the adsorption of CO further and both the presence of OMn and O_2Mnduces an elongation of the C-O bond in adsorbed CO. The presence of OMn also stabilises the dissociation products, co-adsorbed carbon and oxygen on Co(111), whereas the presence of O_2Mn does not seem to affect the dissociation equilibrium significantly. The presence of these ligands slightly enhances the rate of dissociation of CO by lowering the barrier for CO-dissociation from 2.59 eV on Co(111) to 2.55 eV in the presence of OMn and to 2.37 eV in the presence of O_2Mn. Hence, the presence of MnO_x on Co(111) results in a slightly faster direct CO dissociation than on a clean slab. It should however be noted that the direct CO-dissociation on Co(111) is very slow at typical Fischer-Tropsch conditions, even in the presence of MnO_x ligands. Hence, hydrogen-assisted CO dissociation is typically considered on these dense surfaces. The hydrogen assisted CO-dissociation over Co(111) proceeds with an activation barrier of 0.18 eV. The presence of MnO_x ligands does not seem to facilitate the hydrogen-assisted dissociation based on the pathways considered as elevated barriers were determined.

The disproportionation of surface hydroxyl species was considered as the key reaction for the removal of surface oxygen as water, and the systems involving the precursors of the reaction were compared. The presence of MnO_x ligands on Co(111) offers new pathways for oxygen removal involving hydroxylated surface manganese complexes, i.e., OMn(OH) and O_2Mn(OH), which can act as reactive intermediates in the oxygen removal. A microkinetic analysis shows that the oxygen removal in the presence of O_2Mn on Co(111) was ca. $10^{4.2}$ times faster than in the absence of this ligand under Fischer-Tropsch conditions.

It is thus concluded that manganese as a promoter for cobalt-based catalysts may affect the CO adsorption but may not affect the dominant indirect hydrogen assisted CO-dissociation. The promotional effect of manganese may be related to the oxygen removal from Co(111)

Table of contents

List of tables

List of figures

List of abbreviations

FTS	Fischer-Tropsch Synthesis
DFT	Density Functional Theory
LTFT	Low-temperature Fischer-Tropsch (LTFT)
HTFT	High-temperature Fischer-Tropsch (HTFT)
XAS	X-Ray Absorption Spectroscopy
TEM	Transmission Electron Microscopy
XRD	X-Ray Diffraction
TPR	Temperature Programmed Reduction
STEM-EELS	Scanning Transmission Electron Microscopy and Monochromated-Electron Energy Loss Spectroscopy
TOF	Turnover Frequency
ML	Monolayer
SMSI	Strong Metal-Support Interaction
DRIFTS	Diffuse Reflectance Infrared Transformed Spectroscopy
STEM-EDS	Scanning Transmission Electron Microscopy and Monochromated-Energy-Dispersive X-ray Spectroscopy
TPD	Temperature Programmed Desorption
PBE	Perdew- Burke- Ernzernhof
PW91	Perdew-Wang 1991
RPBE	Revised Perdew- Burke- Ernzernhof
VASP	Vienna Ab-Initio Simulation Package
PAW	Projector Augmented Wave
ZPE	Zero-Point Energy
ads	Adsorbed/adsorption
hcp	Hexagonal closed packed
fcc	Face Centered Cubic
surf	Surface
lig	Ligand

1. Introduction

1.1. Context

Sustainable catalytic conversion of renewable substrates derived from biomass or carbon-containing waste can be readily implemented [1] to manufacture of low-cost transportation fuels [2], and present the sole non-petroleum route to generate platform chemicals for the bulk production of fine and speciality chemicals and polymers [3]. The conversion of biomass into useful chemicals may require its transformation into synthesis gas, either through torrefaction/pyrolysis and gasification or anaerobic digestion and reforming [4]-[5]. Synthesis gas, consisting primarily of CO and H_2, can then be transformed into hydrocarbons via the Fischer-Tropsch process [6].

South Africa is well positioned to develop the Fischer-Tropsch process using synthesis gas from renewable sources, as the Fischer-Tropsch process using coal or natural gas as feedstock was commercialized here to counter the effect of a shortage of imported crude oil during the apartheid era and to this day still caters for local demand [7]. Currently, the PetroSA plant (46000 bpd) and the Secunda plants (144000 bpd) contribute between 25-30% of the local demand for fuels.

To ensure the commercial viability of the Fischer-Tropsch process, the design of heterogenous catalysts with optimum performances for the given process and feed materials is required. The use of cobalt catalysts for the conversion of biomass into liquid fuels using the Fischer-Tropsch process [8]-[9] as well as for the industrial Fischer-Tropsch process is advantageous owing to its ability to catalyse FTS reactions towards long chain hydrocarbons (C_{5+}) primarily due to its high activity and longer lifespan [6]. When combined with a suitable metal oxide such as titania or manganese oxide, the cobalt-based catalyst can offer higher turnover frequencies [9] and a shift of the product selectivity towards C_{5+} hydrocarbons [9]-[10].

While recent studies have started to address the working of promoters which enhances the activity of Co-based catalysts and improved the performance in Fischer-Tropsch synthesis [11]–[13], there is still a grey zone in the nature of manganese promoters. Some experimental work has suggested that manganese exists as oxidic islands with manganese in the +2 oxidation state [11], [14] but there is a lack of theoretical work to support the latter. The use of Density Functional Theory (DFT) is a powerful tool to obtain insights on the nature of promoter on the cobalt surface and how it may impact the performance of cobalt-based catalysts in the Fischer-Tropsch synthesis.

1.2. Fischer-Tropsch synthesis

The Fischer-Tropsch synthesis (FTS) process can be described as a combination of surface reactions that convert synthesis gas (essentially CO and H_2) into long chain hydrocarbons (syncrude), which can subsequently be refined into transportation fuels, lubricants, and other petrochemicals (see Figure 1-1).

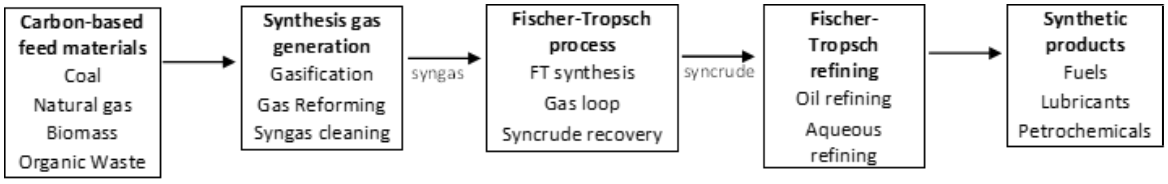

Figure 1-1: Overall schematics of the Fischer-Tropsch process, adapted from [6]

Synthesis gas can be sourced from the gasification of coal, biomass (or organic wastes) or by the reforming of natural gas or biogas. This process is costly and may require substantial investment of up to 70 % of the total cost of the Fischer-Tropsch process. This is primarily accounted in terms of utility infrastructure owing to the low efficiency of the process [6], [15]. Consequently, a thorough assessment of the carbon feed source must be performed despite the low cost of the actual feed component. Among the typical feed source, the production of synthesis gas using gas reforming could be considered to be the cost efficient route given the less demanding feed and waste processing step compared to processing a solid feed such as coal or biomass in a gasifier [6]. It is worth noting that Fischer-Tropsch catalysts are susceptible to poisoning and hence, synthesis gas needs to be cleaned. Using the clean synthesis gas from the generation step, either the low-temperature Fischer-Tropsch (LTFT) or the high-temperature Fischer-Tropsch (HTFT) can be employed for the production of syncrude [7], [16] whereby each output a different range of carbon-based products as shown in Table 1-1.

Table 1-1: Syncrude composition for LTFT and HTFT processes, adapted from [17].

Fischer-Tropsch syncrude property	**HTFT**	**LTFT**
Carbon number range	C_1-C_{30}	C_1-C_{120}
Main product	C_2-C_{10} alkenes	waxes
Normal product phases[a]		
Gases(C_1-C_4)	20-25%	5-10%
Oil	20-25%	15-20%
Wax	0%	20-25%
Aqueous organics	Approx. 5%	1-2%
Water	45-50%[b]	50-55%[b]
Organic compound classes[a]		
Alkanes(paraffins)	20-30%	Major product (>70%)
Cycloalkenes(naphthenes)	<1%	<1%
Alkenes(olefins)	Major product (>50%)	15-20%
Aromatics	1-5%	<1%
Oxygenates	10-15%	Approx. 5%

[a]Percentages are on a mass basis. [b]Closed gas loop, i.e., no net water gas shift conversion

The long-chain hydrocarbons produced in the Fischer-Tropsch synthesis via polymerisation reactions may be accompanied by the water gas shift reactions [18]:

$$2nH_2 + nCO \rightarrow C_nH_{2n} + nH_2O \qquad \textit{Equation 1-1}$$

$$(2n+1)H_2 + nCO \rightarrow C_nH_{(2n+2)} + nH_2O \qquad \textit{Equation 1-2}$$

The products from the Fischer-Tropsch synthesis step are then hydrocracked into diesel, naphtha, lubricants or gaseous products [6]-[7].

1.2.1. Fischer-Tropsch catalysts

It is well documented that selected group VIII transition metal elements constitute the majority of the commercially implemented catalysts. Among those, iron, cobalt, ruthenium and nickel display catalytic activity desirable for industrial-scale implementation [6]. Table 1-2 compares the differences among the available catalysts in terms of price and activities with regards to the reactions in a Fischer-Tropsch reactor. Ruthenium is not used commercially, due to the high cost of the metal as a consequence of its low availability [17]. The use of nickel catalyst is debatable in commercial Fischer-Tropsch plants given its elevated hydrogenation activity which leads to the selective formation of methane and the formation of nickel carbonyls at elevated pressures which leads to catalyst deactivation [17]. Based on the comparison, both iron and cobalt can be used as the catalytically active material in Fischer-Tropsch catalysts. Iron is cheap and can produce more oxygenated wax products. Cobalt is more expensive but, it needs to be replaced less frequently and factoring its high Fischer-Tropsch activity, it is a more profitable option in the long run [17].

Table 1-2: Table comparing the commercially used Fischer-Tropsch catalysts on high surface area oxide supports, adapted from [17]

Active metal	Price	F-T activity	WGS activity	Hydrogenation activity
Ni	Expensive	Low	Low	Very high
Fe	Cheap	Low	Very high	low
Co	Expensive	High	Low	High
Ru	Very expensive	Very high	Low	High

The industrial choice of the catalyst is dependent on the synthesis gas source and the desired products. For synthesis gas with low H_2/CO ratio as obtained in the gasification of coal or biomass, iron-based catalysts are preferred given their water gas shift activity. However, this elevated water gas shift activity will reduce the carbon-efficiency of the process as some carbon will have to be converted to the greenhouse gas, CO_2. The use of cobalt as the catalytically active materials in the Fischer-Tropsch catalyst is better suited for synthesis gas with a H_2/CO of ca. 2 (i.e., closer to the usage ratio) and thus, more suited for synthesis gas generated in a reformer derived from natural gas or biogas. This could be attributed to their higher Fischer-Tropsch activity, particularly at higher conversion, and lower water gas shift activity compared to iron-based catalysts.

The Fischer-Tropsch synthesis is preferably performed at low temperature in the range of 150 to 300 °C . Increasing the reaction temperature shifts the selectivity of the reaction towards methane in the case of cobalt, ruthenium, and nickel while with iron-based catalysts, methane selectivity remains low with the increasing temperatures. While it is favourable to operate the Fischer-Tropsch reactor at lower reaction temperatures, only Ru can drive the reactions at 150 °C with the formation of desirable long chain hydrocarbons.

1.2.2. Catalyst promoters

The catalyst activity and selectivity can be modified by varying process conditions such as temperature, pressure, or feed component ratio. Adjusting catalyst composition and structure may also offer significant improvement in performance [14]. Under instances where modifiers are used to improve the catalytic activity, the nomenclature changes to promoters. Modifiers can also be involved in the performance degradation of the catalyst and in that case, they are referred to as poisons [19]. A synergistic relationship between promoters and poisons is also desirable, particularly for processes yielding different products at different reaction steps but only one product is desired. Together, promoters are added to improve the catalyst activity and the poisons are added to limit undesirable reactions. Hence, high activity and high selectivity can be achieved. By definition, promoters are substances which are added in small quantities to the active catalyst to improve their activity, selectivity or stability. It is important to note that the promoters on their own are not active for the reaction being catalysed [20]. To ensure the relevance for industrial application, the cost and benefit of the promoters must be optimised such that maximum performance can be achieved at the lowest cost, which is typically associated with the amount promoter used [19].

The main classification theme for the promotional effects and in the case of cobalt-based Fischer-Tropsch are as follows:

I. **Structural promoters:** They affect the formation and stability of the catalytically active phase. The work by limiting the agglomeration and sintering of the catalytic metal particles to increase the number of active sites. They also improve the stability of the active sites by influencing metal-support interactions [6], [19].

II. **Electronic promoters:** They affect the electron density on the catalytically active material through the addition and withdrawal of electron density near the Fermi level of the valence band, thereby inducing ligand effects. These changes in electronic environment can lead to changes in turnover frequency and product selectivity. The can also limit the re-oxidation of the metal nanoparticles and induce enhanced stability against catalyst deactivation [6], [19].

III. **Synergistic promoters:** They can be considered as catalytically active promoters whereby they affect the behaviour of the catalytically active material leading to shifts in the overall product distribution [6], [19].

1.2.2.1. Promoters for cobalt-based Fischer-Tropsch catalysts.

Catalyst activity, selectivity and stability are affected by the kind of promoter element used. Table 1-3 provides a summary of various promoters used with cobalt-based Fischer-Tropsch catalysts. The amount of the promoter elements, the reaction conditions and the catalyst preparation method all have an important role in the definition of the promoter effect. Hence, promoter characteristics may vary as a result of these factors, leading to changes in catalytic activity, selectivity and stability [17]. The amount of promoter on the catalytically active site can also have an impact on the adsorption characteristics. For example, if large quantities of an oxide promoter are present on the active metal surface, active sites on the surface may become inhibited and impede catalytic activity. Promoters present a variety of chemical characteristics that can influence cobalt-based Fischer-Tropsch synthesis. For example, certain transition metal oxides have been shown to exhibit characteristics as water gas shift reagent. Promoters can influence hydrogenation and dehydrogenation processes; they can alter the ratio of hydrocarbons produced during reactions. Promoters can also extend the lifespan and efficiency of catalysts as they can minimize the effect of sintering on supported catalyst clusters[17].

Table 1-3: Summary of promoter elements commonly used in cobalt-based Fischer-Tropsch catalysts and promotional mode, adapted from [17]

			Influence on catalyst		
Promotion type	**Elements**	**Promotional mode**	**Activity**	**Selectivity**	**Stability**
Structural	Mg, Si, Zr, Nb, Rh, La, Ta, Re, Pt	Support stabilisation	+		+
	B, Mg, Zr	Cobalt gluing	+		+
	Ti, Cr, Mn, Zr, Mo, Ru, Rh, Pd, Ce, Re, Ir, Pt, Th	Cobalt dispersion increase	+		+
Electronic	B, Mg, K, Ti, V, Cr, Mn, Zr, Mo, La, Ce, Gd, Th	Decorating cobalt surface	+	+	+
	Ni, Cu, Ru, Pd, Ir, Pt, Th	Cobalt alloying	+	+	+
Synergistic	B, Mn, Cu, Ce	Water gas shift	+	+	
	Pt	Hydrogenation/ dehydrogenation		+	
	Ni, Zr, Gd	Coke burning			+
	B, Mn, Zn, Zr, Mo	H_2S adsorption			+

Noble metals such as ruthenium, rhenium and platinum are the most researched and widely used structural promoters for cobalt-based Fischer-Tropsch primarily due to their ability to improve the reducibility of cobalt. Thus, providing more active sites for the reactions [21]–[23]. Ruthenium has been shown to display both electronic and structural promotion characteristics. In comparison to the other promoters, ruthenium promoted catalysts generally exhibit a higher selectivity for C_{5+} hydrocarbons; addition of small amount of the promoter to either unsupported or supported cobalt-based catalysts enhances the turnover frequency. Peak catalytic activity has been reported when the Ru/Co ratio is less than 0.008 [24]. Both ruthenium and rhenium can act as structural promoters. They have been shown to improve the reducibility of cobalt through hydrogen spillover and thereby improving the dispersion of the cobalt nanoparticles [25]-[26]. The addition of rhenium has been shown to improve Fischer-Tropsch activity but site-specific activity remains unchanged [17]. Rhenium may affect the Co particle size distribution which may indirectly shift the product selectivity due to the changes in the Co surface density [17], [25]. While platinum can be considered as a structural promoter, its application as reduction promoter has been well established whereby it can aid in the dispersion of the cobalt nanoparticles [21] by improving the reducibility of Co_3O_4 to Co at lower temperatures [17]. The addition of platinum is not restricted to reduction performance but has also been reported to improve overall Fischer-Tropsch performance [26] with reported higher turnover frequencies [27]. It should be noted that reduction of cobalt is dependent on the magnitude of metal support interaction, and thus, it can be speculated that these promoters may also influence the support material [28].

Other promoters that have been studied for cobalt-based catalysts include lanthanum, magnesium, niobium and zirconium [17]. Lanthanum has been coupled with cobalt supported on γ-alumina whereby it improves catalytic activity and selectivity towards heavy hydrocarbon in comparison to an unpromoted catalysts . But it is worth noting that the latter will be dependent on reactor conditions [29]. Lanthanum has also been shown to prolong the lifetime and enhance activity of the catalyst as it alters the chemical structure of the support material [30]. Magnesium promotion has also been linked to cobalt-catalysts supported on alumina whereby reduces the formation of the metallic cobalt phase but instead, leads to the formation of mixed metal oxides such as MgO-CoO. Improvement in the catalytic activity was observed at low loading of Mg and as the amount of the latter was increased, catalyst reduction was impaired due to the formation of the mixed oxide phase [31]. Niobium promoters has been shown to affect the CO hydrogenation activity of cobalt-based Fischer-Tropsch catalyst supported on alumina [32]. The use of zirconium promoter improves the catalytic efficiency of alumina supported Co catalyst. Enhanced synthesis of $-CH_2-$ intermediates results in increased selectivity of for long chain hydrocarbons. In addition to enhanced catalytic activity, improvement in the reducibility of cobalt can be attributed to the presence of zirconium[33].

Although transition metal oxides are primarily thought of as electronic promoters, they can also display synergistic or structural functions [20]. They tend to be dispersed over the surface of active metal surface thereby, altering the active sites on the surface. This behaviour can, hence, affect the adsorption characteristics of the catalyst. It should be noted that in the circumstance that the concentration of these oxides exceeds 1 ML, it can inhibit the active sites leading to a decrease in catalyst activity [17].

1.2.3. Manganese promoter on Co-based catalysts

Manganese has been investigated as promoter in Fe, Ru and Co-based Fischer-Tropsch catalyst. For iron-based applications, manganese has been used to enhance the production of olefins in the C_2-C_5 range. Xu et al. [34] suggested that in addition to the production of light olefins, Mn as MnO improves the ability and capacity of the catalysts to adsorb CO and CO_2. The enhanced production of light alkenes in Fe-based catalysts has also been attributed to the ability of the Mn promoter to decrease the particle size of the iron oxide precursor [35].

Manganese promotion in ruthenium-based catalysts results in an increase in the formation on alkenes and a shift in the product distribution towards longer chains [36]. However, the catalyst performance may also be affected by the coverage of the catalytically active surface by the promoter. The manganese monolayer generated by Cornils et al. [20] on top the Ru surface was shown to restrict the adsorption of CO since the active sites are occupied by the promoter. Mn has also been shown to act as a structural promoter in Ru-based catalyst whereby it boosts dispersion of the metal nanoparticles on the support [20].

Early experimental studies on manganese promotion on Co-based catalysts supported on TiO_2 by Morales [17] showed that manganese is present in the passivated catalyst in the form of MnO_2 and in the reduced catalyst in the form of MnO. From the combination of XAS, TEM, XRD and TPR measurements, it was deduced that MnO decreases the reducibility of cobalt and lead to the formation of cobalt crystallites with larger particle sizes (>5nm). Manganese was also found to alloy with the cobalt particles in the form of a solid solution with a rock salt structure. In terms of catalytic performance, Mn as MnO lowered CH_4 selectivity, increased hydrogenation activity reflected by an increase in turn over frequency and enhances the catalyst stability.

MnO remains close to the cobalt particles supported on carbon after reduction as evidenced from XPS and STEM-EELS data [37] because carbon as support material lacked sites with significant interaction with MnO. From TPR data, it was shown that the promoter suppresses both the hydrogen chemisorption and cobalt reducibility even at very low MnO loadings. On the other hand, at a loading of 0.3 wt% and higher under low pressure condition (1 bar), there was a significant increase in selectivity of C_{5+} hydrocarbons. Increasing the pressure to 20 bar only offered a slight improvement in selectivity of longer chain hydrocarbons for a Mn loading of 0.03 wt%. Any further increase in the loading of the promoter resulted in detrimental performance with a significant decrease in selectivity for the formation of C_{5+} hydrocarbons from 78 wt% to 52 wt%. Similar trends were observed in terms of turnover frequency, whereby an increase in TOF by 20 % was reported at 1 bar and, 130 % at 20 bar respectively at low manganese loading. At higher loading, a decrease in activity was reported since the active catalyst sites were blocked by the promoter. Hence, it was suggested that the role Mn as MnO could involve the regulation of the hydrogenated process.

Structurally, the presence of manganese as MnO in cobalt-based catalysts supported on titania, impairs the reducibility of cobalt [17] as cobalt and manganese oxide tend to be closely associated together [38]. Hence, this interaction results in a drastic reduction in the cobalt particle size from 24 nm to 11-14 nm. At high manganese loading (>2.15 wt%), hydrogen chemisorption is substantially suppressed in the $Co/Mn/TiO_2$ system due to the coverage of the catalyst active site by TiO_x and MnO species. Nevertheless, at moderate loading, manganese appears to enhance the availability of Co_0 surface, probably by minimising strong-metal support interactions (SMSI) between cobalt and the titania support and thus, boosting catalytic activity. DRIFTS using CO and H_2 as probe molecules showed that the MnO tightly bound to cobalt functions as an electronic promoter during Fischer-Tropsch reactions on the Co_0 surface; Mn^{2+} depletes the electron density of the Co_0 sites, resulting in a comparatively higher concentration of linearly bound CO. Consequently, the hydrogenation rate is reduced favouring the production of additional olefins. This effect can be then translated to shift towards C_{5+} hydrocarbons. The presence of manganese in the catalyst system also led to an increased production of carbonate species during Fischer-Tropsch reaction and thus, it can be implied that MnO may promote the water-gas shift reaction, converting CO to CO_2. Therefore, influencing the catalyst performance.

Manganese is an effective promoter for increasing the activity and selectivity of Co-based Fischer-Tropsch. With the limited understanding behind the mechanism of the promotional effects, a recent study by Johnson et al. [39] addressed the topic by investigating Mn promotion on the activity and selectivity of Co/SiO_2 catalyst on Fischer-Tropsch reactions rate kinetics and STEM-EDS. A single, two parameter rate expression was used to described Fischer-Tropsch kinetics as a function of Mn/Co ratio, temperature, and reactant partial pressure. The presence of the promoter was shown to increase the overall rate constant as well as the kinetic parameter typically representing the strength of adsorption of CO under Fischer-Tropsch conditions. These observations were further supported by temperature-programmed desorption (TPD) measurements on CO desorption. STEM-EDS experiments indicated that the promoter accumulates preferentially on the surface of Co nanoparticles up to a Mn/Co ratio of 0.1 and can result in shift in product selectivity with increasing loading. At higher loadings, manganese rather accumulates as MnO nanoparticles which accumulates on the silica support. Manganese has also been observed to be extensively distributed on the cobalt nanoparticles as MnO with increase manganese loading, Figure 1-2 [A]. whereby Mn is in the +2-oxidation state. In contrast to the structural effects reported by Morales [17], [38], Johnson [39] did not observed a change in the cobalt particle size due to MnO promotion. Lastly, in-situ IR spectra of adsorbed CO showed that MnO increases the amount of adsorbed CO with weakened C-O bonds. It was suggested that Lewis-acid based interactions between the Mn^{2+} cations situated at the edge of the MnO islands and oxygen in the CO adsorbed, enhances the cleavage of the C-O bond (see Figure 1-2 [B]). Lastly, it was suggested that the observed reduction in selectivity towards CH_4 and the shift in selectivity towards C_{5+} hydrocarbons was attributed a decrease in the ratio of adsorbed H to CO ratio on the surface of the supported Co nanoparticles.

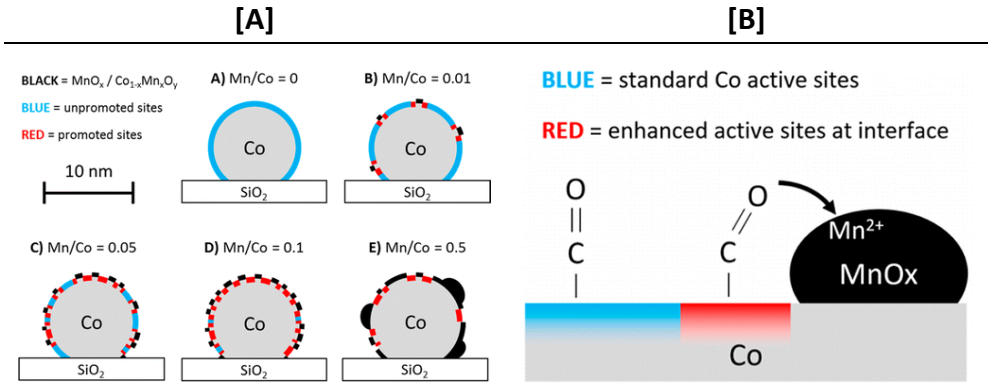

Figure 1-2: Schematics of the distribution of Mn on the active cobalt catalyst. [A] 2D cross sections of Co nanoparticles with the deposition of Mn and MnOx with increasing Mn/Co ratio. [B] Representation of the Lewis-acid base interaction between Mn^{2+} cation and adsorbed CO. Images taken from [39]

Despite the increasing number of experimental investigations that have been conducted to examine the effects of MnO on cobalt catalysts, only a limited number DFT-based theoretical studies have been published. Pedersen et al. [11] incorporated both an experimental and theoretical approach to understanding manganese promotion for Fischer-Tropsch. To broaden the insight on promotion of cobalt-based Fischer-Tropsch with manganese, a DFT model was generated to assess the adsorption of the different species present under Fischer-Tropsch conditions and, to understand the impact of manganese on CO dissociation. The unpromoted slab was modelled as a 5-layer p(2x2) Co(111) slab with the bottom 2 layers fixed, Figure 1-3 [A].For the promoter slabs, a manganese monolayer was added as a top monolayer(Mn/Co), Figure 1-3 [B] and as a subsurface monolayer (Co/Mn/Co), Figure 1-3 [C] while maintaining the total number of layers and slab size. The latter have been shown to stabilise the adsorption of Fischer-Tropsch species on the metal surface. This was given by an increasein the calculated adsorption energies of the species with the exception CH_4 whereby an adsorption energy of -0.02 eV was obtained on all systems. The dissociation of CO was more facile in the promoted models with the monolayer model (Mn/Co) resulting in the lowest barriers. The increased barriers for CH_3 and CH_4 formation on the promoted slabs can be translated to an inhibited hydrogenation activity and hence, can be linked to shift in selectivities for olefins, C_{5+} and CH_4 in the presence of Mn. But the relevance of the models and reported results are questionable as XPS results from the experimental study suggest that manganese exists as Mn^{2+} on the active metal surface. Therefore, indicating that MnO or a mixed oxidic form of containing manganese may be present rather than metallic manganese.

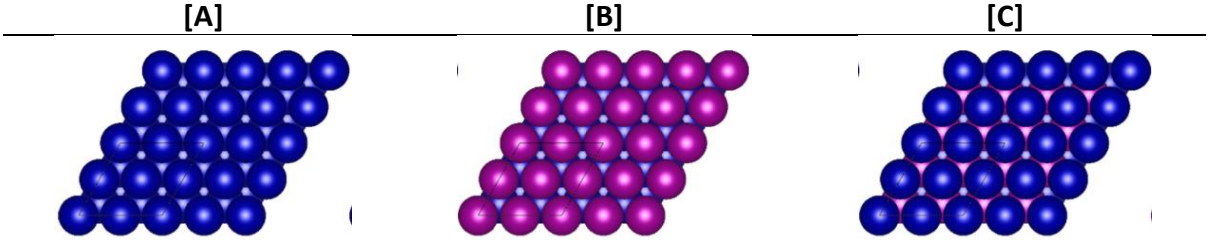

Figure 1-3: Top view of the different Co-based models used for DFT calculations, blue atom represents cobalt and purple atom represent manganese. Taken from [11]

Doorslaer [40] and Gençoğlu [41] investigated the effect of manganese promoters in the oxidic form on Co-based Fischer-Tropsch catalysts using DFT. The ring structure comprising of 6-MnO units by Doorslaer [40] was found to be the most stable ring structure of MnO on the Co(111) surface (see Figure 1-4 [A]). The effect of Mn promotion on the kinetics of CO and H_2O dissociation was assessed by co-adsorbing CO, H, OH and H_2O with the ring structure on the active metal catalyst. The presence of the promoter ring had negligible effect on the adsorption strength of CO on the Co(111) surface as shown by a decrease in adsorption energy from -1.38 eV to -1.35 eV. The adsorption strength of H and OH, faced a significant decrease in proximity of the promoter while the opposite was noted for the adsorption of H_2O. The significant stabilisation of the adsorption of H_2O was associated with the assimilation of the species inside the ring structure. With H_2O adsorption preferred over H and OH, Doorslaer [40] suggested that H_2 dissociation will be unfavourable thereby decreasing the amount of hydrogenating species on the surface.

Gençoğlu [41] considered a linear MnO configuration as shown in Figure 1-4 [B] as basis to investigate the adsorption of Fischer-Tropsch species and the energetics of CO dissociation. Amongst all the adsorbate considered (C, O, H, CO, CH, OH, CH_2, H_2O and C_2H_2) only H and C_2H_2 had their adsorption stability reduced in the presence of the oxide promoter. But it should be noted that the adsorption stability will be dependent on the MnO coverage. The barrier for CO dissociation in the presence of the MnO was found to increase by 0.71 eV for direct pathway and 0.45 eV for the H-assisted pathway. On the other hand, the barrier for the formation of the CH and HCO precursor of the H-assisted dissociation was minimised in the presence of the MnO monomer. Hence it could be suggested the MnO promoter does not promote the direct dissociation of CO. Instead, the activity increase reported in literature due to Mn promotion can be linked to H or OH assisted CO dissociation pathway or another rate limiting step.

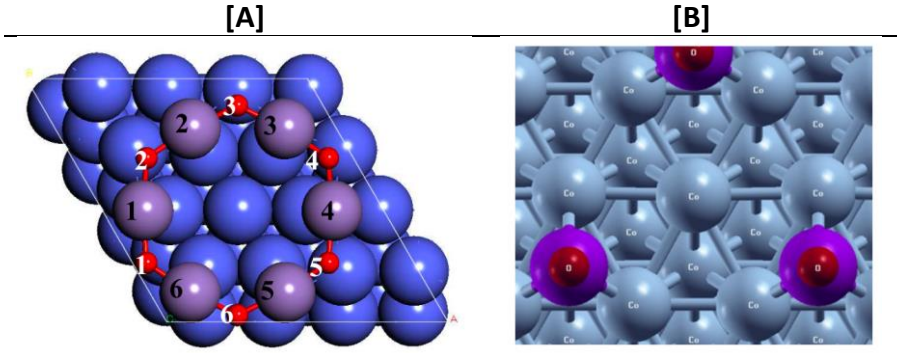

Figure 1-4: DFT-based MnO models on Co(111). [A] 6-MnO ring by Doorslaer [40]***. [B] Linear MnO model by Gençoğlu*** [41]

1.3. Defining the project

1.3.1. Problem statement

Cobalt-based Fischer-Tropsch catalysts are the most desirable commercial catalyst for CO hydrogenation due to their high activity at high conversion and high selectivity towards C_{5+} hydrocarbons. The use of promoters such as Mn in cobalt-based Fischer-Tropsch have gained significant interest since they can lead to changes in catalytic activity, selectivity, and stability.

Early studies suggested that the enhanced activity and selectivity in manganese promoted Co catalyst could be attributed to the promoter affecting the Co particle size, stipulating a structural promotion. But inconsistencies on the effect of manganese promotion on cobalt particle sizes could be noted. A recent publication involving manganese promotion did not report significant change in cobalt particle size, but instead suggested that manganese may instead be acting as an electronic promoter [39]. At high loading (Mn/Co ratio > 0.1) manganese accumulates as MnO nanoparticles and it was suggested to act as a Lewis-acid, whereby it depletes the electron density from the Co surface active sites. This would lead to the increase in linearly adsorbed CO molecules, an effect which could be translated to a shift towards C_{5+} hydrocarbons [40]. With the kinetic study by Johnson et al. [41], the presence of the promoter was shown to increase the overall rate constant as well as the kinetic parameter typically associated with the strength of adsorption under Fisher-Tropsch conditions. A follow up TPD study was performed whereby higher CO desorption temperature was reported and in-situ IR experiments revealed an increased amount of adsorbates with weakened carbonyl stretching frequencies on manganese promoted cobalt surface. But conclusions could not be reached whether this weakening effect is the determinant in improving Fischer-Tropsch activity.

Theoretical work has been undertaken in an attempt to model manganese promotion and comprehend the mechanism underlying manganese promotion of cobalt-based catalysts. An initial challenge of establishing the state of the catalytically active metal was present. Pedersen et al. [11] modelled Mn as a monolayer either on top of the Co surface or between Co layer. Although improved CO adsorption and CO dissociation barriers were observed, the models had to be abandoned because XPS results from the experimental study revealed that Mn exists as Mn^{2+} on the active surface. Therefore, indicating that MnO or a mixed oxidic form of containing manganese may be present and dismissing the validity of the model. Follow-up studies by Doorslaer [40] and Gençoğlu [41], modelled Mn as MnO structures on the cobalt surface in particular Co(111). While improvements in the adsorption strength of CO on the Co(111) surface and slight reduction in the CO dissociation barrier were observed, the results were not sufficient to explain the mechanism by which manganese improves Fischer-Tropsch synthesis activity. Factoring that Co(111) is among the densest surface planes in the cobalt fcc phase, this study will devise a suitable manganese oxide model that can describe the electronic promotional effect and investigate the possible mechanisms that lead to improved Fischer-Tropsch activity.

1.3.2. Objectives

Based on literature, the following objectives have been set:

I. Develop a surface model of the MnO_x promoter on the active metal catalyst.
II. Identify stable MnO_x complexes under Fischer-Tropsch conditions.
III. Evaluate the effect of viable MnO_x models on the adsorption of key Fischer-Tropsch reactants, intermediates, and products.
IV. Assess the impact of the promoter on the dissociation of CO.
V. Assess how the changes in activation barriers will translate to the rate of CO dissociation.
VI. Assess the impact of the promoter on the oxygen removal.
VII. Assess how the changes in activation barriers will translate to the rate of oxygen removal.

1.3.3. Hypothesis

From the objectives and reviewed literature, it can be hypothesised that Mn will be present in the oxidic state (MnO_x) on the catalytically active surface and will affect the strength of adsorption on CO, its rate of dissociation and the rate of oxygen removal as water.

1.3.4. Key questions

To test the above hypotheses, the following questions will serve as guide:

I. Will the oxidation state defined in literature guide the setup process for the MnO_x complexes?
II. For MnO_x complexes to be investigated, which configuration will be more stable or feasible under experimental scenarios?
III. What are the typical range of H_2/H_2O partial pressure under Fischer-Tropsch operating temperature and pressure?
IV. What are the key species involved in Fischer-Tropsch?
V. What are the likely pathways for CO dissociation and oxygen removal on the cobalt surface?
VI. What are elementary step reactions for CO dissociation and oxygen removal?

2. Computational methods

2.1. Introduction

Ab-initio computational methods can be used to predict molecular geometries, calculate molecular energies, identification of reaction intermediates, visualisation of orbitals structures, IR, UV, NMR spectra, chemical reactivity, and translate these into physical properties of different species/materials [42]. Classical mechanics involved in the trajectories of particles can be calculated theoretically by using initial conditions and Hamiltonian structure of electrons encompassing the kinetic and potential energies of a system:

$$\hat{H} = \hat{T} + \hat{V} \qquad \textit{Equation 2-1}$$

- $\hat{H}$ Hamiltonian operator
- $\hat{T}$ Kinetic energy operator
- $\hat{V}$ Potential energy operators

The formalism of the Schrödinger's wave mechanics, allows the behaviours of particles to be estimated using wavefunctions(ψ) and thereby the total energy of a system [43]. The Hamiltonian can hence be rewritten as the time independent Schrödinger equation (TISE):

$$\hat{H}\psi = \hat{T}\psi + \hat{V}\psi \qquad \textit{Equation 2-2}$$

- $\hat{H}$ Hamiltonian operator
- ψ Wavefunction
- $\hat{T}$ Kinetic energy operator
- $\hat{V}$ Potential energy operators

Which can effectively be reduced to:

$$\hat{H}\psi = E\psi \qquad \textit{Equation 2-3}$$

- $\hat{H}$ Hamiltonian operator
- ψ Wavefunction of system
- E Total energy of the system

2.1.1. Born-Oppenheimer (BO) Approximation

For a many-body quantum chemical system, the Hamiltonian can be expressed in terms of electron-electron, electron-nuclei and other cross interactions as described by Equation 2-5 [44]. The first term represents the kinetic energy of the nuclei ($\hat{T}_n$), the second term the kinetic energy of the electrons ($\hat{T}_e$), the third term the potential energy of coulombic nuclei-nuclei interaction ($\hat{V}_{n-n}$), the fourth term the potential energy of coulombic electron-electron interaction ($\hat{V}_{e-e}$), and the last term the potential energy of coulombic nucleus-electron interaction ($\hat{V}_{n-e}$).

$$\hat{H} = \hat{T}_n + \hat{T}_e + \hat{V}_{n-n} + \hat{V}_{e-e} + \hat{V}_{n-e} \qquad \textbf{Equation 2-4}$$

where the Hamiltonian can be expanded in terms of partial derivatives as follows:

$$\hat{H} = -\sum_{I} \frac{\hbar^2}{2M_I} \nabla^2_{\mathrm{R_I}} - \sum_{i} \frac{\hbar^2}{2m_e} \nabla^2_{\mathrm{r_i}} + \frac{1}{2} \sum_{\substack{I,J \\ I \neq J}} \frac{Z_I Z_J e^2}{|R_I - R_J|} + \frac{1}{2} \sum_{\substack{i,j \\ i \neq j}} \frac{e^2}{|r_i - r_j|} - \sum_{I,i} \frac{Z_I e^2}{|R_I - r_i|} \qquad \textbf{Equation 2-5}$$

I, J	Indexes on nuclei
i, j	Indexes on electrons
R_I	Positions of nuclei
r_i	Positions of electrons
M_I	Masses of nuclei
m_e	masses of electrons
Z_I	Atomic number of nuclei I

The partial derivative terms ($\nabla^2_{\mathrm{R_I}}$ and $\nabla^2_{\mathrm{r_i}}$) add a level of complexity to solving Equation 2-5 thereby it can only be solved for simple systems such as a hydrogen atom or an H_2^+ molecular ion. To solve Equation 2-5 for a molecular system, electronic structure approximations need to be considered. Among those is the Born-Oppenheimer(BO) approximation [44], whereby electrons are considered to be able to move more easily compared to nuclei. This is because the model factors that a nucleus has a much greater mass than an electron (mass of proton is 1836 times that of an electron) and thus, the nucleus can be considered immobile. The electronic structure can then be considered as an electron cloud surrounding stationary nuclei.

Hence, with the BO approximation, the total wavefunction of the time independent Schrödinger equation can be expressed as a product of the nuclei ($\psi_n(R)$) and electronic ($\psi_e(r,R)$) wavefunctions under Equation 2-6. It should be noted that the nuclei wavefunction is only dependent on the nuclei position while the electronic wavefunction factors in both positions of electrons and nuclei.

$$\psi(r,R) = \psi_n(R)\psi_e(r,R) \qquad \textbf{Equation 2-6}$$

Similarly, the time independent Schrödinger equation can be reformulated in terms of nuclei (E_n) and electronic energy (E_e) to evaluate the total energy (E) of a system as follows:

$$E = E_e + E_n \qquad \textbf{Equation 2-7}$$

$$\widehat{H}_n(R)\psi_n(R) = E_n\psi_n(R) \qquad \textbf{Equation 2-8}$$

$$\widehat{H}_e(r,R)\psi_e(r,R) = E_e\psi_e(r,R) \qquad \textbf{Equation 2-9}$$

2.1.2. Hartree-Fock Theory

Although the Born-Oppenheimer approximation simplifies the Hamiltonian by introducing nuclei and electronic wavefunctions, it is still a challenge to solve the time independent Schrödinger equation owing to the multi-electron nature of a many-body quantum chemical system. The Hartree-Fock (HF) Self-Consistent Field (SCF) method, based on a modification of the variational principle, overcomes this limitation by approximating the electronic wavefunction of an n-electron system by the product of n anti-symmetric single-electron(fermion) wavefunctions:

$$\psi_e(r) = \prod_n \psi_{e,n}(r_n, R_n) \qquad \textbf{Equation 2-10}$$

This simplification method takes into account the Pauli exclusion principle whereby two electrons cannot occupy the same quantum state and thus the single wavefunction can be evaluated via a Slater determinant [45]. However, the HF method considers a mean-field environment whereby each electron interacts within an average electrostatic field of other electrons and any effect arising from deviations of the latter are neglected [46], [47]. By ignoring these electron correlation effects and the associated energy, Equation 2-11, an important flaw can be linked to the HF method thereby resulting in inaccurate energies for many-body quantum chemical systems.

$$E_{correlation} = E_{exact} - E_{HF} \qquad \textbf{Equation 2-11}$$

Performance parameters are crucial when using *ab initio* methods to solve for a particular property of a system. Among these is a scaling factor based on the number of basis functions used in the calculation (N). The HFSCF method scales with N^4 [48], so doubling the number of electrons will result in each iteration taking 2^4 times as long.

2.2. Density Functional Theory

The requirement for *ab initio* methods which can account for correlation effects with lower computational cost (N scaling factor) has led to the development of alternatives to the HF method. Modern Density Functional Theory (DFT) was developed to determine the properties of many-body quantum chemical systems by using functionals of the spatially dependent particle density $n(r)$ to replace many-electron wavefunctions [49], [50]. It was based on the theorems by Hohenberg and Kohn and the method by Kohn and Sham. By defining any property of a system as a functional of particle density, and thereby knowing the ground state density, we can equate the argument to knowing the wavefunctions for the ground state and all the excited states.

There are several computational methods available to evaluate DFT calculations. Some of the common packages are: Vienna Ab-initio Simulation Package (VASP) [51]–[54], Cambridge Sequential Total Energy Package (CASTEP) [55]and SIESTA [56], each having different advantages over each other depending on the type of systems being investigated. Nevertheless, they all share the same Kohn-Sham [3] formalism with the Hohenberg and Kohn theorems [2] and the Born-Oppenheimer approximation [44] as basis.

2.2.1. The Hohenberg–Kohn (HK) Theorems

The paper published by Hohenberg and Kohn in 1964 [2], brought two theorems to describe the ground state energy. The Hohenberg–Kohn(HK) theorems are based on the Thomas-Fermi [57], [58] model, which identified the electron density as a key parameter in calculating a system's total energy. Thereby, eliminating operation on a 3N-dimentional wavefunction. Instead, independent particle wavefunctions based on scalar functions of $n_0(r)$ in 3-dimentions can be used to define a system completely.

Theorem 1:

From the BO approximation, electron and nuclei contributions are typically considered separately. The coulombic potential arising from the nuclei are isolated as an external potential V_{ext}(all $v_{ext}(r_i)$ contributions) in which all electrons relax in their ground state while the ionic kinetic and self-interaction potential energy considered separately. Consequently, the Hamiltonian under Equation 2-5, can be re-written as:

$$\widehat{H} = -\sum_i \frac{\hbar^2}{2m_e}\nabla_{\mathrm{r_i}}^2 + \frac{1}{2}\sum_{\substack{i,j \\ i\neq j}} \frac{e^2}{|r_i - r_j|} + \sum_i v_{ext}(r_i) \qquad \textit{Equation 2-12}$$

When $v_{ext}(r)$ is defined, the Hamiltonian of the system is fully defined including all state wavefunctions in the ground and excited state. It can be inferred that all properties of the system are uniquely determined by the electron density functional of ground state. Hence, it was theorised that in any system of interacting particles, the external potential $v_{ext}(r)$ except for a constant is uniquely determined by the ground state particle density $n_0(r)$.

Theorem 2:
For any $v_{ext}(r)$, we can define a functional for the energy $E[n(r)]$ in terms of particle density. There also exists a universal functional $F[n(r)]$ of the density, independent of $v_{ext}(r)$. It was theorised that the global minimum of the energy functional with respect to variations $n(r)$ is the exact ground state energy of the system and the exact ground state density $n_0(r)$ minimises the functional. Consequently, the exact ground state energy and density can be fully determined by the energy functional for some arbitrary external potential $E_{v_{ext}}[n(r)]$, as follows:

$$E_{v_{ext}}[n(r)] \equiv \int n(r)v_{ext}(r)dr + F[n(r)] \qquad \textit{Equation 2-13}$$

Although the HK theorems introduced the $n(r)$ as basic variable, it is impossible to calculate any property of a system, yet the energy, because the universal functional $F[n(r)]$ is unknown.

2.2.2. The Kohn-Sham (KS) Equations

The Kohn-Sham (KS) method [50]attempts to reduce the complexity of the many-electron Hamiltonian, Equation 2-12, into a single Slater determinant of one-electron wavefunction. This effectively maps an interacting system onto a non-interacting fictitious system whereby electron move in an effective single-particle potential $v_{eff}(r)$. The independent particle equation is given by:

$$\left(-\frac{\hbar^2}{2m}\nabla^2 + v_{eff}(r)\right)\phi_i(r) = \varepsilon_i\phi_i(r) \qquad \textit{Equation 2-14}$$

Where $v_{eff}(r)$ is the KS potential, denoting the effective external potential in which no-interacting particles move. $\phi_i(r)$ is the KS orbital function (independent particle orbital). $\varepsilon_i$is the eigenvalue of corresponding Kohn–Sham orbital, evaluated via Equation 2-15 (Kohn-Sham energies as a function of occupation numbers) [59].

$$\frac{\delta E}{\delta n_i} = \varepsilon_i \qquad \textit{Equation 2-15}$$

For a system with N electrons, the ground state would consist of the N lowest energy orbital, and thus the density can be evaluated by summing the contributing of each orbital:

$$n(r) = \sum_i^N |\phi_i(r)|^2 \qquad \textit{Equation 2-16}$$

The KS potential $v_{eff}(r)$ can be expressed as Equation 2-17 where, we can note the exchange-correlation potential $v_{xc}(r)$ that accounts for all the many-body quantum mechanical effect encompassing exchange and correlations. To solve for the simultaneous equations required for the independent particle equation, the $v_{eff}(r)$ and $n(r)$ terms need to be constained such that they are consistent. This is done by changing $v_{eff}(r)$ to achieve self-consistency via Equation 2-17. The effective potential is calculated by considering the variation of a the exchange-correlation potential $v_{xc}(r)$ with respect to particle density. Consequently, we can reformulate $v_{xc}(r)$ to a variation of the total energy functional with respect to particle density, Equation 2-18.

$$v_{eff}(r) = v_{ext}(r) + \int \frac{n(r')}{|r - r'|} dr' + v_{xc}(r) \qquad \textit{Equation 2-17}$$

$$v_{xc}(r) = \frac{\partial E_{xc}[n]}{\partial n(r)} \qquad \textit{Equation 2-18}$$

The exchange-correlation energy $E_{xc}[n]$, is comprised of 4 contributions: 1) a coulombic functional, 2) an exchange functional, 3) a correlation functional and 4) a kinetic functional. It can be quite a challenge to approximate each component separately and therefore, a good approximation (either a local or semi-local functional) of $E_{xc}[n]$ will be required to define the density functional.

It is worth noting that in addition to the approximation of $E_{xc}[n]$, the eigenvalue term of Equation 2-15 needs to be solved iteratively (via the definition of particle densities) until an optimum self-consistency is achieved. Thereby translating to a compuational taxing step prior to solving for the modified hamiltonian.

2.2.3. Approximation of exchange-correlation (XC) functionals

2.2.3.1. Local Density Approximation (LDA)

Local Density Approximation (LDA) is amongst the simplest approximations which can describe the exchange-correlation function $E_{xc}[n]$ accurately. The method was initially proposed by Kohn-Sham in 1965 [50] but we can trace its origins to the Thomas-Fermi model [57], [58] where the latter suggests that the ground state of a Homogeneous Electron Gas (HEG) is a function of electron density alone. LDA assumes a homogenous density irrespective of particle position and hence exchange-correlation energy of each particle can be written as:

$$E_{xc}^{LDA}[n] = \int n(r)\varepsilon_{xc}(n(r))\,dr \qquad \textit{Equation 2-19}$$

The LDA-based exchange correlation energy can be further simplified into an exchange term and a correlation term, Equation 2-20. For a system approaching the HEG limit, exchange energy term ($E_x^{LDA}[n]$) based on the Dirac exchange can be reformulated as per Equation 2-21.

$$E_{xc}^{LDA}[n] = E_x^{LDA}[n] + E_c^{LDA}[n] \qquad \textit{Equation 2-20}$$

$$E_x^{LDA}[n] = -\frac{3}{4}\left(\frac{3}{\pi}\right)^{\frac{1}{3}} \int n(r)^{\frac{4}{3}}\,dr \qquad \textit{Equation 2-21}$$

On the other hand, the correlation energy ($E_c^{LDA}[n]$) is still a challenge whereby it can be found in the low- and high-density limits (corresponding to infinitely-weak and infinitely-strong correlation) [60] and no explicit equations can be derived. For intermediate densities, Quantum Monte Carlo (QMC) simulations [61] data need to be fitted to obtain the correlation energy term.

2.2.3.2. Generalised Gradient Approximation (GGA)

The LDA approach does not come without its drawbacks: 1) underestimation of the exchange energy and 2) overestimation of the correlation energy [62]. The Generalised Gradient Approximation (GGA) was hence, introduced to account for the inhomogeneity when describing real particle densities. It accounts for both the particle density and a density gradient to describe the exchange energy term ($E_{xc}^{GGA}[n]$), Equation 2-22. Therefore, we can obtain better description of molecular geometries and ground state energies over LDA. An example could be inhomogeneous systems like molecules, and the GGA approach improves on the accuracy in determining binding energies. The GGA approach tends to favour non-uniform densities more than LDA and thereby leading to bond softening, an effect that sometimes corrects or can even overcorrect LDA predictions [63].

$$E_{xc}^{GGA}[n] = \int n(r)\, \varepsilon_{xc}(n(r), \nabla n) dr \qquad \textit{Equation 2-22}$$

With the aim of further reducing the error of exchange term of the exchange-correlation energy, several GGA-functions have been introduced. These include PBE [63], PW91 [64] or RPBE [65] each minimising the underestimations to some extent to allow better system description. Yet, the GGA functionals do not offer the same accuracy across the periodic table; it tends to overestimate the lattice parameters of the heavier elements and underestimate band gaps. The cost of the improved accuracy of GGA is also associated with higher computing resources requirement and can thus, affect calculations in resource limited conditions [66].

2.3. Cobalt bulk optimisation

The application of the density functional theory as outlined in section 2.2 requires the system under investigations to be defined appropriately. For this study, the system description was generated via visualisation tools whereby the atomic positions of each component were specified, and these would be interpreted by ab-initio codes to enable DFT calculations. With this study focusing on a cobalt surface, the bulk cobalt phase had to be first optimised geometrically alongside the computational parameters specific to the system. The latter would enable accurate and efficient DFT-based results via the ab-initio code.

The bulk optimisation of Co was done in two phases, 1)optimisation of the computational parameters to ensure efficient running of the DFT code and, 2)optimisation of the geometric parameters of bulk structure. The initial guess for the optimisation steps considered a face-centered cubic (fcc) structure present within the Material Studio package, defined by the FM-3M space group with 4 atoms and lattice parameter of 3.544 Å. The GGA-RPBE functional with PAW potentials was used for all optimisation calculations as it gives a good description for geometric parameters and magnetic properties of cobalt-based system [40], [67], [68]. Computationally, an initial cut-off energy value of 600 eV was used as it is well above the VASP recommended value of 267 eV using PAW potentials [54]. This parameter ensured sufficient convergence of the DFT solutions but the cost of elevated computational resource requirement. It also worth noting that all the optimisations were performed using the spin-polarisation parameter to ensure the well convergence of the magnetic state of the system.

2.3.1. K-points

The Monkhorst-Pack [69] scheme was used for the automatic generation of gamma centered k-point grid in the Brillouin zone whereby the subdivisions N_1, N_2 and N_3 were specified as per Table 2-1. The tetrahedron method with Blöchl corrections was used for the total energy calculation of the bulk system with a smearing width of 0.2 eV [70], [71] and the convergence results are given in Figure 2-1. It can be seen that the energy of the bulk cobalt unit cell converged within the 1 meV/atom criteria for 35 irreducible k-points which corresponds to a 9 x 9 x 9 k-point grid generated by the Monkhorst-Pack sampling scheme [69].

Table 2-1: k-points and the corresponding number of irreducible k-points in a primitive FCC-structure

k-point grid (N_1xN_2xN_3)	**Irreducible k-points**
3 x 3 x 3	4
5 x 5 x 5	10
7 x 7 x 7	20
9 x 9 x 9	35
11 x 11 x 11	56
13 x 13 x 13	84
15 x 15 x 15	120
17 x 17 x 17	165
19 x 19 x 19	220

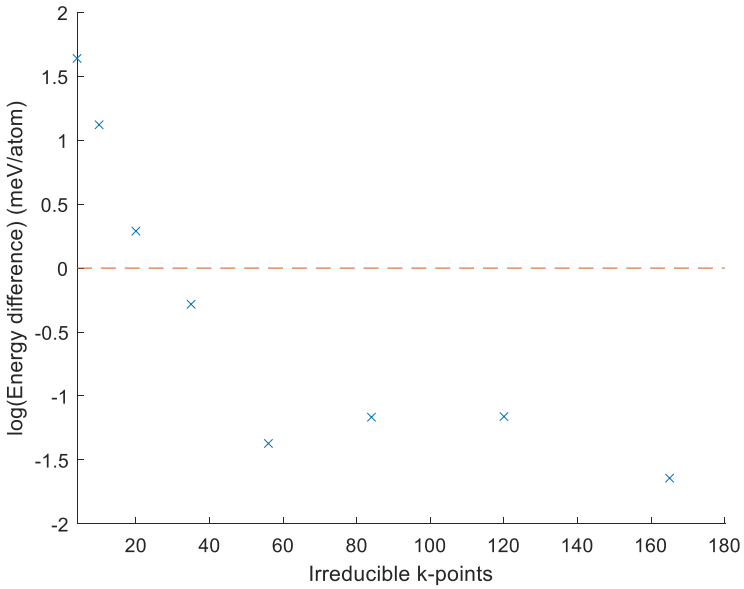

Figure 2-1:Difference in electronic energy $dE = \frac{E_n - E_{n-1}}{n_{Co}}$ ***in a semi-logarithmic plot as a function of the number of irreducible k-points (dash line: convergence criterium).***

2.3.2. Cut-off energy

The cut-off energy was optimised using the same unit cell as the k-point optimisation step with lattice parameter of 3.544 Å. The optimised k-point grid of 9 x 9 x 9 in combination with the tetrahedron method with Blöchl corrections, including a smearing width of 0.2 eV [70], [71] was used for the total energy calculation of the bulk system. From Figure 2-2, a minimum cut-off energy of 380 eV was sufficient for convergence of the total energy of the bulk cobalt unit cell. To ensure reasonably accurate calculations, a slightly higher cut-off energy value of 400 eV was considered as to satisfy the guideline of 1.5 times $E_{cut,rec}$ where $E_{cut,rec}$ = 267 eV, as per the VASP manual for PAW pseudopotentials [72].

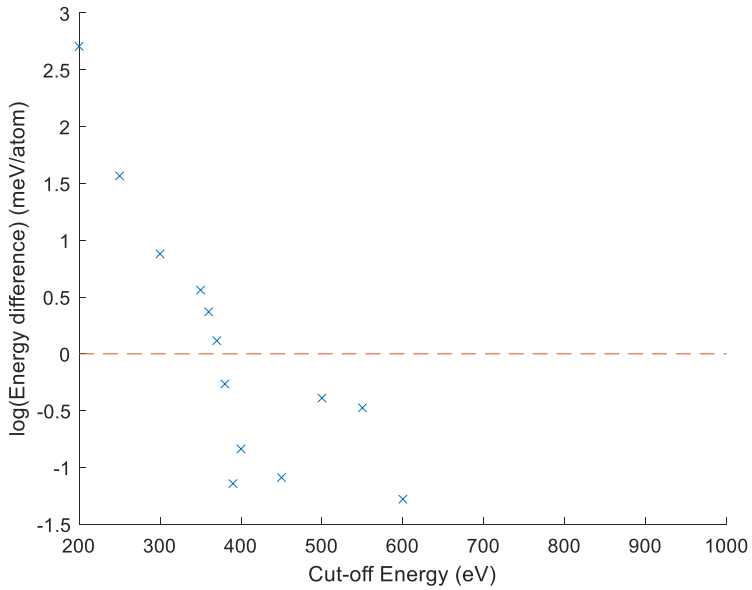

Figure 2-2: Difference in the electronic energy $dE = \frac{E_n - E_{last}}{n_{Co}}$ in a semi-logarithmic plot as a function of the against cut-off energy (dashed line: convergence criterium).

2.3.3. Lattice parameter

The optimisation of the bulk lattice parameter (a) was performed using three approaches which include 1) the empirical(volume screening) method to determine $a_{empirical}$, 2) the use of the Birch-Murnaghan equation of state(EOS) to determine a_{EOS} and, 3) the on-the-fly approach included in the VASP code to determine a_{otf}. For all approaches, a face-centered cubic (fcc) structure defined by the FM-3M space group with 4 atoms and a=3.544 Å was considered as initial guess. For the empirical(volume screening) method, bulk structures with lattice parameters in the range of 3.3 - 3.675 Å with an interval of 0.015 Å were considered. The volume of a uniform unit cell (V) is related to the lattice parameter by $V=a^3$ and $a_{empirical}$ was evaluated by finding the minimum of the total energy of the unit cell as a function of volume, Figure 2-3.

The 3rd order Birch-Murnaghan EOS founded on the basis of the lattice theory was considered for evaluation of the lattice parameter. The model not only considers the symmetry of a cubic crystal but also, factors in all the possible elastic coefficient of the crystal [73]. Thus, offering a good approximation to experimental data for the lattice parameter and the bulk modulus term.

The lattice parameter a_{EOS}, was found by plotting the total energy of the unit cell (E) as a function of the volume to the 3rd order Birch-Murnaghan EOS given by Equation 2-23 [73]. The lattice parameters, $a_{empirical}$ and a_{EOS}, were evaluated at 3.5514 Å and 3.5512 Å respectively.

As shown by Figure 2-3, the EOS is a good representative of the empirical data given a R^2 value close to 1. Furthermore, both $a_{empirical}$ and a_{EOS} are consistent with experimental data of a_{exp}=3.550 Å [74] with an overestimation of 0.0394 and 0.0345 % respectively.

$$E = E_0 + \frac{9V_0B_0}{16}\left\{\left[\left(\frac{V_0}{V}\right)^{\frac{2}{3}} - 1\right]^3 B_0' + \left[\left(\frac{V_0}{V}\right)^{\frac{2}{3}} - 1\right]^2 \left[6 - 4\left(\frac{V_0}{V}\right)^{\frac{2}{3}}\right]\right\} \qquad \textit{Equation 2-23}$$

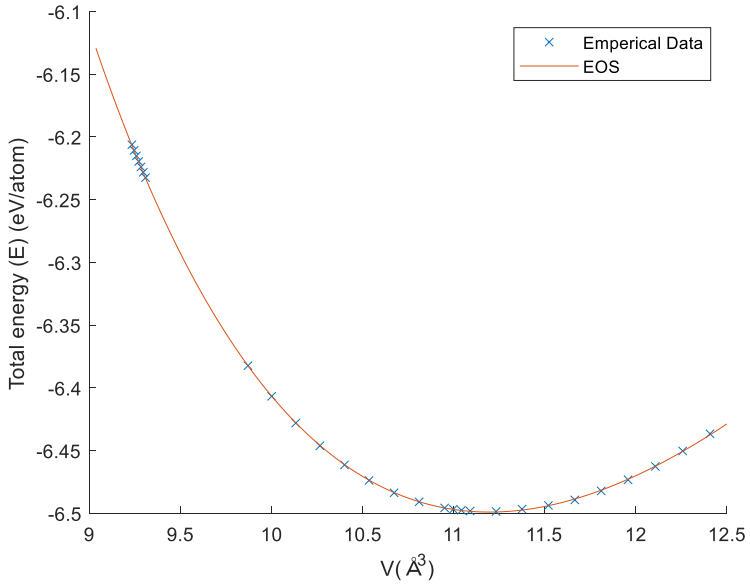

Figure 2-3: Plot of total system energy (E_0) against volume of unit cell(V).

The structure was also relaxed using VASP "on the fly" feature (IBRION=2 and ISIF=3) and a lattice parameter of a_{otf}=3.5445 Å was obtained. Owing to the type of calculation whereby the volume or cell shape was allowed to change, it lead to an underestimation by 0.1540 % in comparison to experimental data [74]. Hence, the lattice parameter of a=3.5512 Å was used to calculate the bulk modulus (B0). A bulk modulus of 185 GPa and a magnetic moment of 1.64 μ_B were obtained for the optimised bulk structure which are in good agreement with experimental values of 191 GPa [75] and 1.70 μ_B [76] respectively.

Table 2-2: Optimised computational and geometric parameters for bulk cobalt

K-point grid	9x9x9
Cut-off energy	400
Lattice parameter (a)	3.5512
Bulk modulus (B0)	185
Magnetic moment(μ_B)	1.64

2.4. Cobalt surface optimisation

For this study the choice of the surface was based the dominant facet on a cobalt nanoparticle which was attributed to Co(111) [67], [68], [77]. The Co(111) slab models were generated based on an asymmetric approach using the optimised bulk crystal lattice parameter of 3.5512 Å and cleaving the defined cobalt surface. The geometric optimisation of the cobalt slab was performed factoring in structural parameters which include 1) slab thickness, 2) vacuum gap and, 3) number of relaxed atomic layers. This will ensure that correct energies are calculated for species adsorbing on the cobalt surface. The structural parameters of the slab were validated through convergence of the energy differences for each scenario. Convergence was assessed based on the adsorption energy whereby CO was used as a probe species on the different Co(111) slabs.

2.4.1. Slab thickness

For the slab models, CO was adsorbed on an atop site of p(2x2) Co(111) slabs where the top two layers within proximity of the adsorbate was allowed to relax and the other sublayers were fixed in their bulk positions. As an initial guess, the vacuum gap between the periodic slabs was set to 12 Å and for the computational parameters, a k-point grid of 9 x 9 x 1 along with a cut-off energy of 400 eV were implemented. The VASP code was used for the periodic DFT calculations to obtain the total energy of the following for the varying slab thicknesses: 1) slab with adsorbed CO, 2) clean slab, and 3) molecular CO. Hence, the adsorption energy of CO ($E_{ads,CO}$) on the p(2x2) Co(111) slab was calculated as follows:

$$E_{ads,CO} = (E_{slab+CO(ads)} + ZPE_{CO(ads)}) - E_{slab} - (E_{CO(g)} + ZPE_{CO(g)}) \qquad \textit{Equation 2-24}$$

Where $E_{slab+CO(ads)}$, E_{slab} and $E_{CO(g)}$ are the total energies of the slab with CO adsorbed, clean slab and molecular CO in the gas phase with the inclusion of dipole corrections. Zero-point energy corrections (ZPE) were included to account for vibrational motions at 0 K. ZPE corrections for CO, $ZPE_{CO(g)}$ and $ZPE_{CO(ads)}$ based on the vibrational modes of molecular CO and adsorbed CO on the surface slab were also included in the adsorption energies. The adsorption energy difference (difference to next) was plotted as a function of the number of layers whereby the convergence criterion for dE_{ads} of 0.02 eV/CO was defined. Based on Figure 2-4, 5 layers was found to be suitable to model the Co(111) slab which is in line with similar theoretical models [62]-[63].

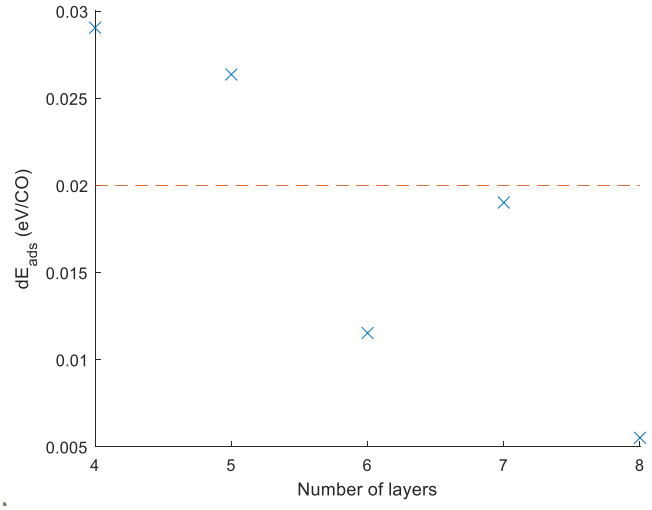

Figure 2-4: Difference in adsorption energy of CO as a function of number of layers (red line: convergence criterium).

For the vacuum gap above cobalt surface, it was chosen to maintain the initial guess of 12 Å as it fall within the range widely used in previous investigations involving adsorption on transition metal surfaces [11], [40], [41], [67], [68], [71], [78]–[80] at coverages in the range of 1/9 -1/4 ML. Thus, yielding converged results in reasonable computational time.

The number of relaxed layers within the Co(111) slab was determined by adsorbing a CO molecule on an atop site on the metal surface and varying the number of relaxed layers in proximity of adsorbate, thereby fixing the number of bottom layers. The adsorption energy of CO was evaluated using Equation 2-25 while ensuring that the adsorbed system and the reference clean slab have the same number of fixed layers (nfx). Since all calculated adsorption energy differences were below the convergence criterion of 0.02 eV/CO, it was decided to proceed with the number of fixed layers that first resulted in the smallest energy difference, in our case fixing the bottom 2 layers. This is agreement with other computational models involving similar Co(111) system [14], [62]-[63].

$$E_{ads,CO,nfx} = (E_{slab+CO(ads),nfx} + ZPE_{CO(ads),nfx}) - E_{slab,nfx} - (E_{CO(g)} + ZPE_{CO(g)}) \qquad \textbf{Equation 2-25}$$

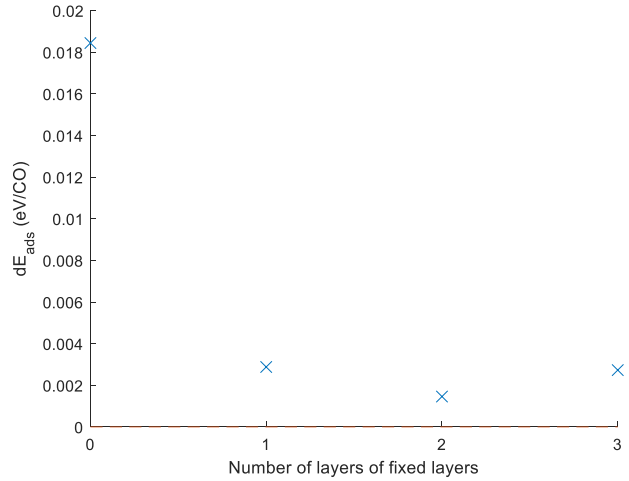

Figure 2-5: Difference in adsorption energy of CO as a function of fixed bottom layers.

2.5.Adsorption models

2.5.1. Adsorption/co-adsorption energy

The adsorption/co-adsorption models were generated on optimised 5-layered Co(111) slab with a p(3x3) cell size. With the focus of this study on CO dissociation and oxygen removal, the adsorption of the reaction species will be modelled at a coverage of 1/9 ML such that minimal lateral interactions will be present between the adsorbates in adjacent cells given the periodic nature of DFT calculations [81] (see Appendix A.1 for sample calculation file). For each of the systems generated, the adsorption energy will be defined with the appropriate reference systems and will further be elaborated in the corresponding chapters.

2.5.2. Vibrational analysis

Vibrational analyses were performed on systems with the adsorbates to validate their stability (see Appendix A.1 for sample calculation file). The calculations involved fixing the atoms of the bare metal while the adsorbate atoms are to be sequentially displaced by a small positive and negative displacement (frozen core approximation) in each cartesian direction of 0.015 Å. From the resulting Hessian matrix, the vibrational frequencies can be calculated. Systems with no imaginary frequencies will correspond to a stable configuration of the adsorbate while a single imaginary frequency in the direction of the reaction pathway corresponds to a transition state. The latter is used for transition state calculation to confirm whether the saddle points from NEB (see section 2.6.1.1) and DIMER (see section 2.6.1.2) methods are actual transition states.

2.5.3. Zero-point energy calculations

To obtain total ground state energy of the metal surfaces with adsorbates, ZPE corrections need be included to the energy of optimisation (total electronic energy) [82] to account for vibrational motions at 0 K. ZPE corrections for the adsorbates and gaseous species/radicals (ZPE) in J/mol was calculated as follows:

$$ZPE = \frac{1}{2}\frac{Rh}{k}\sum_{i=1}^{N} v_i$$ ***Equation 2-26***

Where N is the number of vibrational mode of the adsorbates, c is speed of light in cm/s, h is the plank constant in J.s, v_i is the vibrational modes(see section 2.5.2) of the adsorbate in cm^{-1}, R is the gas constant in J/mol.K and k is the Boltzmann's constant in J/K.

2.5.4. Thermodynamic corrections

The electronic energies (E^{elec}) determined from the DFT-based calculations are based on vacuum conditions, a temperature of 0 K and a pressure of 0 bar. Therefore, in order to assess the viability of the different models under Fischer-Tropsch conditions, thermodynamic corrections based on the equations by Iruka [83] and Sandler [84] need to be applied. For the thermodynamic viability of the models, temperature correction to the Gibbs free energy of each component at temperature T was considered. The Gibbs free energy of the species i is defined in terms of the enthalpy and entropy contributions as follows:

$$G_i(T) = H_i(T) - TS_i \qquad \textbf{Equation 2-27}$$

The enthalpy of the different species considers the vibrational, rotational and translation contribution given *by* E_i^{vib}, E_i^{rot} *and* E_i^{trans} along with the DFT-based energy of the species (E^{elec}). It is worth noting that the electronic energy also includes zero-point energy (ZPE) corrections for the species as per Equation 2-26.

$$H_i(T) = E^{elec} + E_i^{vib}(T) + E_i^{rot}(T) + E_i^{trans}(T) + RT \qquad \textbf{Equation 2-28}$$

With enthalpy of adsorption split into vibrational, rotational and translation contributions, the following partition functions was applied [83]:

$$E_i^{vib}(T) = \frac{1}{2}N_A\sum_i h\nu_i + N_A\sum_i \frac{h\nu_i \exp\left(-\frac{h\nu_i}{k_BT}\right)}{1-\exp\left(-\frac{h\nu_i}{k_BT}\right)} \qquad \textbf{Equation 2-29}$$

$$E_i^{rot}(T) = \frac{n_{rot}}{2}RT \qquad \textbf{Equation 2-30}$$

$$E_i^{trans}(T) = \frac{3}{2}RT \qquad \textbf{Equation 2-31}$$

N_A	Avogadro constant
h	Planck constant
ν_i	Vibrational model of species i
k_B	Boltzmann constant
n_{rot}	Rotational degrees of freedom
R	Ideal Gas constant

Similarly, the entropy part of the Gibbs free energy can be expressed in terms of vibrational, rotational, and translational contributions, Equation 2-32. It should be noted that a degeneracy contribution was also included to cater for stationary states that may have the same energy. Furthermore, additional considerations need to be made dependent on the type of species whether it is a gas molecule or an adsorbate on the cobalt surface. For the case of gaseous species, they can be assumed to be able to vibrate, rotate and translate freely in all directions. Hence, all the corresponding partition functions need to be accounted, Equation 2-33 to Equation 2-37. Additionally, the appropriate rotational partition function for gaseous species needs to be considered on the basis of a linear (Equation 2-34) or non-linear molecule (Equation 2-35).

Adsorbates on the other hand, are limited in terms of rotation and translation as the bonds between the metal surface and the adsorbate hinder those free movements. Hence, only the vibrational partition functions were considered for the evaluations of the enthalpic and entropic contributions.

$$S_i(T) = S_i^{vib}(T) + S_i^{rot}(T) + S_i^{trans}(T) + S_i^{degeneracy} \qquad \textit{Equation 2-32}$$

$$S_i^{vib} = -R\sum_j \ln\left(1 - e^{-\frac{hv_j}{k_BT}}\right) + R\sum_j \frac{hv_j}{k_BT}\frac{e^{\frac{-hv_j}{k_BT}}}{1 - e^{\frac{-hv_j}{k_BT}}} \qquad \textit{Equation 2-33}$$

$$S_i^{rot,linear} = R\left(ln\left(\frac{8\pi^2 I k_B T}{\sigma h^2}\right) + 1\right) \qquad \textit{Equation 2-34}$$

$$S_i^{rot,non-linear} = R\left(\ln\left(\frac{8\pi^2}{\sigma}\right) + \frac{3}{2}\ln\left(\frac{2\pi k_B T}{h^2}\right) + \frac{1}{2}\ln(I_A I_B I_C) + \frac{3}{2}\right) \qquad \textit{Equation 2-35}$$

$$S_i^{trans} = R\left(\frac{3}{2}\ln\left(\frac{2\pi m}{h^2}\right) + \frac{5}{2}\ln(k_B T) - \ln(p) + \frac{5}{2}\right) \qquad \textit{Equation 2-36}$$

$$S_i^{degeneracy} = Rln(g) \qquad \textit{Equation 2-37}$$

I_X Principal moments of inertia
σ External symmetry number
g Degeneracy number
p Pressure of the system

2.6. Reactions models

2.6.1. Transition state calculations

To calculate the activation energy for a reaction or the activation energies of the different steps of a complex reaction, appropriate transition state of the reaction needs to be identified along the minimum energy path between the initial and final state of the species. This is achieved by first identify saddles points across a set of intermediate images along the reactions path using nudge elastic band (NEB) [85]–[87] calculations and then, optimising these saddle points using the DIMER method [76]-[77] (see Appendix A.1 for sample calculation file). To sure the relevance of these optimised saddle points, vibrational analyses will be performed as final step, whereby a single imaginary point in the direction of the reaction pathway will be considered as the validation parameter.

2.6.1.1. Nudged elastic band calculations

The transition states (TS) corresponding to saddle points along the reaction path between the reactants and products, will be identified though optimisation of a set number of intermediate images along the reaction path. Conventional nudge elastic band (NEB) calculations involve a constrained optimisation process whereby each image identifies the lowest possible energy though the inclusion of spring forces along the band between the images such that they are equidistant from each other. Though this method provides an overall idea of the transition state along the reaction coordinate, it falls short when the transition state lies between two images (refer to blue plot, Figure 2-6). Hence, further optimisation will be required to identify the latter.

An improvement over the conventional NEB, is the use of the climbing image nudged elastic band (cNEB) method [85] where a more accurate identification of the TS could be achieved using fewer images. The cNEB method maximises the energy of an image along the band while minimising in the other directions such that upon convergence, there will be an image at the exact saddle point (refer to red plot, Figure 2-6). Instead of introducing spring forces along the image band, the true force of the image along the tangent is inverted and therefore, creating varied spacing on either side of the highest energy image [85]–[87].

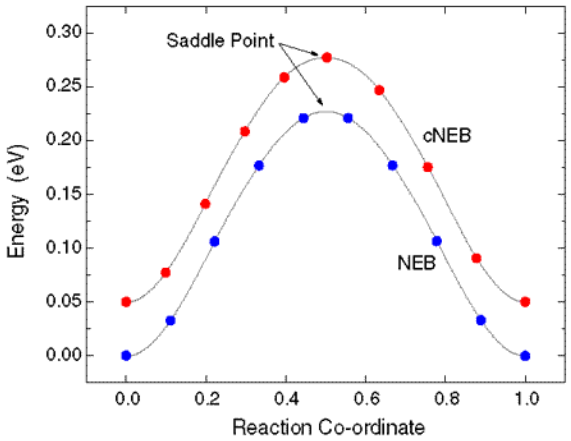

Figure 2-6: Comparison of NEB and cNEB methods for the determination of transition states for Al adatom on Al(100), taken from [90]***. Blue line represents conventional NEB and red line represent cNEB approach. Note the cNEB plot have been shifted by 0.05 eV so that a distinction can be made between the two graphs***

2.6.1.2. DIMER calculations

Due to the extensive computational resources and computational time required to converge the saddle point, single step (NSW=0) cNEB calculations were performed for each reaction investigated to obtain an initial guess of the transition state along the reaction coordinate [85]. To obtain the accurate transition state, the image found using cNEB calculation is optimised using the DIMER method and convergence to the exact saddle point can be achieved [76]-[77]. DIMER calculations use the min-mode method to find nearby saddle points from an initial configuration though specification of a direction along the reaction coordinate [76]-[77]. Depending on the complexity of the reaction, the direction could be specified towards to the final optimised state or in the case of unknown reaction mechanisms, the dimer method could be used to find intermediate images corresponding to saddle points at different position along the reaction path [91].

2.6.2. Rate calculations

2.6.2.1. Simplified model

For this study, we are comparing the promotional effects of MnO_x clusters on Co(111) in the Fischer-Tropsch synthesis. CO dissociation being a paramount step in the FTS, it is therefore useful to assess the kinetics of the reaction on both unpromoted and promoted cobalt surface. The reaction rate constant (s^{-1}) for the clean and MnO_x promoted system were calculated on the basis of the Transition State Theory (TST) formulated by Eyring [92]. Transition state theory in the case of this study, stipulates that between the state that the adsorbates are reactants and the state where the adsorbates are products, there exists a transition state whereby an activated complex is formed from the reactant. Based on the theory, the outcome of a reaction is dependent on the following: 1) The concentration of the activated complex, 2) The rate of the complex breaks apart, and 3) The way the complex breaks apart: whether is breaks to reform the reactants or breaks to form the products. Considering the CO dissociation reaction on both the clean and the promoted surface, the following reaction were devised based on the TST and the thermodynamic equilibrium constant $K^{\ddagger}$ defined:

On unpromoted slab:

$$CO_{ads} \leftrightarrow CO^{\ddagger}_{ads} \rightarrow C_{ads} + O_{ads} \qquad \textit{Equation 2-38}$$

$$K^{\ddagger} = \frac{\left[CO^{\ddagger}_{ads}\right]}{\left[CO_{ads}\right]} \qquad \textit{Equation 2-39}$$

On MnOx promoted slab:

$$(MnO_x + CO)_{ads} \leftrightarrow (MnO_x + CO)^{\ddagger}_{ads} \rightarrow (MnO_x)_{ads} + C_{ads} + O_{ads} \qquad \textit{Equation 2-40}$$

$$K^{\ddagger} = \frac{\left[(MnO_x + CO)^{\ddagger}_{ads}\right]}{\left[(MnO_x + CO)_{ads}\right]} \qquad \textit{Equation 2-41}$$

For the reaction to proceed and form the specified products, the energy barrier between the high energy intermediate, in this case the transition state identified using the DIMER method [76]-[91], and the reactants needs to be overcome. Consequently, the rate of reaction is defined as the number of activated intermediate dissociating into products. Factoring in the frequency of the concentration of intermediate dissociating, the rate of the dissociation reaction can be written as whereby v is the vibrational frequency:

$$rate = v\left[CO^{\ddagger}_{ads}\right] \qquad \textit{Equation 2-42}$$

$$rate = vK^{\ddagger}[CO_{ads}] \qquad \textit{Equation 2-43}$$

Rate can also be written as a function of the rate constant and the concentration of the reactants:

$$rate = k[CO_{ads}] \qquad \textit{Equation 2-44}$$

Combining Equation 2-43 and Equation 2-44:

$$k[CO_{ads}] = vK^{\ddagger}[CO_{ads}] \qquad \textit{Equation 2-45}$$

$$k = vK^{\ddagger} \qquad \textit{Equation 2-46}$$

Defining *v* and substituting into Equation 2-46, the rate constant was evaluated, Equation 2-48:

$$v = \frac{k_B T}{h} \qquad \textit{Equation 2-47}$$

$$k = \frac{k_B T}{h} K^{\ddagger} \qquad \textit{Equation 2-48}$$

Where k_B is the Boltzmann's constant, T is the absolute temperature in Kelvin and h is the Plank's constant.

Combining rate kinetics with thermodynamic theory, $K^{\ddagger}$ can be expressed in terms of Gibbs free energy of activation $\Delta G^{\ddagger}_{act}$:

$$K^{\ddagger} = e^{\frac{-\Delta G^{\ddagger}_{act}}{RT}} \qquad \textit{Equation 2-49}$$

To express $K^{\ddagger}$ as a function of T:

$$K^{\ddagger}(T) = e^{\frac{-\Delta G^{\ddagger}_{act}(T)}{RT}} \qquad \textit{Equation 2-50}$$

$$\Delta G^{\ddagger}(T) = \Delta H^{\ddagger}(T) - T\Delta S^{\ddagger} \qquad \textit{Equation 2-51}$$

Rate as a function of T:

$$k(T) = \frac{k_B T}{h} K^{\ddagger}(T) \qquad \textit{Equation 2-52}$$

$$k(T) = \frac{k_B T}{h} e^{\frac{\Delta S^{\ddagger}_{act}(T)}{R}} e^{\frac{-\Delta G^{\ddagger}_{act}(T)}{RT}} \qquad \textit{Equation 2-53}$$

The rate equation above was then used to evaluate the rate of dissociation of CO on both the clean and the promoted cobalt slab at an initial surface coverage of 1/9 ML

3. Adsorption of Fischer-Tropsch species on Co(111)

3.1. Introduction

Previous studies by Pedersen et al. [11] and Johnson et al. [14] have suggested that the presence of manganese on cobalt-based Fischer-Tropsch catalyst has an impact on the adsorption of certain species on the metal surface. To understand the adsorption effects, key reactions involved in Fischer-Tropsch synthesis had to be identified. While CO dissociation has been extensively studied being a fundamental step for Fischer-Tropsch synthesis[93]–[95], oxygen removal has also gained some attention [96]. A recent study, has suggested that the removal of oxygen as water may be a rate limiting step within the synthesis loop [68]. Consequently, for this study, the species involved in CO dissociation and oxygen removal were considered. For cobalt-based catalyst systems, the supported catalysts are typically synthesised to contain cobalt crystallites with an average diameter less than 100 nm [97] and are stable in the fcc phase [98]. Furthermore, it is suggested that the fcc phase comprises of the most dense surface planes which includes Co(111) [70] and as such, the surface reactivity of the latter is of interest to this study. With the identification of the relevant Fischer-Tropsch synthesis species and the cobalt surface plane, the adsorption energies of the different species on the metal surface can then be evaluated. These energies will then be used as a basis for comparison with the adsorption of the same species on promoted cobalt surfaces. Following the base case, a possible model of the Mn promoter on the Co terrace surface will be devised and a phase diagram for the formation of the promoter complexes will be generated to identify the likely configuration under Fischer-Tropsch synthesis conditions. Finally, with the suitable configurations identified, the adsorption energies of the different Fischer-Tropsch synthesis species on the promoted metal surface will be calculated.

3.2. Adsorption of C, CO, H, O, OH and H_2O on Co(111)

Isolated Fischer-Tropsch synthesis species were each probed at the atop, bridge, fcc and hcp sites on the Co(111) surface and the resulting lowest energy configurations are shown in Figure 3-1. The stabilities of these configurations were validated though vibrational analyses whereby no imaginary frequencies were found (Appendix B.1). The preferred adsorption site of C at an adsorption distance (B) of 1.787 Å, was found to be the hcp position in line with literature[94]. Maintaining a low coverage of 0.11 ML, the adsorption of a CO molecule at the hcp position resulted in the most stable CO adsorption configuration with a C-O bond length of 1.203 Å comparable to similar DFT studies [11], [67]and an adsorbate distance (B) of 1.99 Å. For the case of H which is the product of the dissociative adsorption of H_2 on the cobalt surface, the lowest energy configuration was found upon adsorption at the fcc position [68] at a height (B) of 1.755 Å. Also one oxygen, the product of CO dissociation and the disproportionation reaction of hydroxyl species, is most stable on an hcp site [94], [68]. At very low coverage, following the reaction between O and H, the resulting OH species prefer the hcp position under the lowest energy configuration [68] and sits at an adsorption height (B) of 2.026 Å. The calculated bond length $d_{O\text{-}H}$ of 0.973 Å, is in agreement with similar theoretical studies on Co(111) whereby $d_{O\text{-}H}$ value of 0.972 Å was obtained [68]. Finally, the preferred configuration for an H_2O molecule was found to be a floating position at an atop site with an adsorption distance (B) of 2.387 Å. With regards to optimised geometric parameters, an O-H bond length of 0.978 Å and a H-O-H bond angle of 104.8 ° was determined and was found to be in close agreement with literature [68] and as such, the validity of the model could be confirmed.

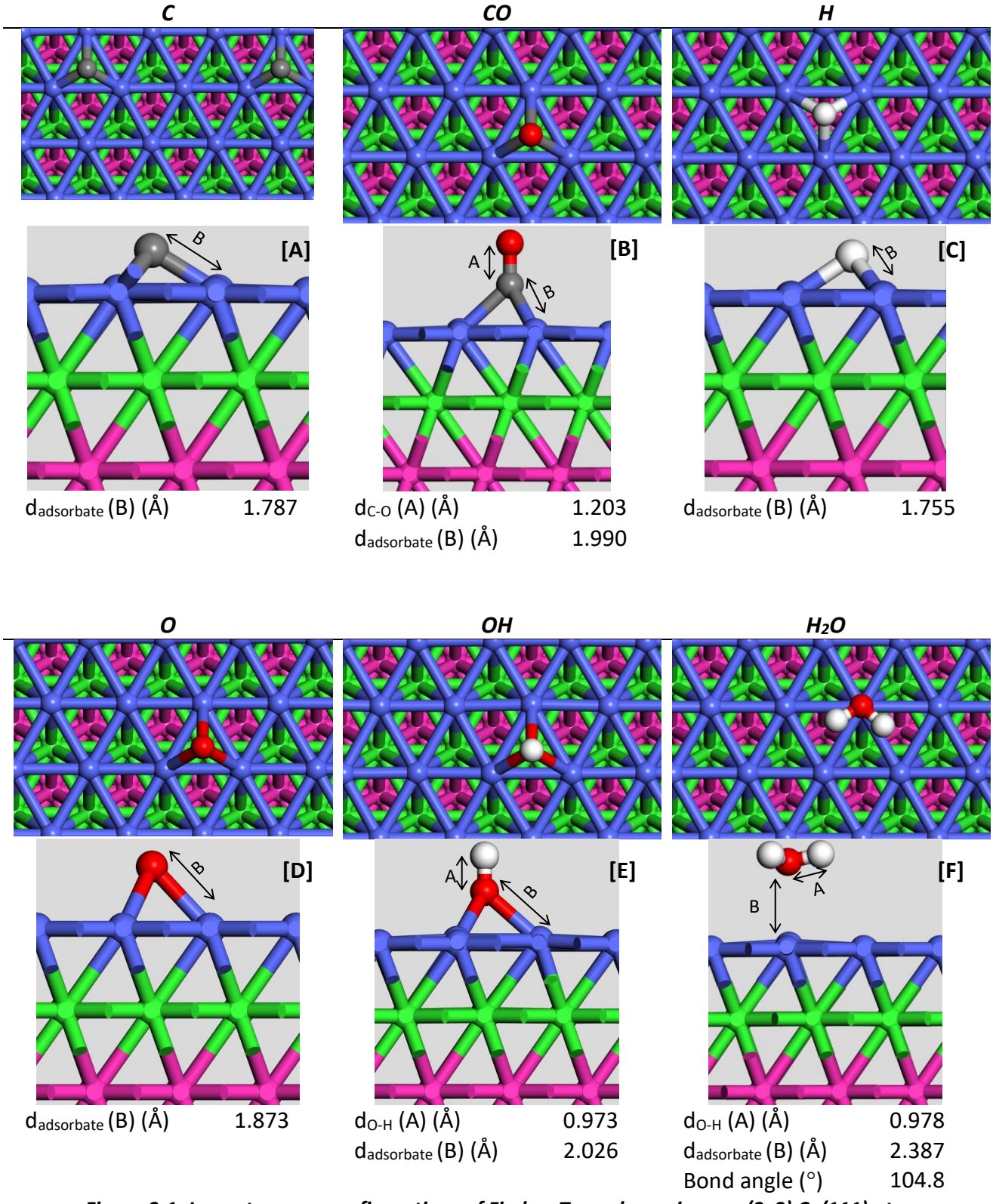

Figure 3-1: Lowest energy configurations of Fischer-Tropsch species on p(3x3) Co(111) at a coverage of 0.11 ML. Atoms represented by C, H, O, Co in first/forth/fifth layer, Co in second and Co in third layer.

Adsorption is a fundamental step in heterogenous catalysis as gaseous reactants need to bind to the solid catalyst surface in order to initiate reactions. For DFT based reaction studies, the evaluation of adsorption energies not only serves as the basis to assess the strength of adsorption of gaseous reactants or intermediates on the catalyst surface but is also used to establish the Brønsted−Evans−Polanyi (BEP) relation and the volcano curve explained by the Sabatier principle [99]. For this study, the adsorption energies of the FTS species on the Co(111) surface were evaluated using Equation 3-1 in combination with the coefficients listed in Table 3-1 and the total energies of the corresponding molecules in the gas phase listed under Table 3-2. Furthermore, ZPE corrections based on the vibrational modes of the adsorbates and gaseous molecules/radicals(see Appendix B.1) were also included in the total energies reported in Table 3-2.

$$E_{ads,i} = E_{slab+ads} - E_{slab} - aE_{H_2} - bE_{CO} - cE_{H_2O} \qquad \textit{Equation 3-1}$$

Table 3-1: Stoichiometric coefficients the calculation of adsorption energies for the adsorption models

Adsorbate	*a*	*b*	*c*
C	1	1	-1
H	0.5	0	0
O	-1	0	1
CO	0	1	0
OH	-0.5	0	1
H_2O	0	0	1

Table 3-2: Total energies of reference states for adsorption energy calculations including ZPE corrections

Reference state	E_{total} *(eV)*
Co(111)-clean	-280.9
H_2	-6.718
CO	-14.29
H_2O	-13.65

Comparing the calculated adsorption energies on Co(111) to the energies reported in literature for the same surface, Table 3-3, it can be noted that a significant disparity between the energies (excess of 1 eV) is present with the exception of CO and H_2O. For the adsorption energy of CO, we note an energy difference in the range of +0.12 eV to -0.51 eV and for H_2O, the energy difference is 0.28 eV. We can attribute these energy differences to the use of smaller p(2x2) slabs which can induce some degree of lateral interactions (attractive or repulsive) between similar neighbouring adsorbates compared to a p(3x3) slab. Hence, the total energies of the systems will be affected [100] and cause a shift in the adsorption bands [101].

We can also associate a small degree of the adsorption energy differences to the performance of the functionals used and their accuracies. The PBE functional as implemented by the majority of the DFT studies, report a mean absolute error (MAE) of approximately 25 kJ/mol for chemisorption systems involving transition metals while the RPBE function accounts for a MAE value of approximately 15 kJ/mol. For the case of the PW91 functional, the MAE value for chemisorption systems maxed out at approximately 30 kJ/mol [102], [103]. Therefore, only a difference of 0.15-0.3 eV between the calculated and literature energies could be attributed to functional performance.

Although the use of smaller p(2x2) slabs and different functionals can impact the adsorption energies, they cannot justify the significant differences in energies. Instead, the latter is attributed to the use of alternate gaseous reference states. In contrast a CO, H_2 and H_2O ensemble as reference state, individual radicals of C, H, O and OH in the gaseous state were used [11], [94], [41]-[40], [70]-[67],. The calculated adsorption energies were re-evaluated with radicals in the gaseous phase to enable useful comparison. The updated adsorption energies under Table 3-3, were found to be more aligned with the values from literature with differences in the range of -0.7 eV to -1.3 eV which can be expected with statements about slab size and functional. The adsorption of H on Co(111) on the other hand was still vastly different, where the updated adsorption energy seems to be doubled.

Table 3-3: Adsorption energies of various species on Co(111) in comparison to literature using gaseous molecular and radical reference states.

	$E_{ads,zpe}$ (eV)	**$E_{ads,zpe}$ (eV)**	**E_{ads} (eV)**
Species	**Co(111)[a] + molecular reference states (CO_g, H_{2g}, H_2O_g)**	**Co(111)[a] + radical reference states(C_g, H_g, O_g, OH_g)**	**Literature**
C	-0.374	-7.57	-6.95[b], -6.76[c], -6.80[d]
CO	-1.35	-1.35	-1.23[e], -1.76[b], -1.61[d], -1.85[f], -1.38[g]
H	-0.345	-6.81	-2.84[b], -2.90[f], -2.83[g]
O	-0.166	-6.93	-5.73[b], -5.61[d], -6.23[f]
OH	-0.190	-3.08	-3.59[f], -3.50[g]
H_2O	0.012	0.012	-0.28[f], -0.28[g]

[a] p(3x3) Co(111), RPBE functional, VASP code, [b] p(2x2) Co(111), PBE functional, VASP code [11], [c] p(2x2) Co(111), PW91 functional, VASP code [70], [d] p(2x2) Co(111), PBE functional, VASP code [94], [e] p(3x3) Co(111), RPBE functional, VASP code [67], [f] p(3x3) Co(111), PBE functional, VASP code [41], [g] p(3x3) Co(111), PBE functional, VASP code [40].

3.3. Manganese ligands on Co(111)

3.3.1. MnO base case

For this study the MnO models were considered as ligands with Mn as the central metal atom bound to an oxygen atom and Mn formally in the +2 oxidation state (with O in the -2 oxidation state) [11],[14]. Hence, combining the ligand description and the defined oxidation state, a base case was generated by introducing the simplest oxidic form of Mn that displays the +2-oxidation state on the metal surface. The Co-OMn models were generated by adsorbing an oxygen atom at the atop, fcc, hcp and bridge positions on a p(2x2) Co(111) slab at a coverage of 0.25 ML. To complete the ligand complex, the manganese atom was introduced directly atop of the oxygen atom in the different cases. Figure 3-2 shows the result of the optimised geometries. The OMn ligands in the atop, fcc and hcp positions retain their linear configuration perpendicular to the surface as seen in Figure 3-2. On the bridge site adsorption, the ligand collapses and forms a bridge bond between the oxygen in the fcc site and the manganese atom in the adjacent hcp site. Based on the total energies of the different geometries, the bridge configuration is more stable on the Co(111) surface as shown by the lowest total energy of -139.9 eV. The stable OMn ligand can described with a Mn-O bond length of 1.915 Å and a Co-O-Mn bond angle of 154.9° between the oxygen and manganese atoms. The stability of the bridge bonded OMn was further validated using vibrational analysis since only real frequencies were evaluated (Appendix **B.1**).

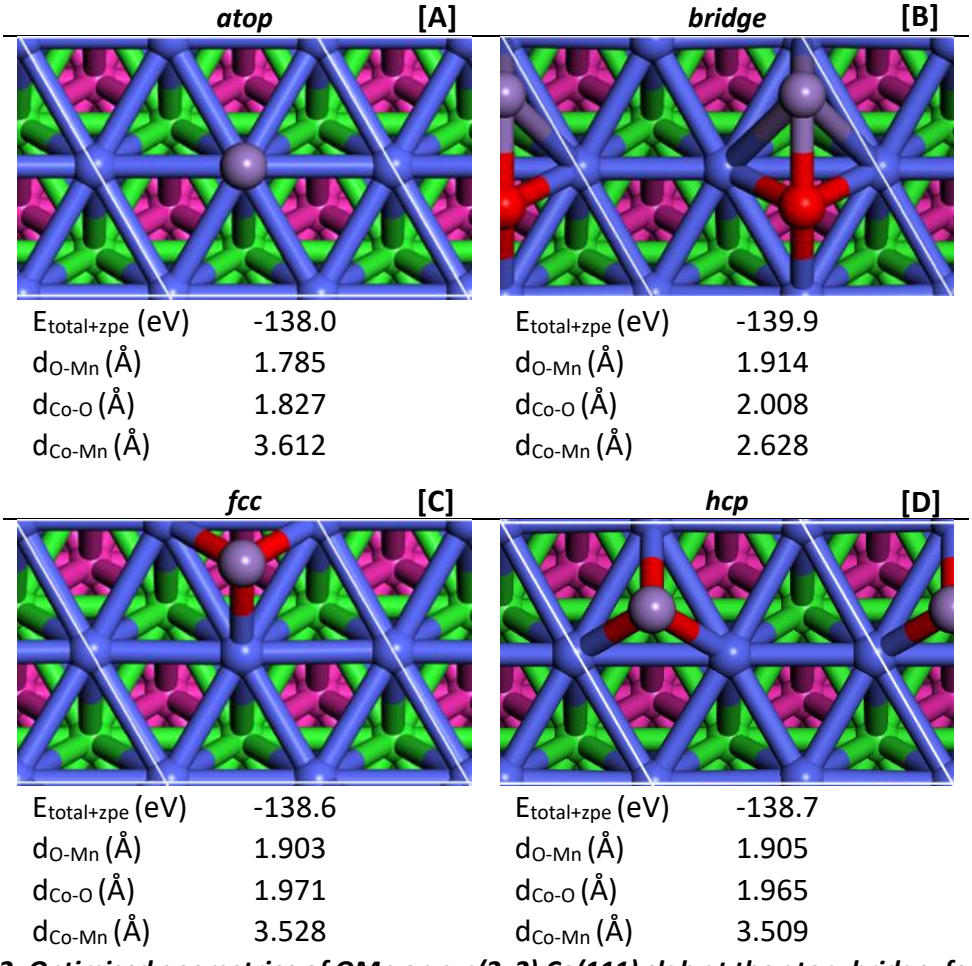

	atop [A]	bridge [B]
$E_{total+zpe}$ (eV)	-138.0	-139.9
d_{O-Mn} (Å)	1.785	1.914
d_{Co-O} (Å)	1.827	2.008
d_{Co-Mn} (Å)	3.612	2.628

	fcc [C]	hcp [D]
$E_{total+zpe}$ (eV)	-138.6	-138.7
d_{O-Mn} (Å)	1.903	1.905
d_{Co-O} (Å)	1.971	1.965
d_{Co-Mn} (Å)	3.528	3.509

Figure 3-2: Optimised geometries of OMn on a p(2x2) Co(111) slab at the atop, bridge, fcc and hcp sites at a coverage of 0.25 ML. Atoms represented by O, Mn, Co in first/forth/fifth layer, Co in second and Co in third layer.

Repeating the same procedure on a p(3x3) slab at a coverage of 0.11 ML, similar observations were noted whereby the optimised structure consisted of an oxygen atom in a fcc site and an adjacent manganese atom in a hcp site connected by a O-Mn bond over the Co-Co bridge position, Figure 3-3. For the larger slab, the bond distance between the oxygen and manganese atom was evaluated at 1.946 Å and the Co-O-Mn bond angle was evaluated at 155.9°. The elongation of the Mn-O bond can be attributed to the use of the larger supercell whereby neighbouring adsorbates experience less repulsive lateral interactions. Hence, the OMn ligand can relax into a more stable geometry.

bridge

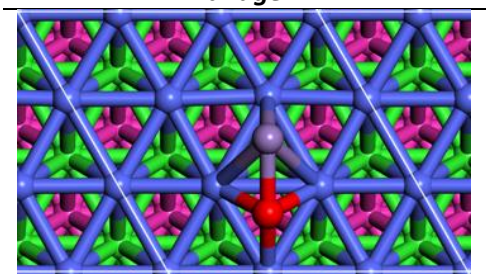

$E_{total+zpe}$ (eV)	-296.1
d_{O-Mn} (Å)	1.946
d_{Co-O} (Å)	1.979
d_{Co-Mn} (Å)	2.626

Figure 3-3: OMn configuration with the lowest total energy on a p(3x3) Co(111) slab at a coverage of 0.11 ML. Atoms represented by O, Mn, Co in first/forth/fifth layer, Co in second and Co in third layer.

In contrast to this study, the MnO model generated by Gençoğlu [41], involved first the adsorption of a manganese atom at the different sites on Co(111) followed by the addition of an oxygen atom atop the manganese in each case. At a coverage of 0.25 ML, the hcp adsorbed MnO was found to be the most stable configuration with an adsorption energy of -254 kJ/mol (-2.63 eV) where still in the linear configuration. On the other hand, the MnO base model by Doorslaer [40], was devised by first probing the manganese atom at different sites on the Co(111) surface and then adsorbing the oxygen atom at adjacent sites. From this approach, the most stable MnO configuration at a coverage of 0.11 ML was found to be a bridge bonded manganese in the hcp position while oxygen in the adjacent fcc site, similar to our study. The stable configuration by Doorslaer [40] was attributed by the lowest Gibbs free energy of formation of 70 kJ/mol given by Equation 3-2:

$$Co_{45}(s) + MnO(s) \rightarrow [Co_{45}MnO](s) \qquad \textbf{Equation 3-2}$$

3.3.2. MnO_x models

An initial configuration of MnO_x was established in section 3.3.1, additional possible configurations still need to be modelled and assessed. While H_2 is normally present in a Fischer-Tropsch reactor, H_2O is also a significant by-product in Co-based Fischer-Tropsch synthesis. Therefore, it may have an impact on the formation of MnO_x and the resulting geometries. From this part onwards, the generated MnO_x models were referred as O_xMn ligands whereby the first part is assigned to the number of oxygen atom, x, directly bonded to the cobalt surface and followed by the manganese atom directly bonded to those oxygen atoms. In the case of additional complexes bonded to the ligand, the nomenclature will take the form of $O_xMn(B)_y$, where B denotes the additional complex bonded to the manganese atom and y the number of repeats of the attached group. The bridge bonded OMn ligand on a p(3x3) slab was used to generate additional ligands. Considering the state of equilibrium with H_2O and H_2 in the FT reactor, Equation 3-3 to Equation 3-7, were used to theorise possible OMn-based ligands configurations and these were modelled on the Co(111) surface, Figure 3-4.

$$OMn + H_2O \leftrightarrow OMn(OH) + \frac{1}{2}H_2 \qquad \textit{Equation 3-3}$$

$$OMn + H_2O \leftrightarrow O_2Mn + H_2 \qquad \textit{Equation 3-4}$$

$$OMn + 2H_2O \leftrightarrow OMn(OH)_2 + H_2 \qquad \textit{Equation 3-5}$$

$$OMn + 2H_2O \leftrightarrow O_2Mn(OH) + \frac{3}{2}H_2 \qquad \textit{Equation 3-6}$$

$$OMn + 2H_2O \leftrightarrow O_3Mn + 2H_2 \qquad \textit{Equation 3-7}$$

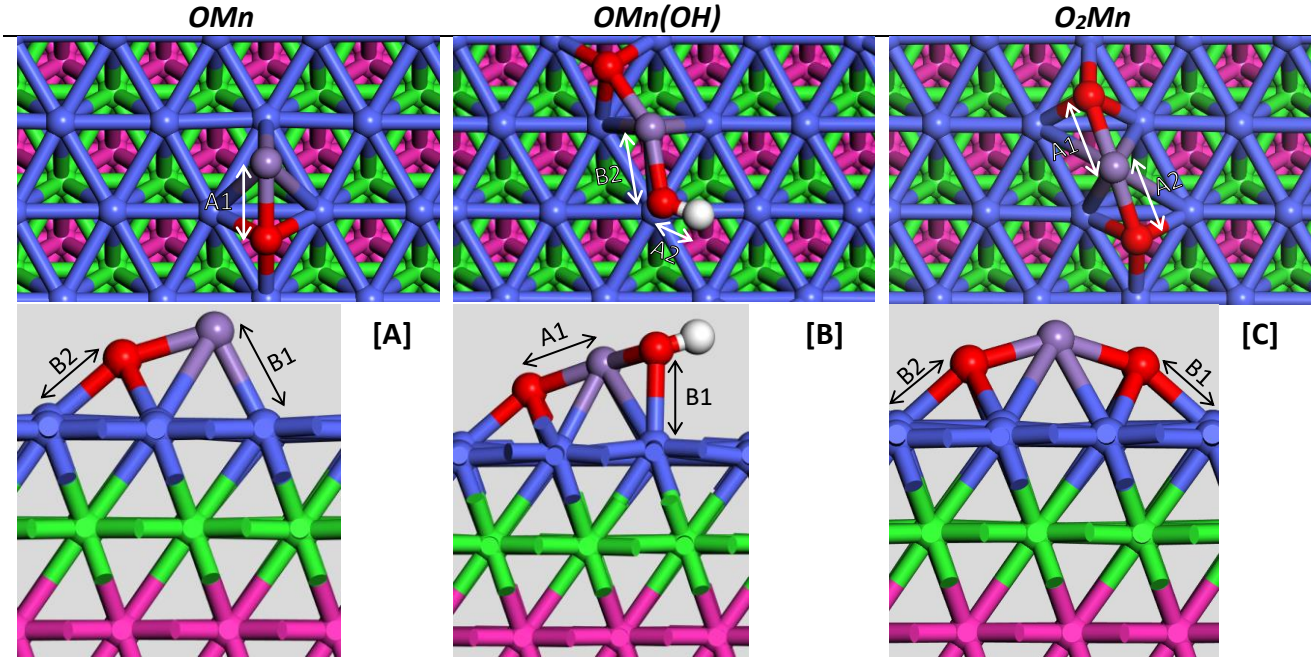

$E_{total+zpe}$ (eV)	-296.1	$E_{total+zpe}$ (eV)	-307.1	$E_{total+zpe}$ (eV)	-303.6
$d_{O\text{-}Mn}$ (A1) (Å)	1.946	$d_{O\text{-}Mn}$ (A1) (Å)	1.937	$d_{O\text{-}Mn}$ (A1) (Å)	1.940
$d_{adsorbate}$ (B1) (Å)	2.347	$d_{O\text{-}H}$ (A2) (Å)	0.975	$d_{O\text{-}Mn}$ (A2) (Å)	1.936
$d_{adsorbate}$ (B2) (Å)	1.979	$d_{adsorbate}$ (B1) (Å)	2.198	$d_{adsorbate}$ (B1) (Å)	1.996
		$d_{adsorbate}$ (B2) (Å)	1.905	$d_{adsorbate}$ (B2) (Å)	2.003

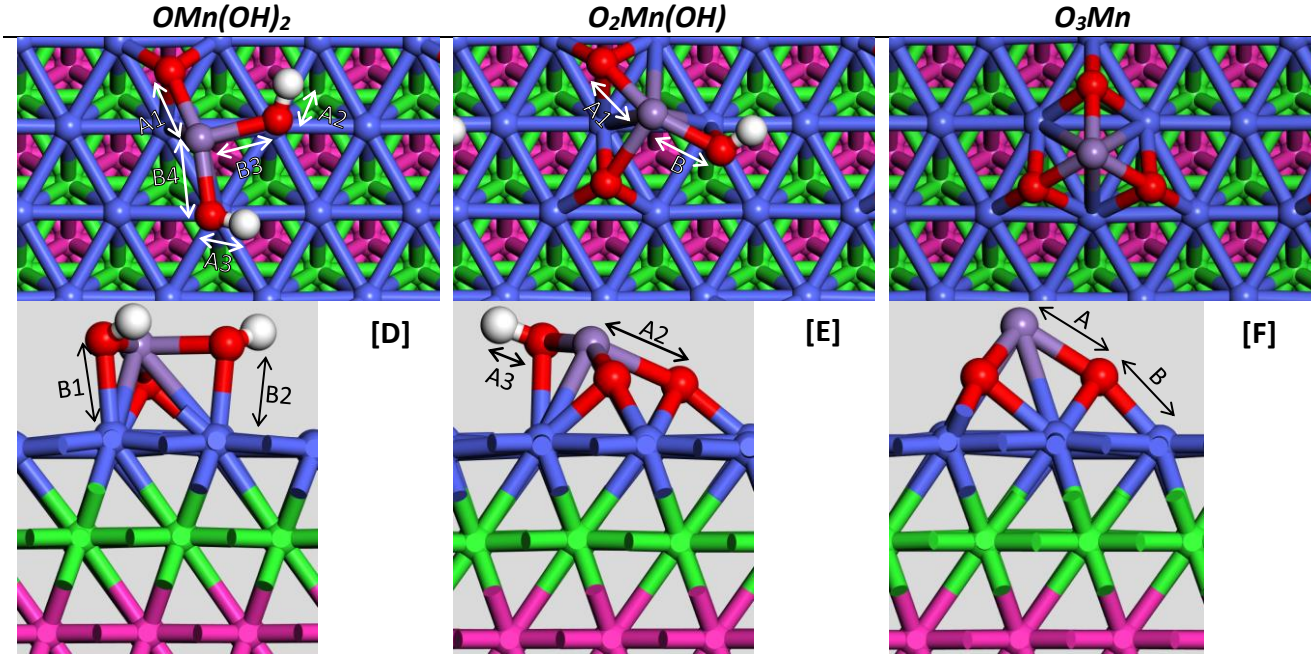

$E_{total+zpe}$ (eV)	-317.3	$E_{total+zpe}$ (eV)	-314.1	$E_{total+zpe}$ (eV)	-310.1
$d_{O\text{-}Mn}$ (A1) (Å)	2.002	$d_{O\text{-}Mn}$ (A1) (Å)	1.975	$d_{O\text{-}Mn}$ (A) (Å)	1.985
$d_{O\text{-}H}$ (A2) (Å)	0.977	$d_{O\text{-}Mn}$ (A2) (Å)	1.942	$d_{adsorbate}$ (B) (Å)	1.894
$d_{O\text{-}H}$ (A3) (Å)	0.977	$d_{O\text{-}H}$ (A3) (Å)	0.976		
$d_{adsorbate}$ (B1) (Å)	2.086	$d_{adsorbate}$ (B1) (Å)	1.983		
$d_{adsorbate}$ (B2) (Å)	2.131	$d_{adsorbate}$ (B2) (Å)	1.833		
$d_{adsorbate}$ (B3) (Å)	2.020				
$d_{adsorbate}$ (B4) (Å)	1.947				

Figure 3-4: Optimised O_xMn and $O_xMn(B)_y$ configurations on p(3x3) Co(111) slabs. Atoms represented by H, O, Mn, Co in first/forth/fifth layer, Co in second and Co in third layer.

For each of the ligand models, the lowest total energy configurations have been included in Figure 3-4 and the stability of these configurations were validated though vibrational analyses whereby no imaginary frequencies were found (Appendix **B.1**). It can also be noted that the addition oxygen atoms and hydroxyl groups minimise the total energies of the systems. This could be attributed to the increase in atoms and thus, increased in bonding within the complexes and to the cobalt surface. OMn(OH) shows a total energy of -307.5 eV compared to O_2Mn with a total energy of -303.8 eV. A similar trend was observed with $OMn(OH)_2$ with a total energy of -318.1 eV while O_3Mn only result in a total energy of -310.3 eV. In direct comparison with O_3Mn, $O_2Mn(OH)$ also shows a lower total energy of -314.6 eV. Though the hydroxyl-based O_xMn ligands have lower total energies to O_xMn-only ligands, their viability for formation under Fischer-Tropsch conditions need to be assessed.

Geometrically, the addition of oxygen atoms and hydroxyl groups also has an impact on the O-Mn bond length. Comparing OMn to OMn(OH) and O_2Mn, a decrease in O-Mn bond length from 1.946 Å to 1.937 Å and 1.940 Å respectively was observed. Further addition of oxygen and hydroxyl groups to form O_3Mn and $OMn(OH)_2$ had the opposite effect and resulted in the increase of O-Mn bond length to 1.985 Å and 2.002 Å respectively. Finally, combining the addition of oxygen and hydroxyl to the base case to form $O_2Mn(OH)$ resulted in O-Mn bond length of 1.975 Å and 1.942 Å.

3.3.3. Phase diagram of manganese ligands

To accurately model the promoted catalyst system, the ligand configurations in Figure 3-4 need to be subjected to a thermodynamic assessment to identify the viable ligand under Fischer-Tropsch conditions. This was achieved by constructing a phase diagram based on the free energy of formation of the ligands from ultrahigh vacuum (DFT output) to Fischer-Tropsch relevant temperatures and pressures. In the aspect of ensuring the validity of the calculated free energies of formation, the total energies of the ligand configurations and the gaseous components were first corrected to factor the change in temperature and pressure using thermodynamic contributions to enthalpy and entropy (see section 2.5.4), Table 3-4

Table 3-4: Gibbs free energy values for component i at 500 K, 1 bar. Ligand reference state in bold.

Component(i)	***G_i (500K, 1 bar) (eV)***
OMn	**-296.2**
OMn(OH)	-307.5
O_2Mn	-303.7
$O_2Mn(OH)$	-314
O_3Mn	-310.2
$OMn(OH)_2$	-317.8
H_2	-7.828
H_2O	-15.06

Using the stoichiometries defined by Equation 3-3 to Equation 3-7 and the Gibbs free energies of the components under Table 3-4, the Gibbs free energy of formation of each ligand configuration at 500 K was calculated using Equation 3-8. It should be noted that the free energy of formation of the ligands were evaluated with OMn as reference state. Since under Fischer-Tropsch conditions, the partial pressures of gaseous H_2 and H_2O vary over time along the reaction pathway, the dependence of the formation of the ligands with respect to the chemical potential of the gases was given by Equation 3-9.

$$G_{form,i}(T) = G_i(T) + xG_{H_2} - G_{OMn}(T) - yG_{H_2O} \qquad \textit{Equation 3-8}$$

$$E_{form,i}(T,P) = G_{form,i}(T) + x\mu_{H_2} - y\mu_{H_2O} \qquad \textit{Equation 3-9}$$

The free energy of formation of each ligand ($E_{form,i}$), was then plotted as function of the chemical potential (μ) of H_2 and H_2O as show by the 3-dimentional plot, Figure 3-5[A]. Since only the most stable configurations at 500 K are of interest, the phase diagram was generated by considering the only regions defined by the lowest energy structures (view the 3D plot from below) as shown in Figure 3-5[B].

To visualise the dependency of the formation of the ligands on the partial pressure of the gases, the chemical potential scale was converted into a pressure scale for a temperature of 500 K and the phase diagram given by Figure 3-6 was generated. From Figure 3-6, at an operating temperature of 500 K, OMn, O_2Mn and O_3Mn are the predominant configurations for the O_xMn ligands and although the hydroxyl configurations (Figure 3-4) have a lower total electronic energy, their formation by the addition of water to oxide cluster (co-generating hydrogen) is not likely due to the stability of water. Factoring in the partial pressure parameter, at high partial pressures of H_2 and very low partial pressures of H_2O which are the typical starting conditions in the reactor, OMn is the dominant ligand. As the partial pressure of H_2O increases and that of H_2 decreases, the likely conditions of ongoing Fischer-Tropsch synthesis reactions in a reactor, it can be suggested that the Mn promoter exists as the O_2Mn ligand. Finally, at very high partial pressures of H_2O and very low partial pressures of H_2, O_3Mn will be the dominant ligand. Using experimental operating conditions by [104] and theoretical Fischer-Tropsch conditions by [68], an operating region as shown in Figure 3-6 was defined. Hence, it could be suggested that the manganese ligands adopt the O_2Mn configuration under desired operating temperature and pressure.

Consequently, for this study both the OMn and O_2Mn ligand configurations were considered to provide insights on the promotional effects ranging from reactor start to equilibrated reactor conditions. For the O_3Mn, due to its formation under undesirable Fischer-Tropsch operating conditions, it was decided not to be included for the study.

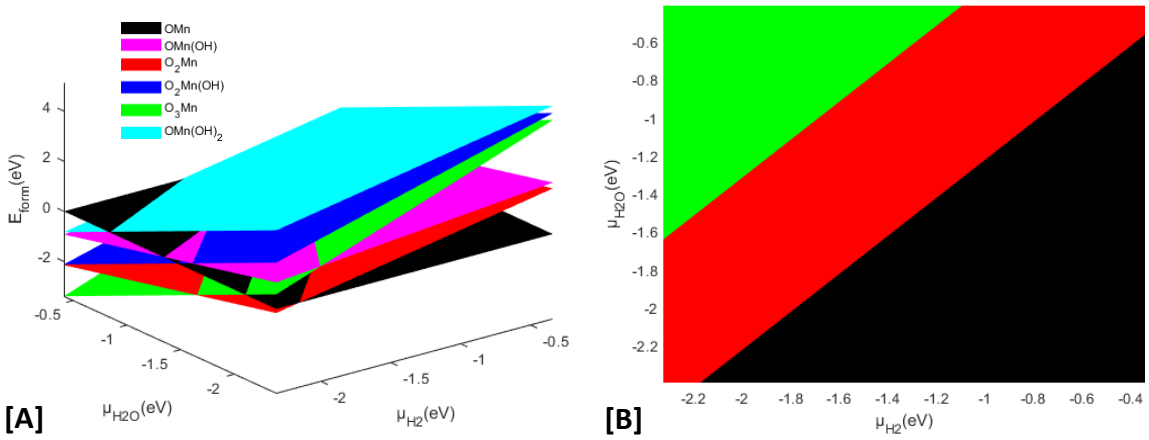

Figure 3-5: Phase diagram of all possible O_xMn configurations on p(3x3) Co(111) slab at 500 K. [A] 3D-plot of phase diagram with respect to chemical potentials of H_2 and H_2O. [B] phase diagram at minimum E_{form} with respect to chemical potentials of H_2 and H_2O

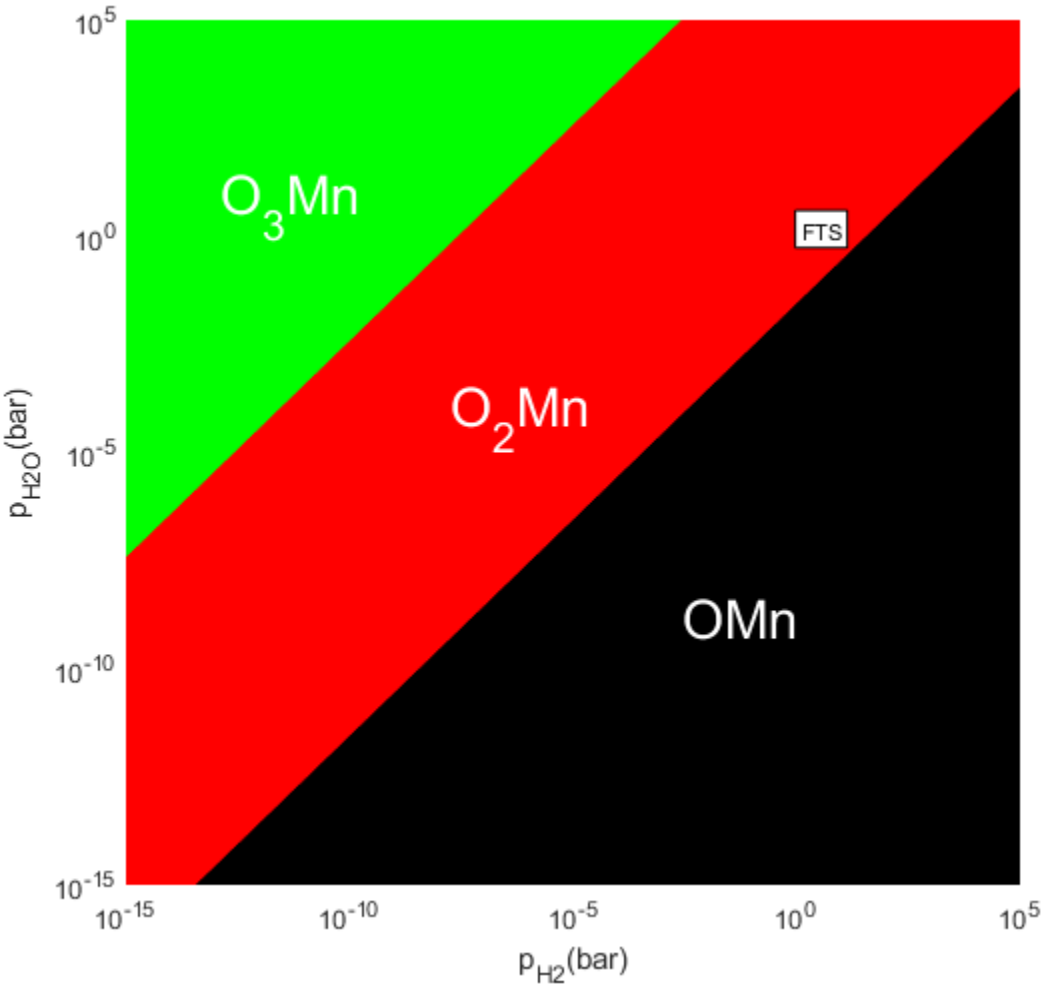

Figure 3-6: Phase diagram for O_xMn ligand formation at 500 K as a function of the partial pressures of H_2 and H_2O. Fischer-Tropsch synthesis (FTS) region represents typical range of operating partial pressures of the gases at 500 K

3.3.4. Charge analysis of Mn in manganese ligands

To quantify the charge distribution in the ligand systems, an atomic population analysis method had to be chosen to generate DFT-based Net Atomic Charges (NACs). Bader's quantum chemical topology (QCT) [105] has been previously applied for DFT-based charge analysis [106]–[109] due to its many desirable properties but it was found to yield non-atomic electron distributions in materials with non-nuclear attractors [110]. To minimised the inclusion of undefined NACs, the DDEC6 atomic population analysis method was chosen instead [111] [112] which is a refinement of the previous Density Derived Electrostatic and Chemical (DDEC) approach. This method is an explicit functional of the electron and spin distributions [110] and can be used to quantify the NAC for an atom A (q_A) as function of the nuclear charge (z_A) and number of electrons (N_A) assigned to it. The DDEC6 NACs can be defined as follows:

$$q_A = z_A - N_A \qquad \textit{Equation 3-10}$$

VASP was used to perform all-electron frozen-core calculations with the inclusion of scalar relativistic effect [110][113] on the full systems while ensuring that sufficient k-points have been considered to converge the required material properties for the systems. DDEC6 NACs was then calculated based on the VASP output using CHARGEMOL program [114] and reported under Table 3-5.

It can be noted that the NACs reported under Table 3-5 are much lower than the typical charges of Mn in oxidic forms reported in literature. This is because the latter reports formal charges which only accounts for ionic bonds in contrast to effective charges that take into account both ionic and covalent bond contributions [115]. Therefore, based on the number of bonds and the NAC is increasing stepwise, a theoretical formal charge of +1, +2 and +3 can be assigned of Mn in the respective species.

Table 3-5: NAC (q_A) of Mn in the O_xMn ligands on Co(111)

Species(i)	***NAC***
OMn	0.53
O_2Mn	0.70
OMn(OH)	0.71
O_3Mn	0.95
$O_2Mn(OH)$	0.83
$OMn(OH)_2$	0.86

3.4. Co-adsorption of species with manganese ligands

With the goal of understanding the effects of Mn on Co-based Fischer-Tropsch synthesis, the different species involved in key Fischer-Tropsch reactions were co-adsorbed with the chosen O_xMn ligands from section 3.3.3 (either OMn or O_2Mn). Though several unique sites on the Co-O_xMn slabs were probed with the various species, only the lowest energy configurations in close proximity of the ligands were reported in Figure 3-7. The stabilities of these configurations were validated though vibrational analyses whereby no imaginary frequencies were found (Appendix C.1). Therefore, the effect of Mn on the adsorption geometries and energies of the Fischer-Tropsch species could be determined. Using the same gas/radical reference states under Table 3-2 and that of the promoted surfaces, Table 3-6, Equation 3-1 was applied to calculate the adsorption energies of the various species on the promoted p(3x3) Co(111) surface, Table 3-7.

Table 3-6: Total energies of reference states for co-adsorption energy calculations inclusive of ZPE corrections

Reference state	$E_{total+zpe}$ ***(eV)***
Co(111)-OMn	-296.1
Co(111)-O_2Mn	-303.6

Table 3-7: Adsorption energies of various species on promoted p(3x3) Co(111) using reference states, CO_g, H_{2g}, H_2O_g and comparable promoted surfaces from literature. Note that co-adsorption energies from literature use different reference states

	$E_{ads,zpe}$(eV)		E_{ads}
Species	**OMn[a]**	**O_2Mn[b]**	**Literature**
C	-0.634	-0.225	-7.43[c], -8.15[d], -8.05[e],
CO	-1.829	-1.097	-2.13[c], -2.55[d], -3.52[e], -1.35[f]
H	-0.183	-0.196	-3.25[c], -3.75[d], -2.92[e], -2.61[f]
O	-0.609	0.416	-6.19[c], -7.27[d], -6.69[e]
OH	-0.696	-0.204	-4.56[e], -3.33[f],
H_2O	-0.656	-0.322	-0.549[f], -2.21[g]

[a/b] p(3x3) O_xMn-Co(111), RPBE functional, VASP code, [c] p(2x2) Co/Mn/Co(111), PBE functional, VASP code [11], [d] p(2x2) Mn/Co(111), PBE functional, VASP code [11], [e] p(3x3) MnO-Co(111), PBE functional, VASP code [41], [f] p(3x3) 6-MnO-Co(111), PBE functional, VASP code [40], [g] p(2x2) MnO-Co(111), PBE functional, VASP code [41]

OMn + C	*OMn + CO*	*O_2Mn + C*	*O_2Mn + CO*
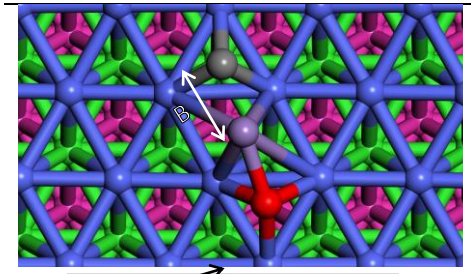	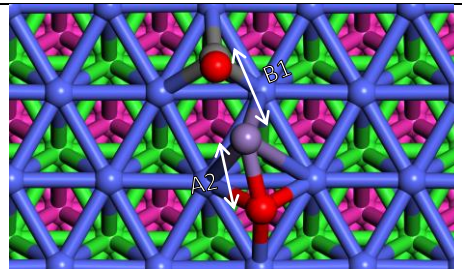	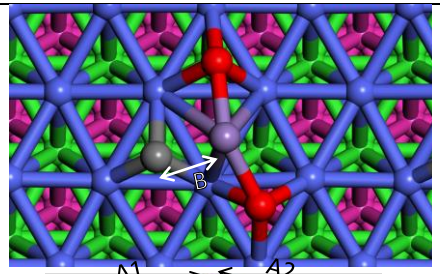	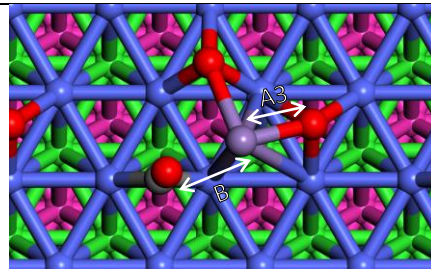
[A] 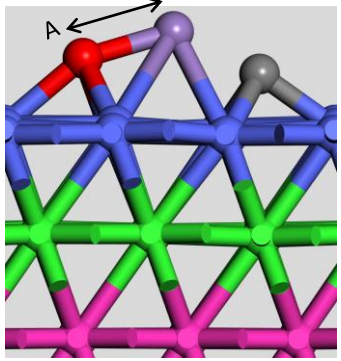	**[B]** 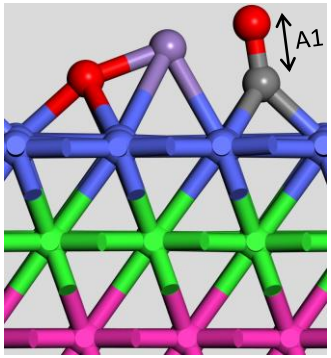	**[C]** 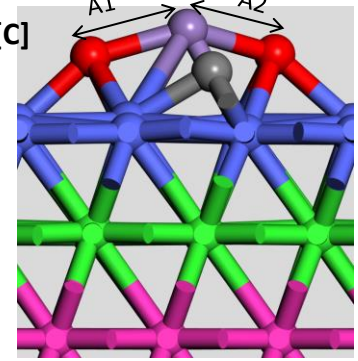	**[D]** 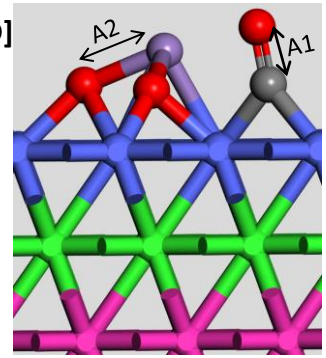
$d_{O\text{-}Mn}$ (A) (Å) 1.944 $d_{adsorbate}$ (B) (Å) 1.963	$d_{C\text{-}O}$ (A1) (Å) 1.282 $d_{O\text{-}Mn}$ (A2) (Å) 1.890 $d_{adsorbate}$ (B1) (Å) 1.998	$d_{O\text{-}Mn}$ (A1) (Å) 1.963 $d_{O\text{-}Mn}$ (A2) (Å) 1.947 $d_{adsorbate}$ (B) (Å) 2.156	$d_{C\text{-}O}$ (A1) (Å) 1.259 $d_{O\text{-}Mn}$ (A2) (Å) 1.947 $d_{O\text{-}Mn}$ (A3) (Å) 2.274 $d_{adsorbate}$ (B) (Å) 2.075

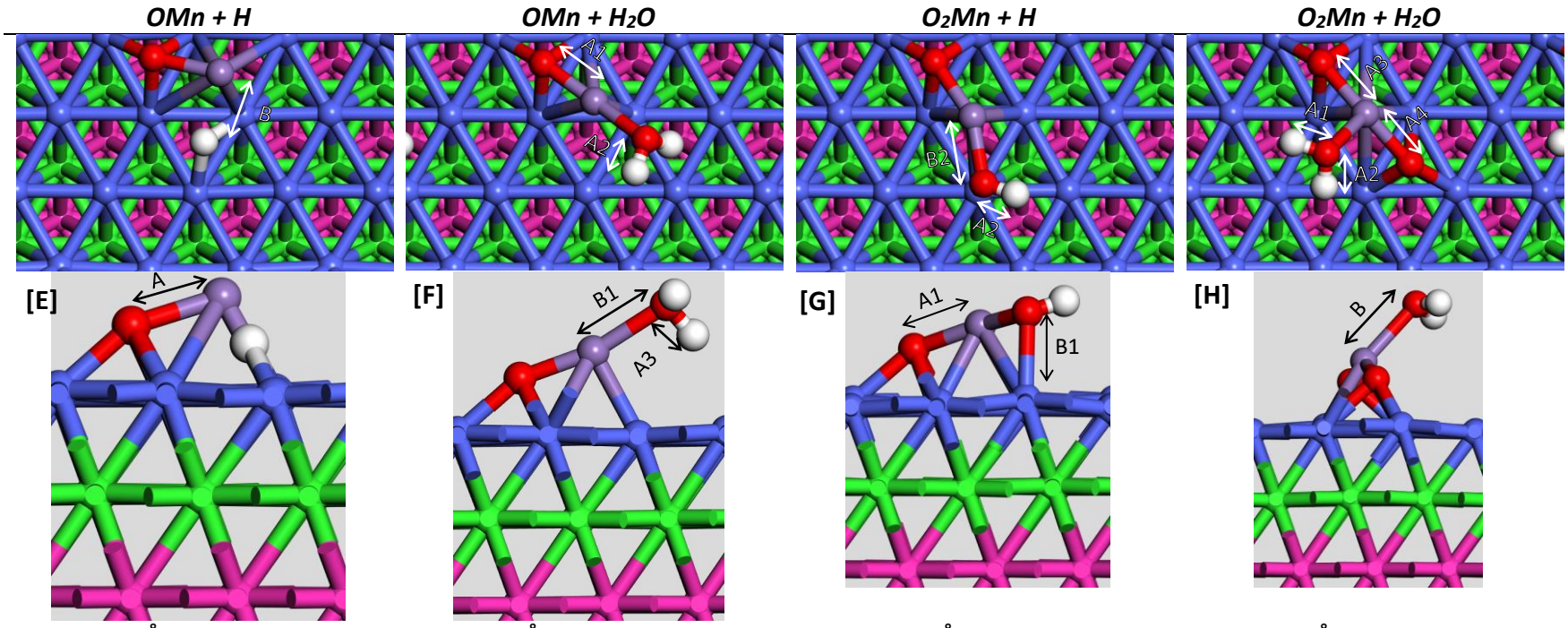

$d_{O\text{-}Mn}$ (A) (Å)	1.994
$d_{adsorbate}$ (B) (Å)	2.168

$d_{O\text{-}Mn}$ (A1) (Å)	1.889
$d_{O\text{-}H}$ (A2) (Å)	0.979
$d_{O\text{-}H}$ (A3) (Å)	0.998
$d_{adsorbate}$ (B1) (Å)	2.116
Bond angle (H_2O) (°)	104.1

$d_{O\text{-}Mn}$ (A1) (Å)	1.937
$d_{O\text{-}H}$ (A2) (Å)	0.975
$d_{adsorbate}$ (B1) (Å)	2.198
$d_{adsorbate}$ (B2) (Å)	1.905

$d_{O\text{-}H}$ (A1) (Å)	0.977
$d_{O\text{-}H}$ (A2) (Å)	0.979
$d_{O\text{-}Mn}$ (A3) (Å)	1.958
$d_{O\text{-}Mn}$ (A4) (Å)	1.964
$d_{adsorbate}$ (B) (Å)	2.290
Bond angle (H_2O) (°)	104.5

Figure 3-7: Lowest energy configurations of Fischer-Tropsch species co-adsorbed in proximity of OMn and O_2Mn ligands on p(3x3) Co(111) slab. Atoms represented by C, H, O, Mn, Co in first/forth/fifth layer, Co in second and Co in third layer.

Very few theoretical studies have addressed the promotional effects of Mn on Fischer-Tropsch synthesis species owing to the lack of information on the structure of the promoter complex on the cobalt surface. The calculated adsorption energies of the various species on the OMn and O_2Mn promoted slabs display significant differences to those from literature primarily due to the various configurations used for the Mn promoter and the varying species used as gaseous reference states.

Early DFT-based studies on Mn promoter involved manganese as either a subsurface monolayer(Co/Mn/Co) or as a top monolayer(Mn/Co) [11]. As with the case of the clean Co(111) slab, the calculated adsorption energies for C, H, and O on the OMn and O_2Mn slabs are much higher than those reported in literature owing to different reference states. With gaseous radicals as reference states in addition to the promoted surfaces, the adsorption of C and O were more comparable as shown in Table 3-8. Contrasting the data, the trends in co-adsorption energies of the ligand-based systems falls in between and fell in-between the subsurface monolayer and top monolayer models. For the co-adsorption of CO, the monolayer systems report lower adsorption energy in the range of 0.3-1.4 eV than our ligand systems. This might be attributed to the enhanced stabilising effect of the monolayer in comparison to a single Mn atom in the oxidic ligands. Though, the Co-Mn alloy model by Pedersen [11] did support the enhanced adsorption of C, CO, H and O in comparison to a clean slab, the accuracy of the model could not be supported as XPS results suggest that Mn rather exists as Mn^{2+} instead of metallic Mn on the catalyst surface [11]. Furthermore, the use of monolayer model induced additional source of error as the manganese atoms might not be able to relax into their most stable positions due to the periodic nature of the system where neighbouring unit cells may induced a large degree of lateral interactions. Hence, introducing the possibility of the monolayers being compressed.

The recent models on the other hand, considered the oxidic phase of Mn on the cobalt surface [41], [40]. Comparing the adsorption of C, O, H and OH in the presence of the MnO promoter by Pedersen et al. [11], we can note significant disparity of at least 3 eV which is linked to the used of gaseous radicals as reference state. The re-calculated adsorption energies with radicals in the reference state, provided comparable co-adsorption energies of C, O and OH on MnO_x promoted Co(111) surfaces, Table 3-8. Although CO also adsorbed preferentially at an hcp site in proximity of the MnO model by Gençoğlu [41], it experiences a higher degree of stabilisation due to the linear nature of the latter MnO complex. Co-adsorption of H_2O with MnO, re-configures the complex to mimic the geometry under Figure 3-7[F]. While we expect a similar degree of co-adsorption, the model by Gençoğlu [41], show extensive stabilisation with an co-adsorption energy of -2.21 eV. We attribute this to the smaller p(2x2) slab where the oxygen from MnO in the neighbouring cell creates a wire-like chain with the water molecule. Thus, with the additional bonds formed, we can explain much lower adsorption energy.

For the case of the 6-MnO ring promoter model by Doorslaer [40], similar disparities in co-adsorption energies due to differences in gaseous reference states can be noted (reviewed under , Table 3-8) with the exception of CO and H_2O. The ring MnO structure, seems provide a stabilisation effect that is in-between the OMn and O_2Mn ligands. We can link this observation to geometry of each MnO in the ring being similar to OMn used for our study and the fact that each adsorbate only interacted with a single MnO from the ring structure.

Table 3-8: Adsorption energies of various species on Co(111) using modified reference states, C_g, H_g, O_g, OH_g and comparable promoted surfaces from literature.

	$E_{ads,zpe}$ (eV)		E_{ads} (eV)
Species	**OMn[a]**	**O_2Mn[b]**	**Literature**
C	-7.83	-7.42	-7.43[c], -8.15[d], -8.05[e],
CO	-1.83	-1.10	-2.13[c], -2.55[d], -3.52[e], -1.35[f]
H	-6.65	-6.66	-3.25[c], -3.75[d], -2.92[e], -2.61[f]
O	-7.37	-6.35	-6.19[c], -7.27[d], -6.69[e]
OH	-3.59	-3.10	-4.56[e], -3.33[f],
H_2O	-0.66	-0.32	-0.549[f], -2.21[g]

On an overall picture of adsorption of FTS species, the presence of Mn-promoter, most studies reached the same conclusion, i.e a lowering of the co-adsorption energies. We only note this effect for C, CO, O, OH and H_2O on OMn promoted Co(111) and for OH and H_2O on O_2Mn promoted Co(111).

4. CO dissociation species on Co(111)

4.1. Introduction

CO dissociation is a crucial step in the Fischer-Tropsch synthesis process as it provides the carbon source for hydrocarbon formation which via surface polymerisation. While there is a general consensus on manganese promotional effects, which include: 1) improved catalytic activity, 2) increased selectivity towards C_{5+} while suppressing CH_4 formation and 3) improved the adsorption of CO while increasing H_2 uptake and the retardation of Co reduction [11], [116]-[117], little work has been done on understanding the mechanism behind those promotional effects. In an attempt to quantify and qualify these effects, recent studies have confirmed that Mn exists as MnO_x on the surface of the Co catalyst [12]-[14], [40], [67], [69], and they all suggest that the promoter may have an impact on CO adsorption and dissociation products. While most studies focused on direct CO dissociation, manganese may also have an impact on the H-assisted CO dissociation(due to the former's high activation barrier on Co(111)) [12]. To quantify the effect of Mn on CO dissociation, the evaluation of the adsorption strength of the reactants and products can be considered as a viable method for theoretical studies. It is also worth noting that the surface coverage of the adsorbed species is an important criterion to consider when probing adsorption strength. Under Fischer-Tropsch reaction conditions, high CO coverage is typically expected and will induce larger degree of lateral interactions. Under such high coverage cases, observations regarding CO dissociation is minimal as CO will rather desorb than dissociate owing to the elevated barrier [81], [118]. To ensure the reliability of the calculations, theoretical studies for the adsorption of CO and its dissociated state, are primarily carried under low coverage conditions from 1/9 ML to 1/4 ML. Thus, ensuring that negligible lateral interaction between the species are present and the correct adsorption geometries can be reported [81]. Here we will report the adsorption geometries and energies of the reactants/products of CO dissociations on both clean and promoted p(3x3) Co(111) slabs at a coverage of 1/9 ML and compare them to literature.

4.2. CO dissociation species on clean Co(111)

The description of CO dissociation on Co(111) is incomplete with just adsorption of isolated CO dissociation species as reported in chapter 3.2. Hence, the adsorption of the reactants and resulting products was also, included in the study. To evaluate the adsorption energies of the CO dissociation species(reactants and products) on the Co(111), Equation 3-1 was applied in combination with the relevant stoichiometric coefficients listed under Table 4-1 and the total energies of the corresponding molecules or free radical in the gas phase listed under Table 3-2. As previously mentioned, ZPE corrections based on the vibrational modes of the adsorbates and gaseous molecules/radicals were also included in the total energies reported under Table 3-2.

Table 4-1: Stoichiometric coefficients the calculation of adsorption energies for the adsorption models

Adsorbate	*a*	*b*	*c*
CO	0	1	0
C + O	-2	1	0
HCO	0.5	1	-1

CH + O	0.5	1	0

4.2.1. Direct CO dissociation species

The atop, bridge, fcc and hcp sites on the Co(111) surface were probed and it was found that CO adsorption on the hcp site, Figure 4-1[A], resulted in the lowest adsorption energy of -1.37 eV. Upon immediate dissociation of CO, both carbon and oxygen adsorb on adjacent hcp sites as shown in Figure 4-1[B], but the proximity of the two atoms induces increased atomic repulsion forces which result in an adsorption energy of 0.27 eV. To obtain a stable configuration of the dissociated state, the oxygen atom can diffuse to a further fcc position, Figure 4-1[C] or the carbon atom diffuses to a further fcc position, Figure 4-1[D]. The more stable configurations of the dissociated state resulted in adsorption energies of -0.168 and -0.25 eV respectively. Although literature reports the same dissociated configurations of carbon and oxygen(in terms of sites on Co(111)), the adsorption energies were evaluated at a higher value of -12.7 eV and -12.1 eV respectively Gençoğlu [41]. This large disparity in the co-adsorption energies could be primarily attributed to difference in reference state whereby carbon and oxygen radicals in the gaseous phase was considered by Gençoğlu [41]. The adsorption energies of [B], [C] and [D] were adjusted with carbon and oxygen radicals in the gas phase, and we hence report adsorption energies of -13.7 eV, -14.1 and -14.2 eV. With the disparity in the reference states addressed, we can suggest that some degree of repulsive forces between neighbouring adsorbates in the repeating p(2x2) unit cells used by Gençoğlu [41] is present, thus accounting for the higher adsorption energies.

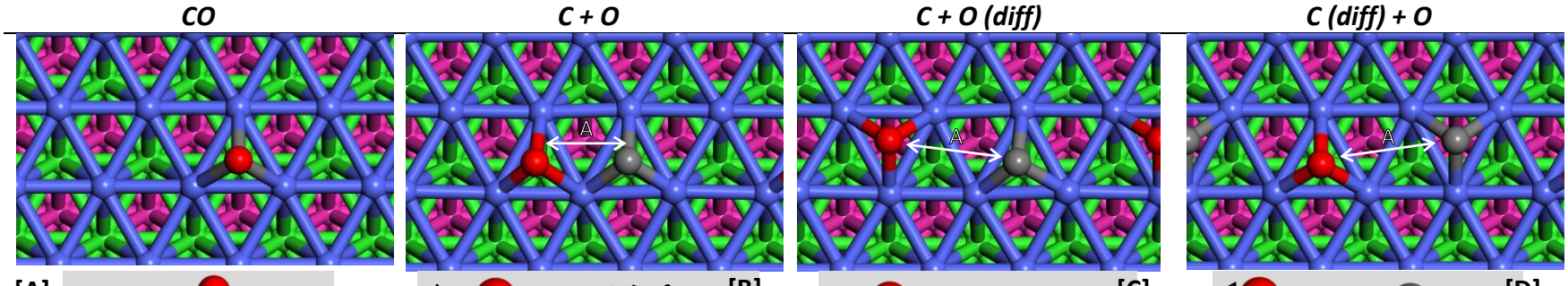

$E_{ads+zpe}$ (eV)	-1.37	$E_{ads+zpe}$ (eV)	0.27	$E_{ads+zpe}$ (eV)	-0.17	$E_{ads+zpe}$ (eV)	-0.25
d_{C-O} (A) (Å)	1.203	d_{C-O} (A) (Å)	2.586	d_{C-O} (A) (Å)	3.625	d_{C-O} (A) (Å)	3.821
$d_{adsorbate}$ (B) (Å)	1.99	$d_{adsorbate}$ (B1) (Å)	1.797	$d_{adsorbate}$ (B1) (Å)	1.866	$d_{adsorbate}$ (B1) (Å)	1.866
		$d_{adsorbate}$ (B2) (Å)	1.724	$d_{adsorbate}$ (B2) (Å)	1.787	$d_{adsorbate}$ (B2) (Å)	1.774

Figure 4-1: Lowest energy configuration of direct CO dissociation reactants and products on p(3x3) Co(111) at an initial coverage of 1/9 ML. CO dissociation products based on the initial position under [A]. Atoms represented by C, O Co in first/forth/fifth layer, Co in second and Co in third layer.

4.2.2. H-assisted CO dissociation species

HCO configurations were generated by adsorbing a carbon atom at the different sites on the surface and the hydrogen and oxygen atoms bonded directly atop with an initial HCO bond angle of 115°. Upon performing geometric optimisations of the initial geometries, the starting bridge site resulted in the lowest energy configuration as show in Figure 4-2[A] whereby the carbon and oxygen atoms occupy bridge sites with the hydrogen atom atop carbon at an HCO bond angle of 114.3 °. The adsorption energy of HCO on the Co(111) surface was evaluated at -0.39 eV which is significantly less stable than that reported in literature with a range of -2.15 to -2.18 eV [41]. The significant disparity could be associated with the choice of reference state; in contrast to having CO, H_2 and H_2O in the gas phase which is typical under Fischer-Tropsch reactor condition, the study by Gençoğlu [41] considered HCO in the gaseous state. The dissociated state of the reactant was obtained by cleaving the C-O bond of the adsorbate and diffusing the oxygen atom to an adjacent hcp site. The repulsive forces between O and CH in the immediate dissociated state causes the CH adsorbate to diffuse to an hcp position as shown in Figure 4-2[B]. The adsorption energy of the dissociated state was hence evaluated at -1.01 eV in comparison to the adsorption energy of -12.2 eV reported by Gençoğlu [41] whereby CH + O, CH and O in the gas phase along with a smaller p(2x2) slab were used as reference states. The adsorption energies of [A] and [B] were adjusted with HCO, CH and O radicals in the gas phase, and we hence report adsorption energies of -1.67 eV and -12.8 eV which are in agreement with literature.

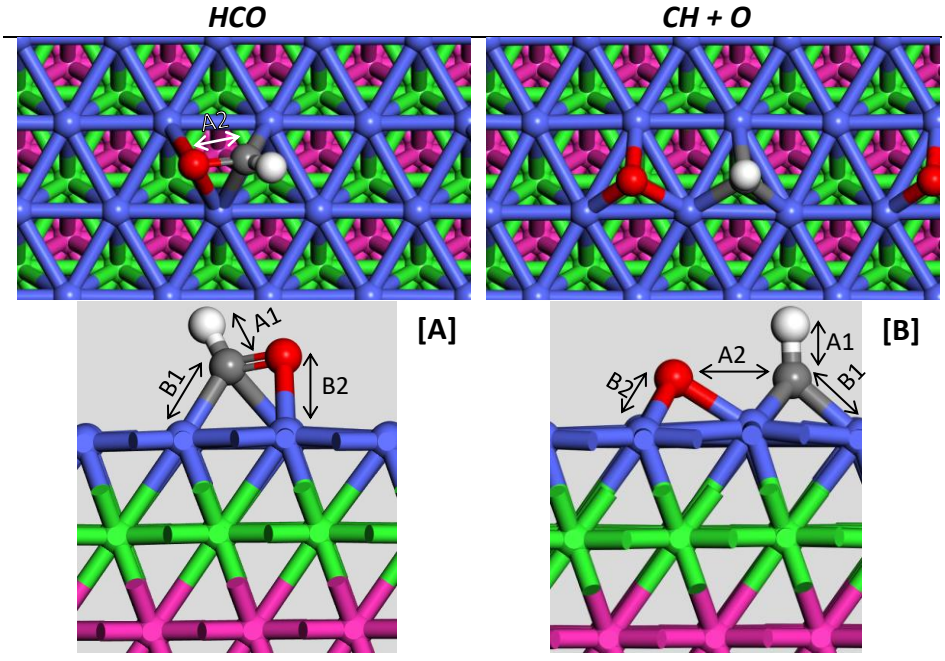

$E_{ads+zpe}$ (eV)	-0.39	$E_{ads+zpe}$ (eV)	-1.01
d_{C-H} (A1) (Å)	1.109	d_{C-H} (A1) (Å)	1.103
d_{C-O} (A2) (Å)	1.328	d_{C-O} (A2) (Å)	2.879
$d_{adsorbate}$ (B1) (Å)	1.882	$d_{adsorbate}$ (B1) (Å)	1.840
$d_{adsorbate}$ (B2) (Å)	2.138	$d_{adsorbate}$ (B2) (Å)	1.881
Bond angle-HCO (°)	114.3		

Figure 4-2: Lowest energy configuration of H-assisted CO dissociation reactants and products on p(3x3) Co(111) at an initial coverage of 1/9 ML. H-assisted CO dissociation products based on the initial position under [A]. Atoms represented by C, H, O, Co in first/forth/fifth layer, Co in second and Co in third layer.

4.3.CO dissociation on MnO_x promoted Co(111)

For CO dissociation on promoted p(3x3) Co(111) slabs, the co-adsorption energies of the reactants and products in the presence of OMn and O_2Mn were evaluated using Equation 3-1 and the stoichiometric coefficients listed under Table 4-1. While the gaseous reference states remained unchanged, the surface reference state listed under Table 3-6 was instead used.

4.3.1. Direct CO dissociation

The presence of the promoters offers two distinct effects on the adsorption energies of CO on the metal surface. Compared to the adsorption energy of CO on the clean slab of -1.35 eV, the presence of OMn stabilises CO with an elongated bond, resulting in a co-adsorption energy of -1.84 eV, Figure 4-3[A]. Co-adsorption with O_2Mn, on the other hand, results in a less stable adsorption of a CO molecule with a weakened C-O bond, as indicated by a smaller binding energy of -0.94 eV., Figure 4-4[A]. The same observation can be made for the immediate dissociated products whereby the presence of OMn as shown in Figure 4-3[B], offered improved adsorption of the species with a co-adsorption energy of -0.56 eV versus -0.17 eV on the unpromoted slab. While in the unpromoted case, diffusion of the carbon atom to a further fcc position resulted in a more stable configuration, in the case of OMn the diffusion shown in Figure 4-3[C] impaired the adsorption strength of the species. This resulted in a smaller adsorption energy of -0.44 eV due to the repulsive forces between the carbon atom and the OMn ligand in the adjacent cell. The presence of O_2Mn, resulted in an unstable state of the dissociated products given by a co-adsorption energy of 0.62 eV. To stabilise the dissociated state, the carbon atom can diffuse to a fcc position in proximity to the O_2Mn ligand, Figure 4-4[C], and hence, bringing the adsorption energy of the dissociated state of 0.13 eV. But the repulsive lateral interactions are still significant in the O_2Mn model given the restrictive p(3x3) slab. Hence, to obtain a more accurate representation of the effect of O_2Mn on the dissociated state, a bigger p(4x4) slab will be required. The MnO model by Gençoğlu [41] shows a different degree of stabilisation of the dissociated state. The presence of the promoter lead to the co-adsorption energies of C and O at similar sites (in proximity of MnO) of -12.97 eV and -13.76 eV depending on the proximity to the promoter. We should note that latter considered carbon and oxygen radicals in the gaseous phase along with a smaller p(2x2) slab as reference states. The co-adsorption energies of [B] and [C] for both OMn and O_2Mn were adjusted with carbon and oxygen radicals in the gas phase. We hence report co-adsorption energies of -14.5 eV and -14.4 eV for OMn and -13.3 eV and 13.8 eV for O_2Mn. Although, minor differences in the co-adsorption strength of the dissociated species were present, a similar trend was confirmed whereby the presence of the manganese oxide-based promoter improved the co-adsorption energies, translating to a stabilisation effect.

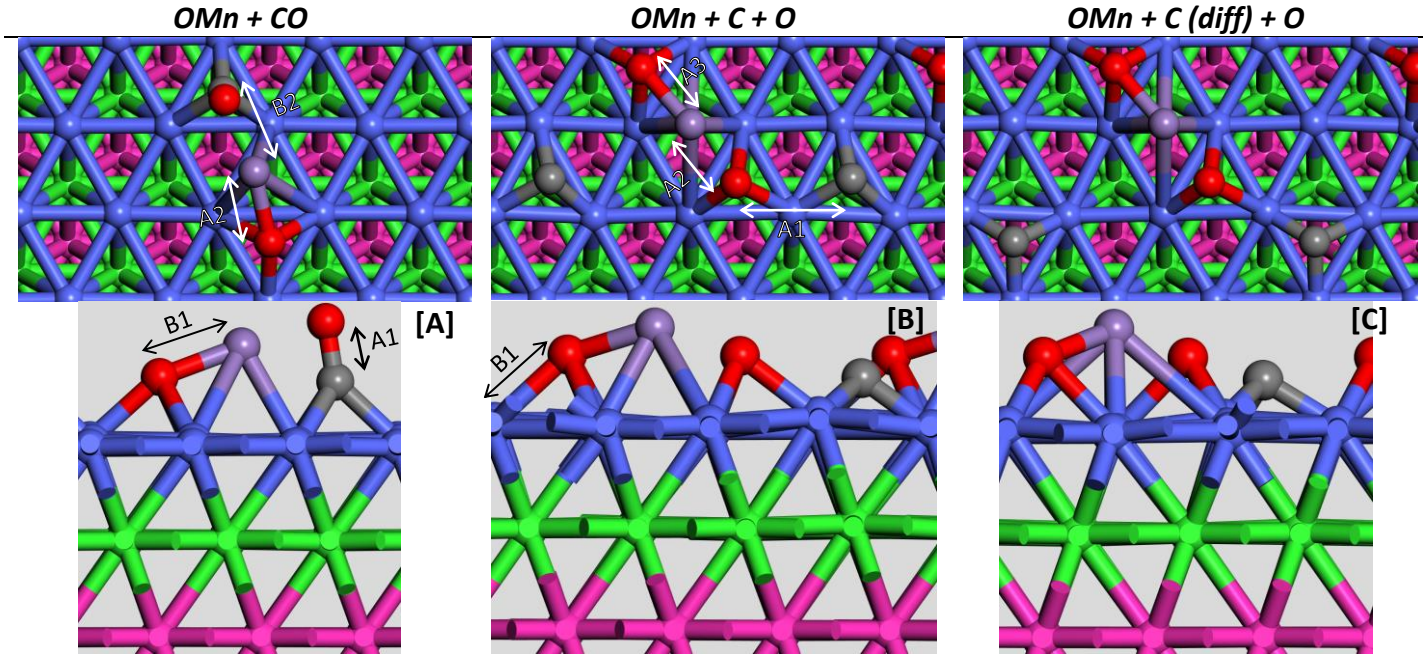

$E_{ads+zpe}$ (eV)	-1.84	$E_{ads+zpe}$ (eV)	-0.56	$E_{ads+zpe}$ (eV)	-0.44
d_{C-O} (A1) (Å)	1.282	d_{C-O} (A1) (Å)	2.911	d_{C-O} (A1) (Å)	3.052
d_{O-Mn} (A2) (Å)	1.890	d_{O-Mn} (A2) (Å)	1.932	d_{O-Mn} (A2) (Å)	1.932
$d_{adsorbate}$ (B1) (Å)	1.991	d_{O-Mn} (A3) (Å)	1.930	d_{O-Mn} (A3) (Å)	1.930
$d_{adsorbate}$ (B2) (Å)	1.998	$d_{adsorbate}$ (B1) (Å)	1.990	$d_{adsorbate}$ (B1) (Å)	1.989

Figure 4-3: Lowest energy configuration of direct CO dissociation reactants and products on a p(3x3) OMn promoted Co(111) slab. Atoms represented by C, O, Mn, Co in first layer, Co in first/forth/fifth layer, Co in second and Co in third layer.

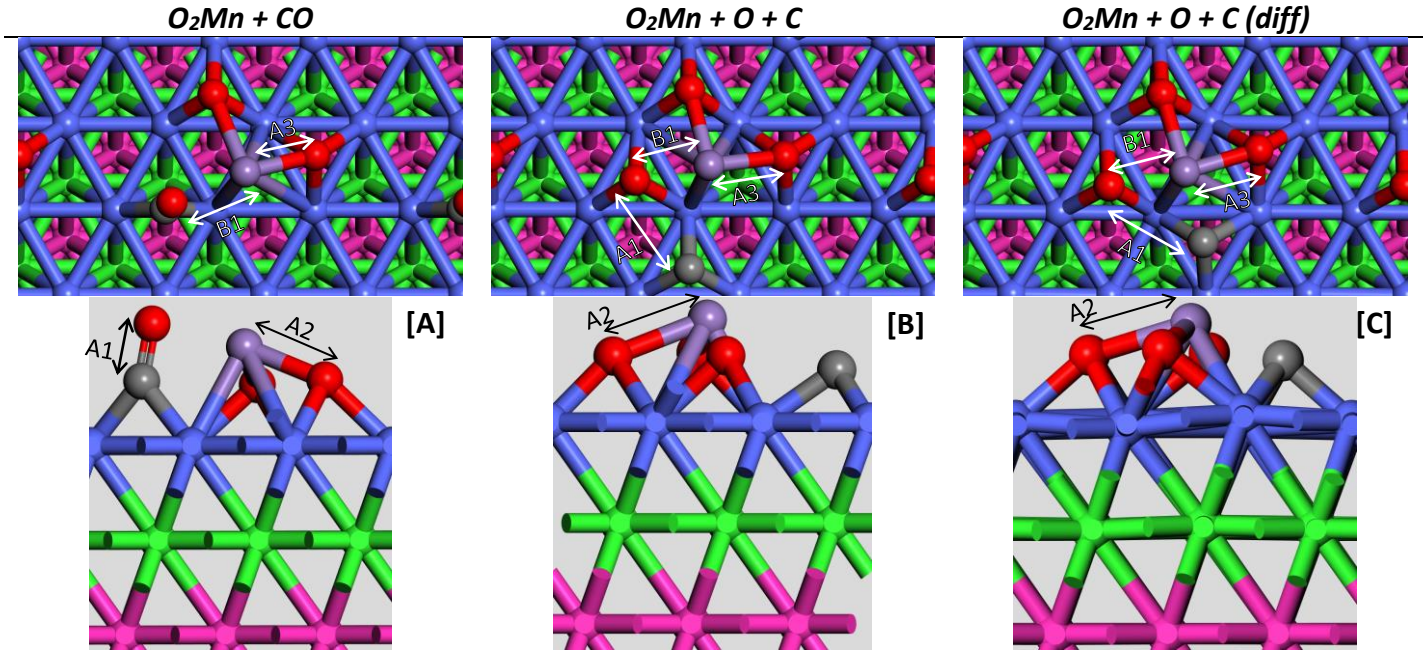

$E_{ads+zpe}$ (eV)	-0.94	$E_{ads+zpe}$ (eV)	0.62	$E_{ads+zpe}$ (eV)	0.13
d_{C-O} (A1) (Å)	1.259	d_{C-O} (A1) (Å)	2.664	d_{C-O} (A1) (Å)	2.785
d_{O-Mn} (A2) (Å)	1.947	d_{O-Mn} (A2) (Å)	2.109	d_{O-Mn} (A2) (Å)	2.141
d_{O-Mn} (A3) (Å)	2.274	d_{O-Mn} (A3) (Å)	2.038	d_{O-Mn} (A3) (Å)	2.001
$d_{adsorbate}$ (B1) (Å)	2.075	$d_{adsorbate}$ (B1) (Å)	2.065	$d_{adsorbate}$ (B1) (Å)	2.038

Figure 4-4: Lowest energy configuration of direct CO dissociation reactants and products on a p(3x3) O_2Mn promoted Co(111) slabs. Atoms represented by C, O, Mn, Co in first/forth/fifth layer Co in second and Co in third layer.

4.3.2. H-assisted CO dissociation

For the OMn promoted system, the minimum energy configuration was given by C adsorbed at a bridge site bonded to an H atom over a bridge site and O over an hcp site, all with an HCO bond angle of 111.9°. On the other hand, the minimum energy configuration on the O_2Mn promoted slab was given by C still at a bridge site but bonded to an H atom over an hcp site and oxygen atom over a bridge site, all with an HCO bond angle of 110.9°. The presence of the promoter offered different effects on the adsorption of HCO on the cobalt surface. As shown in Figure 4-5[A], OMn induced a significant stabilisation HCO on the cobalt surface given by an increased co-adsorption energy of -1.60 eV. O_2Mn on the other, offers the same degree of adsorption as an unpromoted surface, Figure 4-6 [A], and result in an adsorption energy of -0.39 eV. On MnO model by Gençoğlu [41], HCO prefers and hcp adsorption site with an adsorption energy of -2.54 eV with HCO in the gaseous phase as reference state. Adjusting the adsorption of the systems under Figure 4-5 [A] and Figure 4-6 [A] with HCO as reference state, the adsorption energies were evaluated at -2.87 eV and -1.67 eV respectively. We can suggest that the presence OMn ligand offered similar degree of HCO co-adsorption as the MnO model by Gençoğlu [41].

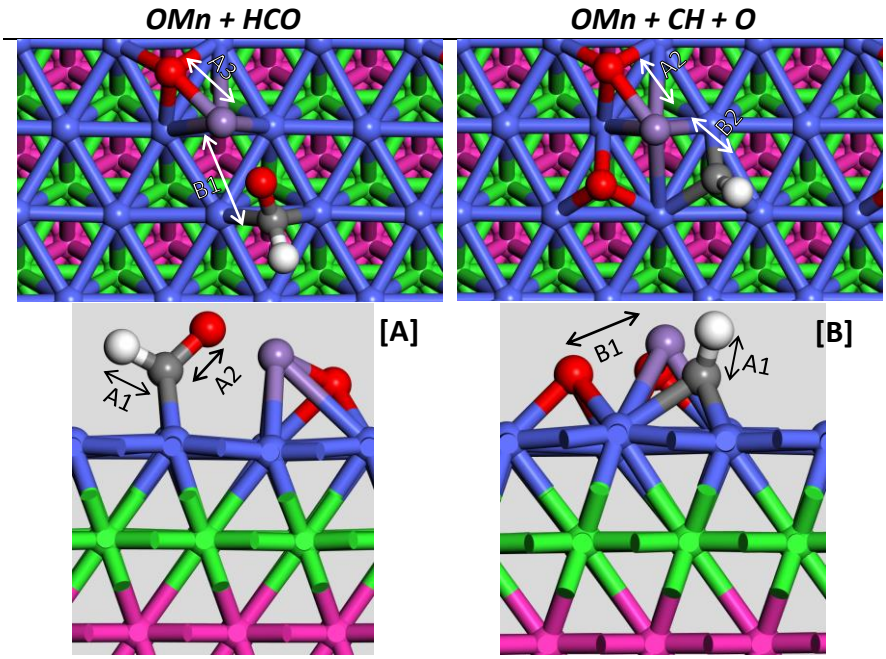

$E_{ads+zpe}$ (eV)	-1.60	$E_{ads+zpe}$ (eV)	-1.86
d_{C-H} (A1) (Å)	1.110	d_{C-H} (A1) (Å)	1.111
d_{C-O} (A2) (Å)	1.327	d_{O-Mn} (A2) (Å)	2.007
d_{O-Mn} (A3) (Å)	1.903	$d_{adsorbate}$ (B1) (Å)	2.024
$d_{adsorbate}$ (B1) (Å)	2.765	$d_{adsorbate}$ (B2) (Å)	2.079
Bond angle-HCO (°)	110.9		

Figure 4-5: Lowest energy configuration of H-assisted CO dissociation reactants and products on a p(3x3) OMn promoted Co(111) slab. Atoms represented by C, H, O, Mn, Co in first/forth/fifth layer, Co in second and Co in third layer.

The presence of OMn (see Figure 4-5 [B]) enhanced the adsorption of the H-assisted CO dissociation products (CH + O) as evidenced by a co-adsorption energy of -1.86 eV in contrast to an unpromoted adsorption energy of -1.01 eV. The presence of O_2Mn (see Figure 4-6[B]) on the other hand induced a weaker co-adsorption energy of -0.76 eV compared to the unpromoted slab. We believe this could be due to the limitation of a p(3x3) slab whereby in the dissociated state, the adsorbates can induce repulsive lateral interactions with each other or the promoter in adjacent repeat units. As a result, migration to a larger slab may offer a more accurate representation of the co-adsorption energy of the dissociated state. The dissociated state on the MnO model by Gençoğlu [41], was reported in the configuration whereby the CH molecule and the O atom are adsorbed in the hcp and atop position respectively with a co-adsorption energy of -13.3 eV. The co-adsorption energies of the OMn and O_2Mn systems under Figure 4-5 [B]and Figure 4-6[B], were adjusted with CH and O radicals in the gas phase. We hence, report co-adsorption energies of -13.6 eV for OMn and -12.5 eV for O_2Mn. We can suggest that the presence OMn ligand offers similar degree of CH + O co-adsorption as the MnO model by Gençoğlu [41].

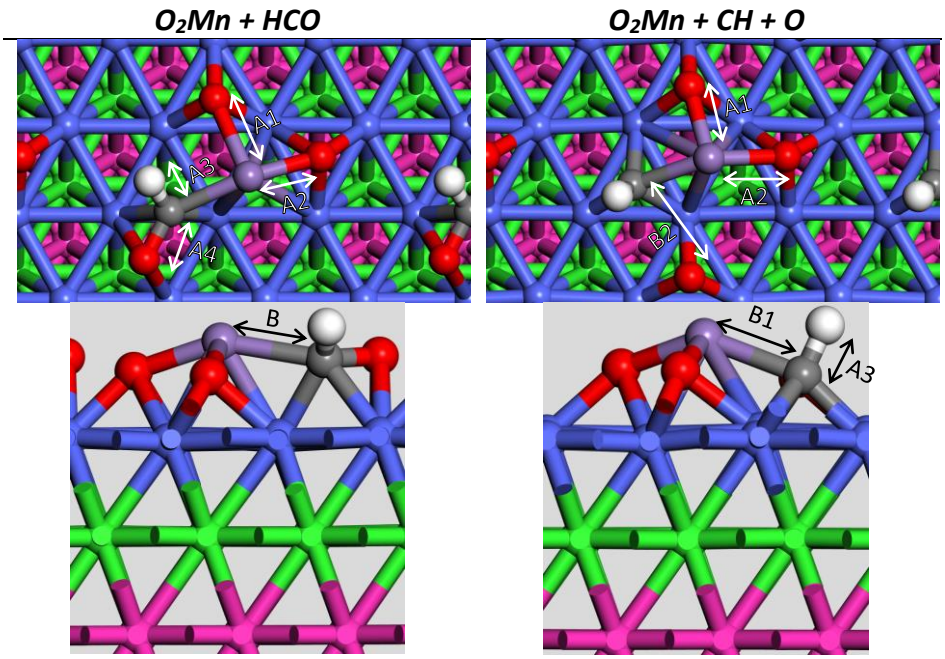

E_{ads} (eV)	-0.39	E_{ads} (eV)	-0.76
$d_{O\text{-}Mn}$ (A1) (Å)	1.958	$d_{O\text{-}Mn}$ (A1) (Å)	1.967
$d_{O\text{-}Mn}$ (A2) (Å)	2.228	$d_{O\text{-}Mn}$ (A2) (Å)	2.017
$d_{C\text{-}H}$ (A3) (Å)	1.120	$d_{C\text{-}H}$ (A3) (Å)	1.113
$d_{C\text{-}O}$ (A4) (Å)	1.358	$d_{adsorbate}$ (B1) (Å)	2.164
$d_{adsorbate}$ (B) (Å)	2.191	$d_{adsorbate}$ (B2) (Å)	2.709
Bond angle-HCO (°)	110.9		

Figure 4-6: Lowest energy configuration of H-assisted CO dissociation reactants and products on a p(3x3) O_2Mn promoted Co(111) slab. Atoms represented by C, H, O, Mn, Co in first/forth/fifth layer, , Co in second and Co in third layer .

We also came to the consensus that OMn on Co(111) leads to improved co-adsorption of H-assisted CO dissociation species compared to bare Co(111). On the hand, O_2Mn on Co(111), weakened the adsorption strength of HCO and the dissociated state CH + O

5. Oxygen removal species on Co(111)

5.1. Introduction

The removal of oxygen as water on cobalt catalysts can occur through the hydrogenation of hydroxyl, the product of the hydrogenation of surface oxygen, or from the disproportionation of two hydroxyl molecules [7], [44]-[45], [121]. Here, we present the adsorption geometries and energies of the reactants/products of the steps involved in the oxygen removal process on both clean and promoted Co(111) slabs and compare them to literature. Thereby, expanding on adsorption of isolated species under chapters 3.2 and 3.4.

5.2. Oxygen removal species on clean Co(111)

To evaluate the adsorption energies of the oxygen removal species(reactants and products) on Co(111), Equation 5-1 was implemented in combination with the relevant coefficients listed under Table 5-1 and the total energies of the hydrogen and water molecules in the gas phase under Table 3-2. As previously mentioned, ZPE corrections based on the vibrational modes of the adsorbates and gaseous molecules/radicals were also included in the total energies reported under Table 3-2. Surface oxygen is produced upon CO dissociation and needs to be removed as it can poison the Fischer-Tropsch catalyst. Therefore, to assess oxygen removal on Co(111), a reference state consisting of a Co(111) slab pre-covered with an oxygen atom on it most stable position, Figure 5-1, was considered. The total energy of the reference slab (E_{slab+O}) was evaluated at -288 eV and was used in conjunction with Equation 5-1.

$$E_{ads,i} = E_{slab+ads} - E_{slab+O} - aE_{H_2} - bE_{H_2O} \qquad \textit{Equation 5-1}$$

Table 5-1: Stoichiometric coefficients the calculation of adsorption energies for the adsorption models

Adsorbate	*a*	*b*
O	0	0
O + H	0.5	0
OH	0.5	0
OH + H	1	0
H_2O	1	0
OH + OH	0	1
H_2O + O	0	1

O	***OH***	***OH + H***
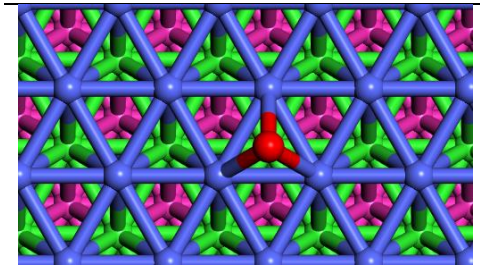	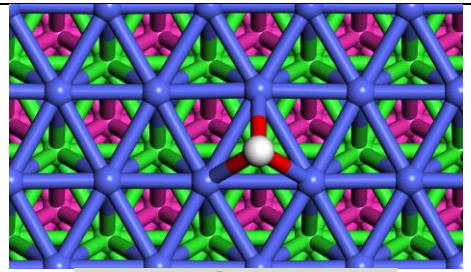	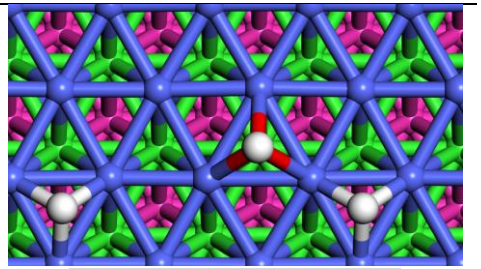
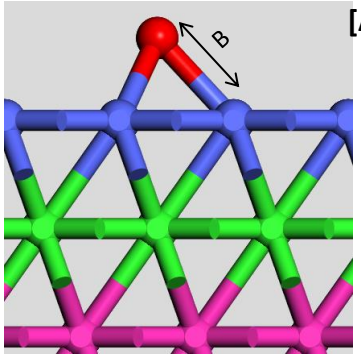 **[A]**	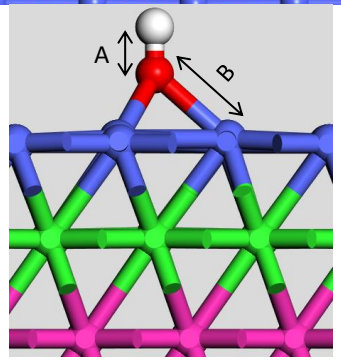 **[B]**	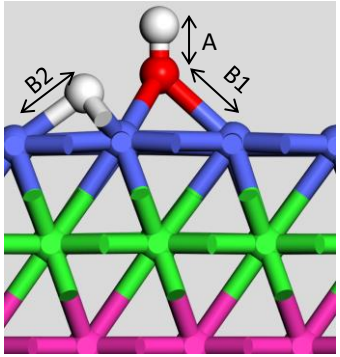 **[C]**
$d_{adsorbate}$ (B) (Å) 1.873	$E_{ads+zpe}$ (eV) -0.18 d_{O-H} (A) (Å) 0.973 $d_{adsorbate}$ (B) (Å) 2.026	$E_{ads+zpe}$ (eV) -0.51 d_{O-H} (A) (Å) 0.973 $d_{adsorbate}$ (B1) (Å) 2. 013 $d_{adsorbate}$ (B2) (Å) 3.062

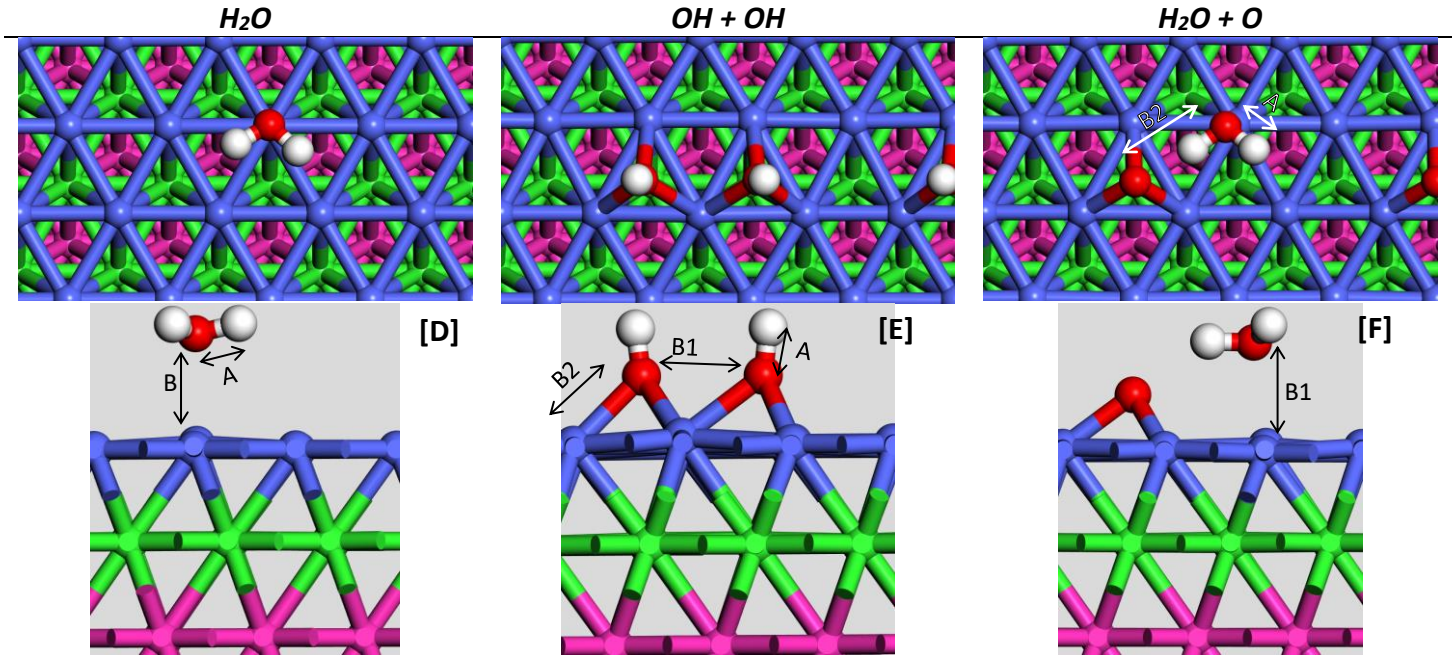

$E_{ads+zpe}$ (eV)	-0.097	$E_{ads+zpe}$ (eV)	-0.11	$E_{ads+zpe}$ (eV)	-0.18
d_{O-H} (A) (Å)	0.978	d_{O-H} (A) (Å)	0.973	d_{O-H} (A) (Å)	0.987
$d_{adsorbate}$ (B) (Å)	2.387	$d_{adsorbate}$ (B1) (Å)	2.865	$d_{adsorbate}$ (B1) (Å)	2.280
Bond angle (°)	104.8	$d_{adsorbate}$ (B2) (Å)	1.985	$d_{adsorbate}$ (B2) (Å)	2.869
				Bond angle (H_2O) (°)	105.8

Figure 5-1: Lowest energy configuration of oxygen removal reactants and products on p(3x3) Co(111) slab. Atoms represented by H, O, Mn, Co in first/forth/fifth layer Co in second and Co in third layer.

The lowest energy configuration of atomic oxygen adsorbed on the bare surface was identified at an hcp position with a total energy of -288 eV. The hydroxyl species prefers an hcp position on Co(111), and in presence of a hydrogen atom adsorbed at a fcc position. The binding energy of the OH + H species on the Co(111) was evaluated at -0.51 eV and is comparable to the results by Govender et al. [68] where a binding energy of -0.47 eV was obtained for the configuration whereby OH and H are in the hcp and fcc positions respectively.

Upon the direct hydrogenation of the hydroxyl species, the resulting water molecule prefers a floating configuration parallel to the metal surface as shown in Figure 5-1[D] whereby the oxygen atom is directly atop a cobalt atom with the bonded hydrogen atoms above fcc sites. Factoring the reference state energy, the adsorption energy of the water molecule was evaluated at -0.097 eV in line with the adsorption energy of -0.09 eV reported by Liu [121] for the same adsorption site. On the other hand, Govender et al. [68] evaluated a significantly lower binding energy level of -0.31 eV for a water molecule floating atop a cobalt atom (The results from this study and that by [121] could be an indication that upon formation, the water molecule rapidly desorbs and thus, resulting in the higher reported energy. Furthermore, the final geometries obtained by Govender et al. [68] were generated on a p(2x2) surface whereby there is a possibility of higher degree of attractive lateral interactions between the adsorbates for this system). Hence, resulting in the lower calculated binding energy.

Prior to the disproportionation reaction of hydroxyl molecules, the most stable configuration of two hydroxyl molecules on the surface must be identified. Having two hydroxy molecules with the oxygen atoms in adjacent hcp positions and the bonded hydrogen tilting away from each other over bridge sites as shown in Figure 5-1[E]; resulted in the lowest energy geometry with an adsorption energy of -0.11 eV. While Govender et al. [68] reports a higher binding energy of -0.15 eV, the lowest energy positions was given by the oxygen atoms on adjacent hcp sites but with the hydrogen atom facing the oxygen atom instead.

The lowest energy position for the disproportionation products can be defined as an oxygen atom adsorbed at an hcp site along with a water molecule floating atop a cobalt atom with the bonded hydrogen atoms at fcc and bridge sites respectively, Figure 5-1[F]. This result in an adsorption energy of -0.18 eV which is significantly higher than the binding energy of -0.63 eV given by Govender et al. [68] for the same final geometries. In this case, the lower energies reported by the latter can be attributed to the used of the smaller p(2x2) slab whereby the adjacent adsorbed oxygen atoms on the surface induce a higher degree of attractive lateral interactions on the hydrogen atoms in the water molecules when considering repeat units on the lattice.

5.3. Oxygen removal species on MnO_x-promoted Co(111)

For the MnO_x promoted oxygen removal process, a slab pre-covered with oxygen at its most stable position with either OMn or O_2Mn co-adsorbed was considered as reference state, Figure 5-2[A] and Figure 5-3[A]. In both cases, oxygen prefers a hcp site neighbouring the ligands. The co-adsorption energies of the different species were defined as per Equation 5-1, whereby the stoichiometric coefficients under Table 5-1 and the total energies of the hydrogen and water in the gas phase under Table 3-2 were still considered. As per all energy calculations, ZPE corrections based on the vibrational modes of the adsorbates and the gaseous molecules were included in the reported adsorption energies. For the promoted reference systems, an oxygen atom was adsorbed at an hcp site far from the ligand while ensuring minimal lateral interactions of the adsorbates in adjacent repeat unit cells. The total energies for the reference system were evaluated at -303 and -310 eV for the OMn and O_2Mn promoted systems respectively.

To obtain a valid configuration for the precursors for the disproportionation reaction on the promoter system, hydroxyl molecules were adsorbed in proximity to hydroxyl-based ligand intermediate as shown in Figure 5-2 and Figure 5-3. In contrast to the unpromoted surface where the disproportionation reactants (OH + OH) preferred hcp sites, we note a hydroxyl molecule over an atop site bonded to the ligand and the other over a fcc site for both OMn and O_2Mn systems. For the OMn promoted system, the disproportionation reactants were defined as OMn(OH) + OH whereby the adsorption energy was evaluated at -0.88 eV with the reference system as basis. The disproportionation reactants on the O_2Mn promoted system were instead defined as $O_2Mn(OH)$ + OH and the resulting adsorption energy was evaluated at -0.22 eV. In both cases, the adsorption energy of the disproportionation reactants is larger than that in the unpromoted case where it was evaluated at -0.11 eV and therefore, suggesting that the presence of manganese may have a stabilising effect via increased bonding.

For the disproportionation products systems, OMn + H_2O + O and O_2Mn + H_2O + O, we note that the H_2O molecules preferred an atop site in proximity of the ligands. The oxygen formed, adsorbed preferentially at a fcc site adjacent to H_2Or. This adsorption geometry contrasts the results on the clean slab, where the oxygen formed preferred to adsorb at a hcp site further from the water molecule floating atop a cobalt atom. For the OMn and O_2Mn promoted systems, the adsorption energies were evaluated at -0.85 and -0.39 eV respectively which are still lower than the binding energy of -0.18 eV in the unpromoted case. In addition to manganese having a stabilising effect on the reaction products, it can be speculated that manganese might also slow down the desorption of water from the surface in comparison to a bare cobalt surface. This is because in addition to the attractive forces between the hydrogen atom in the water molecule and the oxygen adsorbed on the catalysts surface, manganese in the MnO_x-based promoter may also induce some attractive forces.

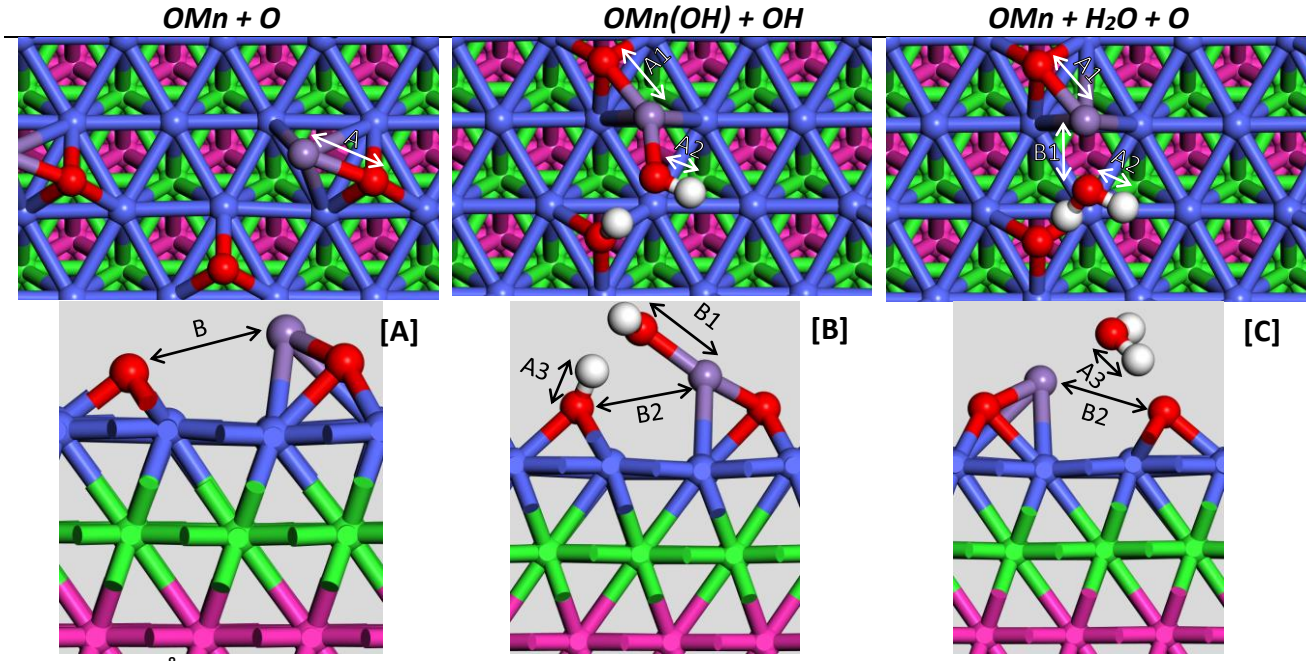

$d_{O\text{-}Mn}$ (A) (Å)	1.938	$E_{ads+zpe}$ (eV)	-0.88	$E_{ads+zpe}$ (eV)	-0.85
$d_{adsorbate}$ (B) (Å)	3.569	$d_{O\text{-}Mn}$ (A1) (Å)	1.934	$d_{O\text{-}Mn}$ (A1) (Å)	1.910
		$d_{O\text{-}H}$ (A2) (Å)	0.973	$d_{O\text{-}H}$ (A2) (Å)	0.976
		$d_{O\text{-}H}$ (A3) (Å)	1.008	$d_{O\text{-}H}$ (A3) (Å)	1.038
		$d_{adsorbate}$ (B1) (Å)	1.883	$d_{adsorbate}$ (B1) (Å)	2.081
		$d_{adsorbate}$ (B2) (Å)	3.310	$d_{adsorbate}$ (B2) (Å)	3.304
				Bond angle (H_2O) (°)	105.3

Figure 5-2: Lowest energy configuration of oxygen removal reactants and products on a p(3x3) OMn promoted Co(111) slab. Atoms represented by H, O, Mn, Co in first/forth/fifth layer, Co in second and Co in third layer.

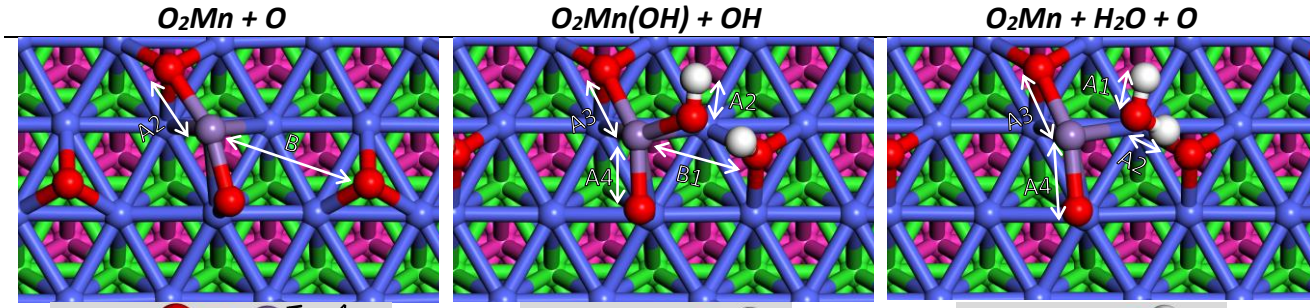

$d_{O\text{-}Mn}$ (A1) (Å)	1.838
$d_{O\text{-}Mn}$ (A2) (Å)	1.962
$d_{adsorbate}$ (B) (Å)	4.280

$E_{ads+zpe}$ (eV)	-0.22
$d_{O\text{-}H}$ (A1) (Å)	1.013
$d_{O\text{-}H}$ (A2) (Å)	0.976
$d_{O\text{-}Mn}$ (A3) (Å)	1.981
$d_{O\text{-}Mn}$ (A4) (Å)	1.812
$d_{adsorbate}$ (B1) (Å)	3.101

$E_{ads+zpe}$ (eV)	-0.39
$d_{O\text{-}H}$ (A1) (Å)	0.976
$d_{O\text{-}H}$ (A2) (Å)	1.002
$d_{O\text{-}Mn}$ (A3) (Å)	1.995
$d_{O\text{-}Mn}$ (A4) (Å)	1.866
$d_{adsorbate}$ (B1) (Å)	2.205
$d_{adsorbate}$ (B2) (Å)	3.145
Bond angle (H_2O) (°)	105.5

Figure 5-3: Lowest energy configuration of oxygen removal reactants and products on a p(3x3) O_2Mn promoted Co(111) slab. Atoms represented by H , O , Mn , Co in first/forth/fifth layer , Co in second and Co in third layer

6. Effect of Mn on CO dissociation

6.1. Introduction

It was shown that the presence of MnO_x ligands on the Co(111) surface has an impact on the adsorption energies of CO dissociation reactants on the catalyst surface (see section 4.3). Furthermore, for the direct CO dissociation, the ligands have been shown to induce changes in the C-O bond length in the adsorbate. Consequently, these changes may have an influence on the activation barriers for the CO dissociation step and bring about a change in the overall rate of CO dissociation. Here we will report possible mechanisms for the changes in adsorption energy and the explanation behind some of the geometric changes such as bond length. Theoretical studies about CO adsorption and activation is mainly carried under low coverage conditions ranging from 1/9 ML to 1/4 ML [81] as repulsive lateral interactions between adsorbed CO molecules can be considered to be negligible at this low coverage. Hence, in this case the direct relationship between the change in activation barriers and the rate of reaction at 1/9 ML will be quantified.

6.2. Charge density and charge analysis

Charge density plots can provide useful visual cues in understanding the electronic effect of the promoter on the adsorption of species present during the Fischer-Tropsch synthesis on Co(111). Hence, the charge densities around the different systems whereby CO/HCO is either far or in proximity of the ligand and their redistributions were calculated using VASP whereby the xyz position of the ions were fixed. For each case, the charge density of the full system(the substrate and the adsorbed system) were calculated to generate charge density plots given by Equation 6-1. VESTA (Visualization for Electronic and Structural Analysis) [122] was used to visualise the charge density difference plots of the co-adsorbed system and thus an overall picture of the charge redistribution upon adsorption of CO/HCO on promoted Co(111) was obtained.

$$\rho_{diff}(x,y,z) = \rho_{CO/HCO+ligand+slab} - \rho_{slab} - \rho_{CO/HCO+ligand} \qquad \textbf{Equation 6-1}$$

From Figure 6-1[A]/[D], the O_xMn ligands induce pocket of electron accumulation in the vicinity of the central metal atom on the cobalt surface. The latter would prove to be high stability co-adsorption sites supported by the lowest co-adsorption energy described in section 3.4. With the adsorbate in proximity to the ligands shown in Figure 6-1[B]/[C], a high-density electron region extending from the central metal atom in the ligand to the carbon atom of the adsorbate can be observed. This phenomenon may explain the enhanced adsorption strength in the case of OMn. This should also be valid for the co-adsorption of O_2Mn and CO, but here a zone with a lower electron density is observed between the oxygen atom in O_2Mn to the carbon atom in the adsorbate, CO. Hence, offsetting the enhancement in adsorption strength. Interestingly, in both cases when the adsorbate is close to the ligand, the manganese atom draws part of the electron density from the oxygen atom of the adsorbate. It induces a region with more electron depletion. CSeeequently, we can extend this explanation to the bond weakening effect reported in the co-adsorbed systems(see section 4.3.1). For the HCO co-adsorbed systems, similar trends can be observed whereby in proximity of the MnO_x there is an extension of the electron density from the Mn centre to the carbon in HCO. It is hard to visually gauge the effect of the promoter on the C-O bond in HCO since in all cases, unpromoted and promoted and a zone with strong electron depletion is present around the C-O bond. Thus, suggesting that the latter is already weak.

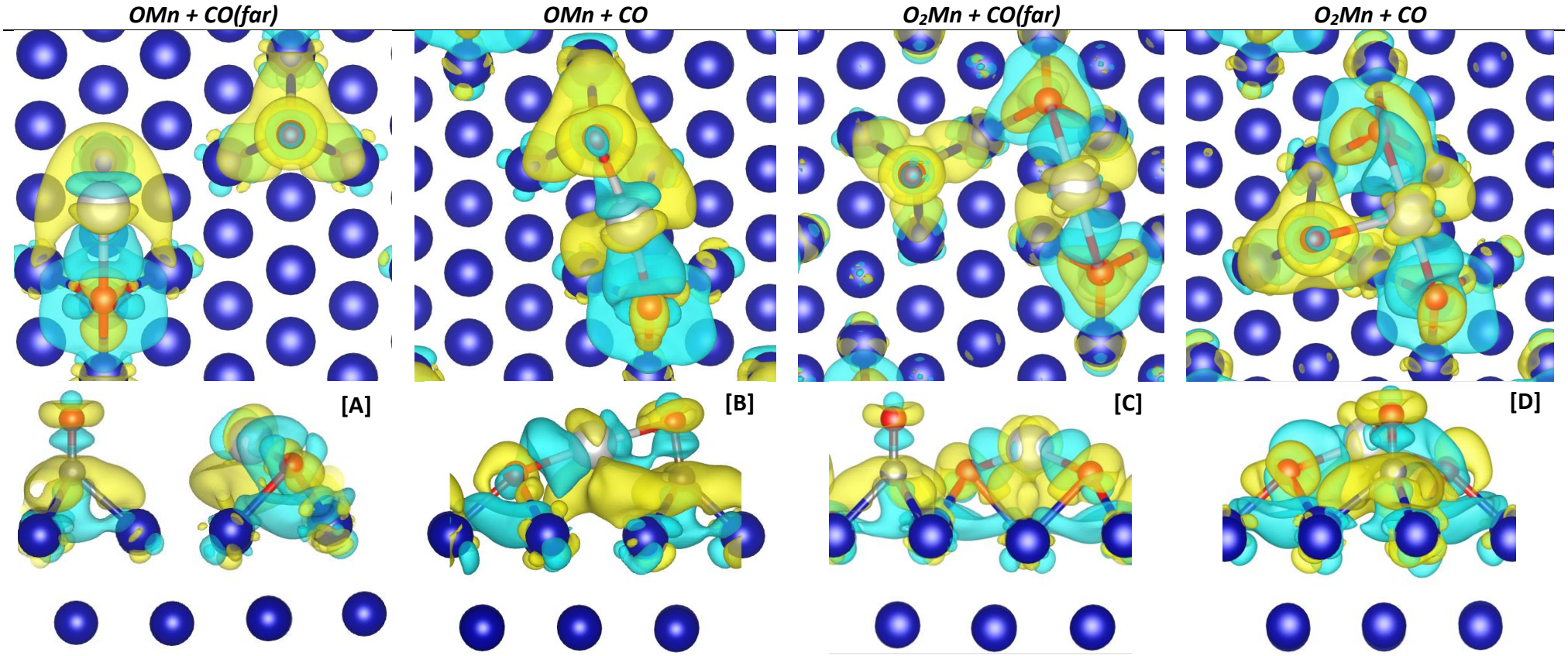

Figure 6-1: Charge density difference plots of CO co-adsorbed with O_xMn systems. Isosurface value=0.005 e/Å^3. Yellow region represents charge gain and blue region represent charge depletion. Atoms represented by C, O, Mn and Co.

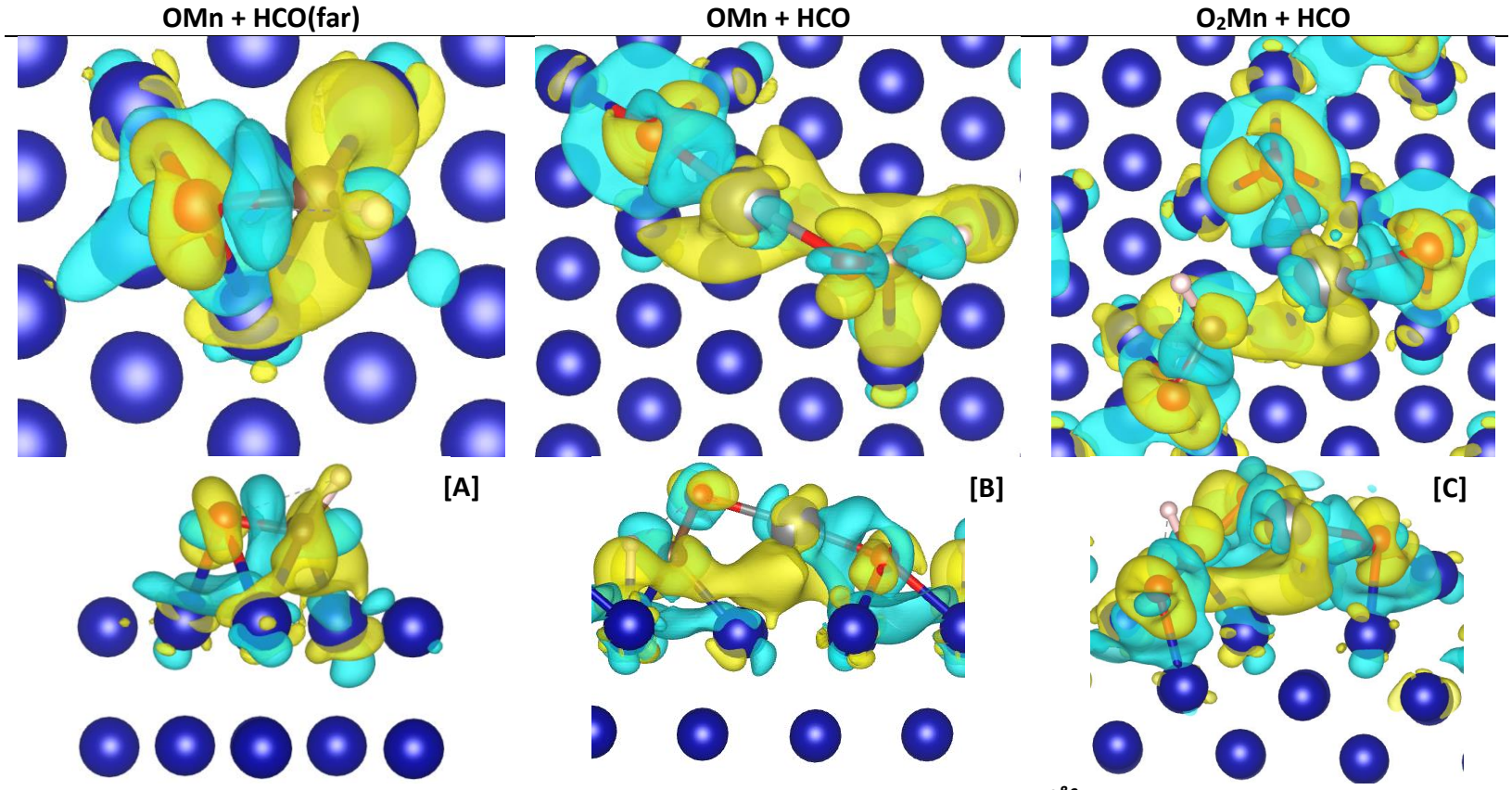

Figure 6-2: Charge density difference plots of HCO co-adsorbed with O_xMn systems. Isosurface value=0.005 e/Å^3. Yellow region represents charge gain and blue region represent charge depletion. Atoms represented by C, H, O, Mn and Co.

To quantify the charge redistribution in the above promoted systems, the charge analysis methodology defined under section 3.3.4 was applied and Table 6-1 generated. While the charge analysis should be useful for understanding the flow of electrons between the ligand centre and the adsorbate, it will also help in understanding the Lewis acid-base interaction between the MnO_x promoter and CO as introduced by Johnson et al. [14]. Based on the result of the NAC analysis in Table 6-1, there is a more significant NAC change for Mn_{lig} in the case of OMn than O_2Mn indicating that there is a higher degree of electron loss or donation in the presence of OMn on Co(111) than in the presence of O_2Mn on Co(111). Thus, based on a Lewis acid-base relationship, the manganese ion in the OMn ligand could act as a weaker Lewis acid than the manganese ion in O_2Mn. The change in the net atomic charge (NAC) on carbon in CO between CO far removed from the ligand and CO in close proximity of the ligand remains unchanged upon changing the ligand from OMn to O_2Mn, 0.053 versus 0.053. This suggests that the ligands have little influence on electron transfer with regards to C in the adsorbate. Thus, it can be suggested that minimal Lewis acid-base interactions are presence between the Mn ions of the promoter and the C atom of the adsorbate. The somewhat larger change in the net atomic charge (NAC) on oxygen in CO in the OMn promoted system in contrast to the O_2Mn promoted system, -0.03 against -0.024 (NAC difference), correlates to a higher degree of electron gain. Hence, this could indicate that oxygen acts as a stronger Lewis base in the OMn promoted system.

Table 6-1: NAC (q_A) on Mn, C and O in CO in far from and close to the MnO_x ligand. Increase in NAC implies a loss of electrons and vice versa

	OMn		**O_2Mn**	
	CO far	**CO close**	**CO far**	**CO close**
Mn_{lig}	0.63	0.71	0.80	0.83
C_{ads}	0.066	-0.013	0.077	0.024
O_{ads}	-0.22	-0.25	-0.21	-0.23

When HCO is adsorbed, Table 6-2, the oxygen in the adsorbate acts as a stronger Lewis base in the presence of OMn compared to O_2Mn. Comparing the NAC on carbon in HCO, we can note significant changes electron exchange in the presence of O_2Mn in comparison to both the unpromoted slab and OMn promotion. Since the NAC on Mn in both OMn and O_2Mn remain unchanged, we can deduce that the metal centre rather induced the redistribution of electron within the adsorbate itself rather than being directly involved.

Table 6-2: NAC (q_A) of Mn, C and O for HCO far and close to the MnO_x ligand. Increase in NAC implies a loss of electrons and vice versa.

	OMn		**O_2Mn**
	HCO far	**HCO close**	**HCO close**
Mn_{lig}		0.72	0.72
C_{ads}	-0.026	-0.0048	-0.21
O_{ads}	-0.16	-0.31	-0.15

To quantify the effect of the MnO_x promoters on the adsorption of CO/HCO on the catalyst surface, chemical bond descriptors such a bond length and bond order can be typically applied. While the bond length between atom A and B (d_{AB}) can be summarised as the average distance between the nuclei of the atoms, the bond order between atom A and B ($B_{A,B}$) correlates to the quantity of electrons 'dressed' exchanged between them [123]. Here we report the DDEC6 bond order [124] evaluated using CHARGEMOL, of C and O in the CO/HCO adsorbate in the presence of the MnO_x based promoters. For comparison, a decrease in bond order correlates to a decrease in bond strength and therefore, an increase in bond length and vice versa.

The bond order for C-O in adsorbed CO on a clean slab is approximately 2 since the CO adsorbate has been positioned far from the ligand (see Table 6-3) and thus, in agreement with the bond order reported in literature [118]. The proximity of CO to the promoter results in a decrease in the C_{ads}-O_{ads} bond order from 2.0 to 1.7 and 2.0 to 1.8 in the case of OMn and O_2Mn respectively. Therefore, suggesting the stretching of the C_{ads}-O_{ads} bond. Furthermore, it can be observed that the bond weakening effect is more significant for the OMn promoted slab, shown by lowest calculated bond order. Comparing the C_{ads}-Co_{surf} bond order, the presence of the MnO_x ligands also affects the binding strength of the adsorbate to the catalyst surface as shown by the increase in magnitude from 1.9 to 2.1 and 1.9 to 1.9 in the case of OMn and O_2Mn respectively. While the change is negligible in the O_2Mn promoted system, it can be suggested that OMn offers a more significant enhancement of the binding strength of CO to the Co(111) surface. From the Mn_{lig}-C_{ads} and Mn_{lig}-O_{ads} bond orders, it can be noted that there is a higher degree of electron exchange between Mn and O than Mn and C. Hence, we can deduce that the metal centre of the ligand induces Lewis acid-based interactions with the oxygen atom in the adsorbate thus, supporting the argument by Johnson et al. [14]. Furthermore, based on the impact of the promoter on the binding strength of adsorbate on the surface and the weakening of intermolecular bond in the adsorbate, we can also expect a change in the activation barriers for the CO dissociation reaction.

Table 6-3: Bond order between atoms (B_{A-B}) for CO far and close to the MnO_x ligands

	OMn		**O_2Mn**	
A-B	**CO far**	**CO close**	**CO far**	**CO close**
Mn_{lig}-C_{ads}	0.0075	0.17	0.0044	0.15
Mn_{lig}-O_{ads}	0.011	0.39	0.025	0.29
C_{ads}-O_{ads}	2.0	1.7	2.0	1.8
C_{ads}-Co_{surf}	1.9	2.1	1.9	1.9

The presence of the MnO_x ligand induce different effects on the bond orders within the HCO adsorbate. OMn seem to strengthen the adsorption of HCO on the Co(111) surface and stabilised the C-O bond given by the increase in C_{ads}-O_{ads} and C_{ads}-Co_{surf} bond orders. O_2Mn on the other does not have a significant influence on the strength of the C-O bond, rather a small weakening effect, but instead worsens the stability of the HCO on the Co(111) surface suggested by the decrease from in the bond order of C_{ads}-Co_{surf} 1.5 to 1.2.

Table 6-4: Bond order between atoms (B_{A-B}) for HCO far and close to the MnO_x ligands

	OMn		**O_2Mn**
A-B	**HCO far**	**HCO close**	**HCO close**
Mn_{lig}-C_{ads}		0.12	0.44
Mn_{lig}-O_{ads}		0.6	0.0015
C_{ads}-O_{ads}	1.4	1.5	1.3
C_{ads}-Co_{surf}	1.5	1.7	1.2

6.3. Activation barrier

6.3.1. Direct CO dissociation

Following the molecular adsorption of CO on the cobalt surface, CO can undergo dissociation via the direct pathway to form carbon and oxygen which in turn can take part chain growth reactions. Here we report the reaction path chosen and the energies for each step for the dissociation reaction at a CO coverage of 1/9 ML, as shown under Figure 6-3. As a base case, the activation energy for the bond scission step via the transition state Figure 6-4[A], was evaluated at 2.59 eV on the unpromoted Co(111) surface (in line with literature values of 2.43 eV [11] and 2.55 eV [41])

When Mn is present on the Co(111) surface as OMn and O_2Mn, the barrier for the forward reaction via transition states Figure 6-4[B] and Figure 6-4[C], is reduced to 2.55 and 2.37 eV respectively. Similarly, the Co/Mn/Co(111) and Mn/Co(111) models by Pedersen et al. [11] experienced reduction in the dissociation barriers to 2.27 eV and 1.13 eV respectively. On the other hand, the opposite effect was recorded by Gençoğlu [41] where the CO dissociation barrier jumped to 3.25 eV in the presence of MnO. For the reverse reaction, the barrier was evaluated at 0.98 eV on the bare metal surface which is comparable to the reverse barrier of 0.816 eV reported by Gençoğlu [41]. The presence of the ligands induces different degrees of change on the reverse barrier: on the OMn promoted surface, the reverse barrier increased to 1.27 eV while on the O_2Mn promoted surface, the reverse barrier was calculated at 0.80 eV. A similar trend was noted by the model by Gençoğlu [41], where the reverse barrier increased in the presence of the promoter, in this case to 2.23 eV.

Given the elevated barriers for the direct CO dissociation step even in the presence of the MnO_x ligands, this pathway can be considered unfavourable as significant energy seems to be required to bend the adsorbed CO molecule and this energy makes up a large part of the reaction barrier. With the activation barriers higher than the adsorption energies in all the cases, we can suggest that CO would rather desorb than dissociate.

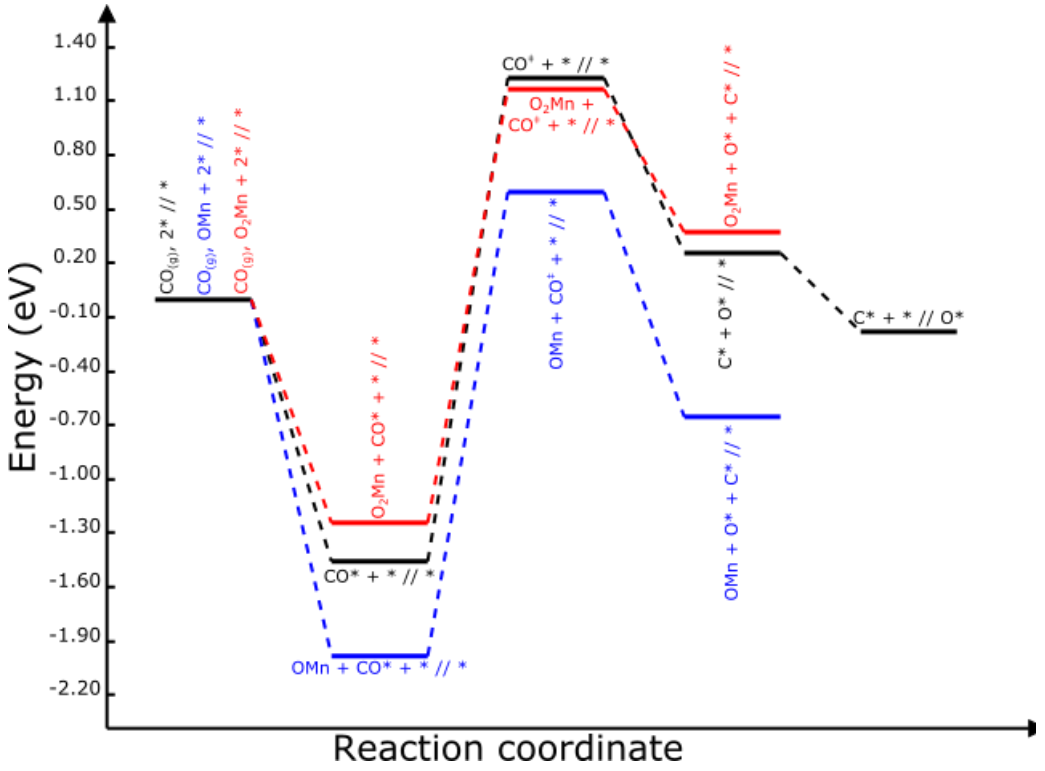

Figure 6-3: Potential energy surface diagram (PES) for direct CO dissociation at 500 K on different Co(111) surfaces unpromoted/promoted at coverage 1/9 ML. Black line=clean Co(111); Blue line= OMn promoted Co(111); Red line= O_2Mn promoted Co(111). Energies corrected for a temperature of 500 K and total pressure of 1 bar

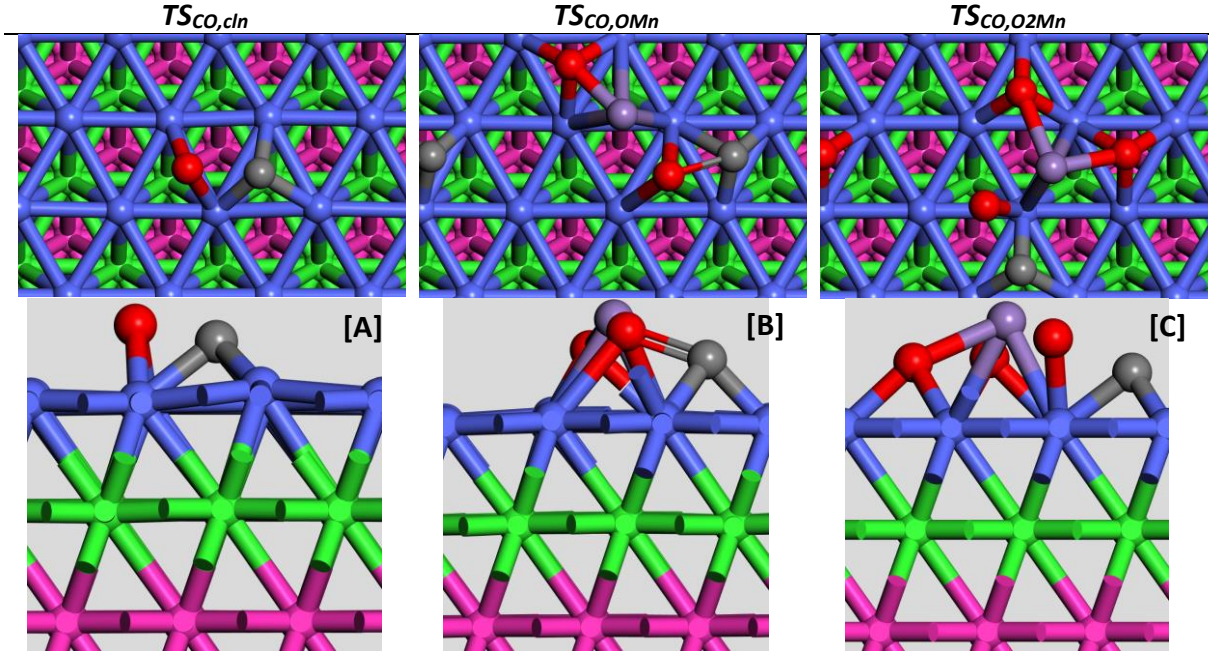

Figure 6-4: Transition states (TS) for the direct CO dissociation on unpromoted and promoted on p(3x3) Co(111) at a coverage of 1/9 ML. Atoms represented by C, O, Mn, Co in first/forth/fifth layer, Co in second and Co in third layer.

6.3.2. H-assisted CO dissociation

For the hydrogen-assisted pathway, the adsorbed CO must first be hydrogenated into HCO, CO + H ↔ HCO, which can either undergo bond scission to form CH + O or further hydrogenation to H_xCO [125]. These longer hydrogenated chains can then undergo bond scission to form CH_x + O. For this study, only the dissociation of HCO to CH + O on the different Co(111) surfaces was considered for comparison to the direct CO dissociation step and a potential surface energy diagram as shown in Figure 6-5 was generated. As reference, the activation energy via the transition state Figure 6-6[A] for the dissociated step was evaluated at 0.18 eV on a bare Co(111) surface(0.70 eV reported by Gençoğlu [41]). The presence of Mn as OMn and O_2Mn, increased the forward reaction barrier via transition states, Figure 6-6[B] and Figure 6-6[C] to 1.41 and 1.70 eV respectively (similar trend to MnO model by Gençoğlu [41] where increase in barrier to 1.15 eV was recorded) . The same observation can be made for the reverse reaction whereby the presence of the ligands increased the reverse barrier from 0.80 eV to 1.67 and 2.07 eV respectively (similar trend observed by Gençoğlu [41] where reverse barrier increased from 0.87 eV to 1.86 eV in the presence of MnO promoter). Based on these results, it can be suggested that the dissociation of CO might be more favourable via the H-assisted pathway on bare surfaces such as Co(111) given significantly lower activation barrier of the dissociation step. This could be attributed to lack of the bending step in the dissociation of HCO compared to an adsorbed CO.

Although, OMn may stabilise HCO (larger adsorption energy), it will not facilitate the dissociation of the C-O bond. On the other hand, O_2Mn neither stabilise the adsorption of HCO nor enhances the dissociation of the C-O bond and thus, HCO in the vicinity of the O_2Mn complex would rather dissociate into CO and H and desorb as CO (or diffuse away from O_2Mn and dissociate at a further site). Although the presence of MnOx ligands did not offer desirable improvements on the dissociation reaction, the promotional effects cannot be fully dismissed as alternative H-assisted pathways for CO dissociation are possible. The study by Gençoğlu [41] also displayed similar trends in the activated barrier for the dissociation step but instead suggested that the presence of Mn as MnO (their model) may offer a reduction in the barrier for the formation of HCO or H_xCO based precursors.

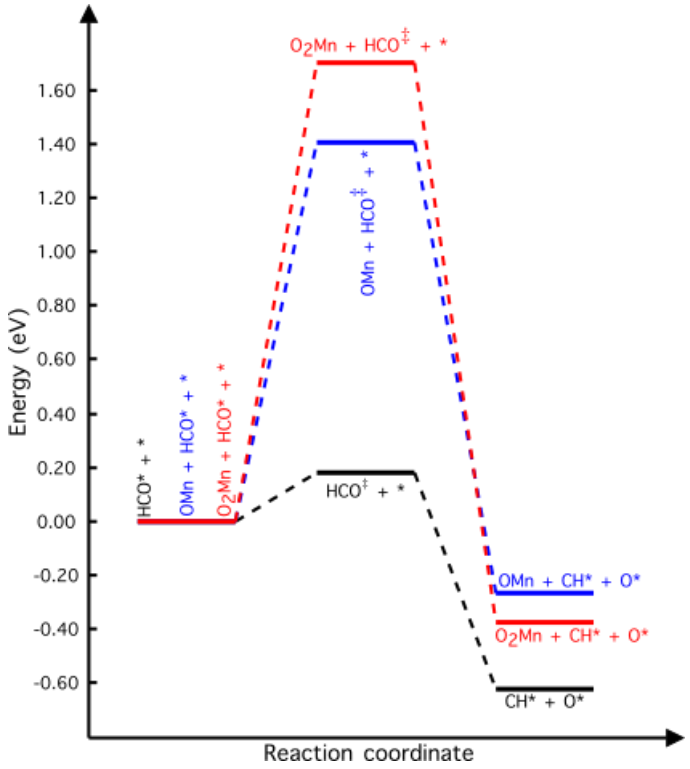

Figure 6-5: Potential energy surface diagram (PES) for hydrogen assisted CO dissociation at 500 K on different Co(111) surfaces unpromoted/promoted at coverage 1/9 ML. Black line=clean Co(111); Blue line= OMn promoted Co(111); Red line= O_2Mn promoted Co(111). Energies corrected for a temperature of 500 K and total pressure of 1 bar

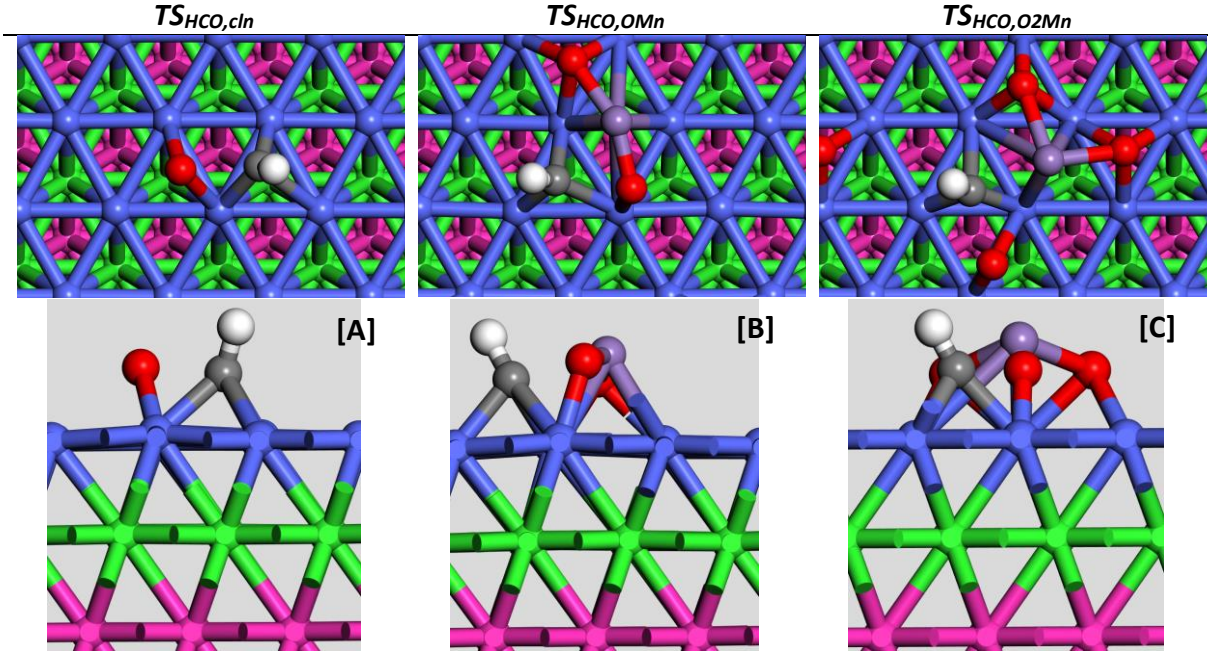

Figure 6-6: Transition states (TS) for the hydrogen assisted CO dissociation on unpromoted and promoted p(3x3) Co(111) at a coverage of 1/9 ML. Atoms represented by C, H, O, Mn, Co in first/forth/fifth layer, Co in second and Co in third layer.

6.4. Rate of CO dissociation

6.4.1. Direct CO dissociation

As reported in section 6.3.1, the presence of MnO_x offers a small reduction in the forward barrier for direct CO dissociation at a coverage of 1/9 ML by 0.04 eV and 0.23 eV in the case of OMn and O_2Mn respectively in comparison to the bare metal. Here, we will discuss the impact of the change in activation barrier on the rate of direct CO dissociation. A simple kinetic model based on the dissociation step given by CO* ↔ C* + O* was considered and for each system, unpromoted and promoted, the Arrhenius-type rate constants for the forward (k_f) and reverse (k_r) reaction were evaluated using Equation 2-53, which can also be written as:

$$k = Ae^{-\frac{E_a}{RT}} \qquad \textit{Equation 6-2}$$

Hence, the dissociation rate (r_{diss}) as a function of the coverage of the species (θ_i) involved in the reaction was calculated using Equation 6-3, whereby a positive reaction rate indicates that CO dissociation into C and O atoms is more facile than the recombination of C and O atom, and vice versa.

$$r_{diss} = k_f \theta_{CO^*} \theta_* - k_r \theta_{C^*} \theta_{O^*} \qquad \textit{Equation 6-3}$$

The presence of Mn as OMn and O_2Mn, result in an increase in the Arrhenius-type forward rate (k_f), up to approximately 180 times in the presence of O_2Mn as shown in Table 6-5. The reverse Arrhenius-type rate (k_r) was instead reduced to 1.59 s^{-1} from 1.48E+03 s^{-1} in the presence of OMn and O_2Mn rather boosted the reverse rate to 7.93E+04 s^{-1}. Based on the negative overall reaction rate (r_{diss}), the recombination of carbon and oxygen atoms into CO seems to be more facile on both unpromoted and promoted Co(111) surfaces at low CO coverages of 1/9 ML. It can be also inferred that OMn facilitates CO dissociation given by the significant increase in the overall reaction rate. On the other hand, the presence of O_2Mn offers a higher degree of C and O recombination than both the clean and the OMn promoted slab and factoring the lower CO co-adsorption energy (see section 4.3.1), it can be confirmed that CO desorption will be more favourable than dissociation.

Table 6-5: Rate constants and overall reaction rate for direct CO dissociation at 500 K. θ_{CO}=0.11, θ_{OMn}=0.22 and θ_{O2Mn}=0.33

	Co(111)	**Co(111)+OMn**	**Co(111)+O_2Mn**
k_f (s^{-1})	7.48E-14	1.91E-13	1.37E-11
k_r (s^{-1})	1.48E+03	1.59	7.93E+04
r_{diss}	-14.2	-0.011	-435

6.4.2. H-assisted CO dissociation

For the H-assisted CO dissociation, a simple kinetic model based on the dissociation step given by HCO* ↔ CH* + O* was considered and for each system, unpromoted and promoted. The rate constants for the forward (k_f) and reverse (k_r) reaction were evaluated using Equation 6-2. The reaction barrier for the forward and reverse reaction in the dissociation of HCO increases due to the presence of OMn and O_2Mn on Co(111) in comparison to the bare Co(111) slab (see section 6.3.2)

Table 6-6: Rate constants and overall reaction rate for H-assisted CO dissociation at 500 K. θ_{HCO}=0.11, θ_{OMn}=0.22 and θ_{O2Mn}=0.33

	Co(111)	**Co(111)+OMn**	**Co(111)+O_2Mn**
k_f (s^{-1})	1.44E+11	6.87E-02	6.86E-05
k_r (s^{-1})	8.22E+04	1.63E-04	1.25E-08
r_{diss}	1.42E+10	0.0051	5.92E-06

As shown in Table 6-6, the presence of Mn as OMn and O_2Mn resulted in a reduction in both the forward and backward Arrhenius-type rate constants owing to the increase in the forward and reverse barriers. Using the calculated rate constants and the coverage values, the overall reaction rates (r_{diss}) on both unpromoted and promoted surfaces were evaluated using Equation 6-3. From the positive r_{diss} values, it can be suggested that dissociation via the H-assisted pathway is more favourable than the direct route on bare Co(111) at low coverages. Similar to section 6.3.2, the presence of MnO_x resulted in worse performance than bare Co(111), here shown by the decrease in r_{diss} values. Thereby suggesting that CH* and O* might be recombine to HCO* which will subsequently decompose to CO* and H*. The promotional effects of Mn cannot be completely dismissed for H-assisted CO dissociation as alternative pathways exist for the dissociation step and also, the formation of the HCO* intermediate itself might influence the kinematics.

7. Effect of Mn on oxygen removal

7.1. Introduction

Given the complexity of oxygen removal on the active cobalt surface, changes in adsorption strength of Fischer-Tropsch species as shown in chapter 5, are not sufficient to obtain a full picture of the impact of manganese-based promoters. Surface oxygen produced upon CO dissociation needs to be removed as it can poison the Fischer-Tropsch catalyst and thus, limit Fischer-Tropsch activity. Disregarding the possibility of functionalising the growing hydrocarbon chain with the surface oxygen (to form alcohol or aldehydes), the latter has been assumed to be fast rejected via water formation [12]. Water formation is a highly activated process [68], and in the presence of the a catalyst, chemisorbed hydrogen and surface oxygen can react to form water [126]. Here, we will first identify the key reactions steps involved in oxygen removal based on the Fischer-Tropsch species adsorbed on the unpromoted and promoted surfaces. Then, the effect of the presence of manganese ligands on the energetics of the oxygen removal process will be investigated and thereby, the rate of oxygen removal can be gauged.

7.2. Activation barrier

The reaction pathway for oxygen removal on both the unpromoted and promoted cobalt surface as shown in Figure 7-2 was generated using the reference states given under Figure 7-1. While the pathways consist of various steps which include adsorption/desorption, diffusion and reactions of different components, key surface reactions for the removal of oxygen were also identified. For the unpromoted pathway the hydrogenation of O* to OH*, the hydrogenation of OH* to H_2O* and the disproportionation of two OH* to H_2O* and O* were chosen. Although the direct hydrogenation of hydroxyl species to water has an elevated barrier in the range of 1.10 – 1.32 eV [68], [121], [127], [128], the reaction was still deemed viable at low OH* concentrations and at 500K. The disproportionation reaction with it much smaller barrier on Co(111))[68], plays a significant role at high OH* concentrations. Thus, water formation can be considered as a blend of the direct hydrogenation and disproportionation of hydroxyl species. For the promoted pathway, in addition to the hydrogenation of the strongly bound oxygen to hydroxyl, the hydrogenation of the O_2Mn promoter to OMn(OH) and the disproportionation involving OMn(OH) and OH* to OMn(H_2O) and O* were identified as key surface reactions. The direct hydrogenation of two OMn(OH) promoter intermediates to OMn(H_2O) and O_2Mn was not included due to geometry limitations on a p(3x3) slab and the likelihood of lateral interactions between neighbouring intermediates.

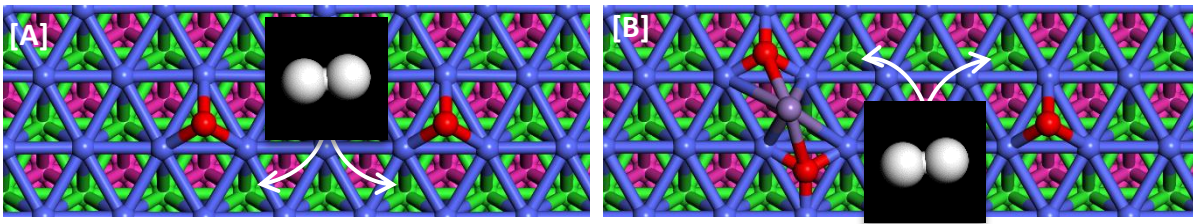

Figure 7-1: Reference states for the removal of oxygen on unpromoted and promoted p(3x3) Co(111). [A] Unpromoted: $H_{2(g)}$, O* + * // O + *. [B] Promoted: $H_{2(g)}$, O_2Mn + * // O + * . Atoms represented by H, O, Mn, Co in first/forth/fifth layer Co in second and Co in third layer .

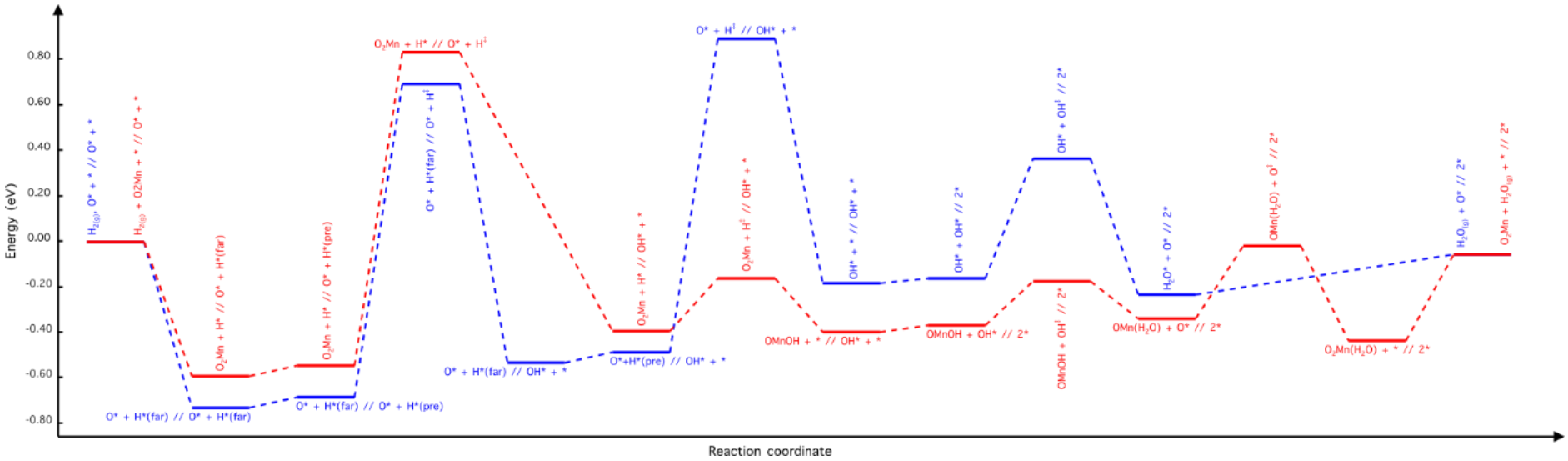

Figure 7-2: Potential energy surface (PES) diagram for the removal of oxygen as water on p(3x3) Co(111). Blue line=removal pathway on an unpromoted slab; red line=oxygen removal pathway on a O_2Mn promoted slab. Energies corrected for a temperature of 500 K and total pressure of 1 bar. See appendix D.1 for transition states.

At 500 K, the forward barrier for the for the hydrogenation of oxygen was evaluated at 1.38 eV on a clean Co(111) which is comparable to those reported in literature (Govender et al. [68] reports a forward barrier of 1.16 eV on Co(111) and Gong et al. [126] reports a forward barrier of 1.72 eV on Co(0001)). In the presence of manganese as O_2Mn, an adsorbed hydrogen combines with one of the oxygen atoms in the ligand to form an intermediate hydroxyl-based ligand, OMn(OH). In contrast to the direct hydrogenation of chemisorbed oxygen, the hydrogenation of O_2Mn was found to be more facile with a forward barrier of 0.23 eV. The reverse barrier for hydrogenation of O_2Mn was evaluated at 1.06 eV while that of the direct hydrogenation of oxygen was reported at a higher magnitude of 1.16 eV. The presence of O_2Mn on the surface can be said to induce favourable O_2Mn-H interactions. Hence, the minimum pathway for the reactions avoids the atop sites. While the hydrogenation of the O_2Mn promoter was found to be more facile, the promoted pathway still requires the formation of OH* as it as a precursor for the disproportionation reaction.

The barriers for the disproportionation reactions for the chemisorbed hydroxyl species on the bare Co(111) surface are given by 0.53 eV for the forward reaction and 0.61 eV for the reverse reaction. In the presence of manganese as the OMn(OH) intermediate, the disproportionation of the hydroxyl species occurs via the reaction $OMn(OH) + OH^* \leftrightarrow OMn(H_2O) + O^*$ and the reaction barriers were evaluated at 0.19 eV and 0.11 eV for the forward and backward steps respectively. As with the hydrogenation of O_2Mn, OMn(OH) induces favourable OMn(OH)-H interactions such that the formation of $OMn(H_2O)$ becomes more facile.

Since CO dissociation may proceed via the H-assisted pathway, Raub et al. [12] and Govender et al. [68] suggest that the surface may be pre-covered by OH* rather than O*. On that note, the O_2Mn ligand may combine with the hydroxyl species to form $O_2Mn(OH)$. This intermediate ligand can then undergo the disproportionation with other hydroxyl species to form $O_2Mn(H_2O)$ and O* via $O_2Mn(OH) + OH^* \leftrightarrow O_2Mn(H_2O) + O^*$. Via this pathway, Figure 7-3, the barriers for the disproportionation reaction were evaluated at 0.014 eV and 0.19 eV for the forward and reverse barrier respectively. This could be attributed to the proximity of the adsorbate and the ligand intermediate and hence, less energy is required for bond breaking. Although this reaction may suggest the possibility of faster initial removal of hydroxyl species, the surface oxygen produced from the disproportionation reaction will still have to be hydrogenated to hydroxyl for removal. Hence, the pathway described by Figure 7-2 will further be required.

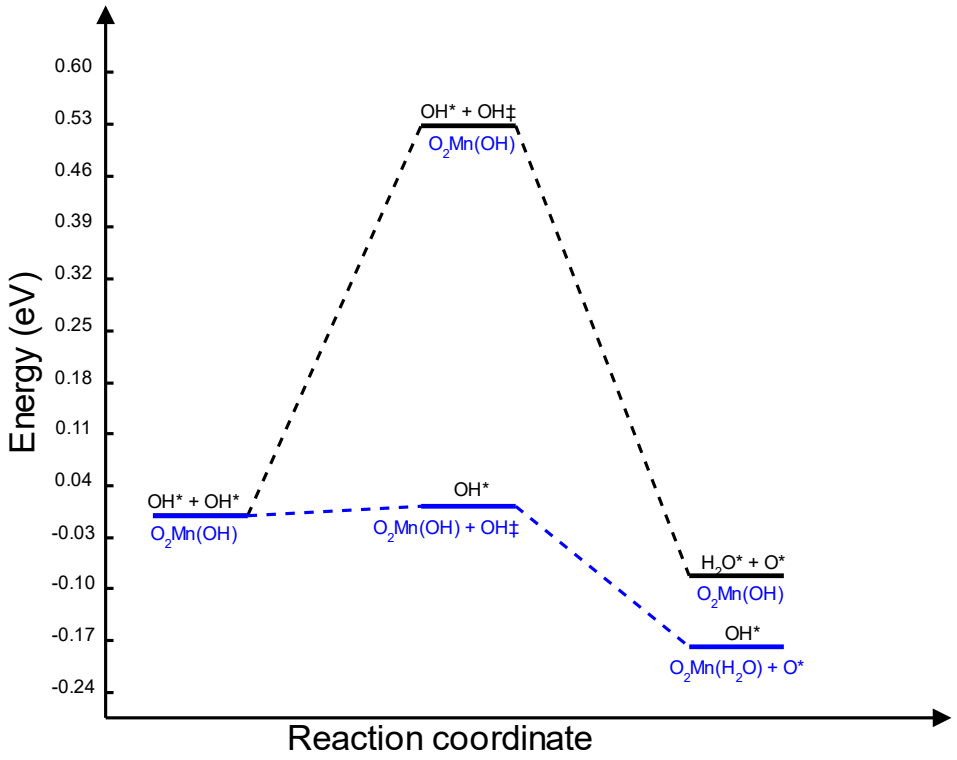

Figure 7-3: Potential energy surface (PES) diagram for the disproportionation step on p(3x3) Co(111) slab pre-covered with OH*. Black line represents oxygen removal pathway on an unpromoted slab. Blue line represents oxygen removal pathway on a O_2Mn promoted slab. Energies corrected for a temperature of 500 K and total pressure of 1 bar. See appendix D.1 for transition states.

7.3. Rate of oxygen removal

7.3.1. Microkinetic model

The changes in the activation barriers for the reactions described in section 7.2, are only part of the equation to draw conclusions on the effect of the manganese oxide promoter on the removal of oxygen as water. Hence, a microkinetic model was devised to correlate the change in the barriers to the rate of oxygen removal on the Co(111) surface. Relevant Fischer-Tropsch synthesis conditions were considered for the microkinetic analysis; a temperature of 500 K and partial pressures of H_2 and H_2O of 10 and 2.5 bar respectively. The starting coverage for the unpromoted Co(111) surface were set to 22% O*, 33% H* and the difference assigned to the vacant sites, typical for initial FTS conditions [68]. For the promoted model, the O_2Mn system was considered as it is the dominant ligand under Fischer-Tropsch operating temperature and partial pressures of H_2 and H_2O, section 3.3.3. The same starting coverages were used for O* and H* but an additional 33% was allocated for the O_2Mn ligand.

Given the complexity of oxygen removal as water on the cobalt surface, the microkinetic analysis was performed based on the elementary step reactions given by Equation 7-1 to Equation 7-5 for the unpromoted case. For the promoted catalyst surface, 7 additional elementary step reactions were also considered, Equation 7-6 to Equation 7-13, where X* represents an X-occupied catalytic site and * denotes a vacant site. It should be noted that the simplified rate model can only provide part of the picture for the analysis and hence, a material/species balance, in terms of fractional coverage, for each of the reaction steps will be required.

Adsorption/desorption reactions:

$$H_2 + 2^* \leftrightarrow 2H^* \qquad \textbf{Equation 7-1}$$

$$H_2O + {}^* \leftrightarrow H_2O^* \qquad \textbf{Equation 7-2}$$

Surface reactions:

$$O^* + H^* \leftrightarrow OH^* + {}^* \qquad \textbf{Equation 7-3}$$

$$OH^* + OH^* \leftrightarrow H_2O^* + O^* \qquad \textbf{Equation 7-4}$$

$$OH^* + H^* \leftrightarrow H_2O^* + {}^* \qquad \textbf{Equation 7-5}$$

Additional adsorption/desorption reactions (assuming H_2O bonds directly to promoter):

$$OMn + H_2O \leftrightarrow OMn(H_2O) \qquad \textbf{Equation 7-6}$$

$$O_2Mn + H_2O \leftrightarrow O_2Mn(H_2O) \qquad \textbf{Equation 7-7}$$

Surface Reactions:

$$O_2Mn + H^* \leftrightarrow OMn(OH) + {}^* \quad \textbf{Equation 7-8}$$

$$OMn(OH) + OH^* \leftrightarrow OMn(H_2O) + O^* \quad \textbf{Equation 7-9}$$

$$OMn(H_2O) + O^* \leftrightarrow O_2Mn(H_2O) + {}^* \quad \textbf{Equation 7-10}$$

$$OMn + O^* \leftrightarrow O_2Mn + {}^* \quad \textbf{Equation 7-11}$$

$$O_2Mn + OH^* \leftrightarrow O_2Mn(OH) + {}^* \quad \textbf{Equation 7-12}$$

$$O_2Mn(OH) + OH^* \leftrightarrow O_2Mn(H_2O) + O^* \quad \textbf{Equation 7-13}$$

The rate equations corresponding to each elementary step reaction as function of the factional coverage of the different species (θ_i) and the vacant sites (θ_*) can then be expressed as per Equation 7-16 to Equation 7-18 and Equation 7-21 to Equation 7-26. Since adsorption and desorption of gaseous species is included in the oxygen removal process, a partial pressure component was also included in the rate equations corresponding to these steps, Equation 7-14 to Equation 7-15 and Equation 7-19 to Equation 7-20.

Adsorption/desorption reactions:

$$r_1 = k_{ads,\,H_2}.\left(p_{H_2}.\theta_*^2 - \frac{\theta_H^2}{K_{ads,H_2}}\right) \quad \textbf{Equation 7-14}$$

$$r_2 = k_{ads,\,H_2O}.\left(p_{H_2O}.\theta_* - \frac{\theta_{H_2O}}{K_{ads,H_2O}}\right) \quad \textbf{Equation 7-15}$$

Surface reactions:

$$r_3 = k_3\left(\theta_O.\theta_H - \frac{\theta_{OH}.\theta_*}{K_3}\right) \quad \textbf{Equation 7-16}$$

$$r_4 = k_4\left(\theta_{OH}.\theta_{OH} - \frac{\theta_{H_2O}.\theta_O}{K_4}\right) \quad \textbf{Equation 7-17}$$

$$r_5 = k_5\left(\theta_{OH}.\theta_H - \frac{\theta_{H_2O}.\theta_*}{K_5}\right) \quad \textbf{Equation 7-18}$$

Additional adsorption/desorption reactions (assuming H_2O bonds directly to promoter):

$$r_6 = k_{ads,\,H_2O+OMn}\left(p_{H_2O}.\theta_{OMn} - \frac{\theta_{H_2O}}{K_{ads,H_2O+OMn}}\right) \quad \textbf{Equation 7-19}$$

$$r_7 = k_{ads,\,H_2O+O_2Mn}\left(p_{H_2O}.\theta_{O_2Mn} - \frac{\theta_{H_2O}}{K_{ads,H_2O+O_2Mn}}\right) \quad \textbf{Equation 7-20}$$

Surface Reactions:

$$r_8 = k_8\left(\theta_{O_2Mn}.\theta_H - \frac{\theta_{OMn(OH)}.\theta_*}{K_8}\right) \quad \textbf{Equation 7-21}$$

$$r_9 = k_9\left(\theta_{OMn(OH)}.\theta_{OH} - \frac{\theta_{OMn(H_2O)}.\theta_O}{K_9}\right) \quad \textbf{Equation 7-22}$$

$$r_{10} = k_{10}\left(\theta_{OMn(H_2O)}.\theta_O - \frac{\theta_{O_2Mn(H_2O)}.\theta_*}{K_{10}}\right) \quad \textbf{Equation 7-23}$$

$$r_{11} = k_{11}\left(\theta_{OMn}.\theta_O - \frac{\theta_{O_2Mn}.\theta_*}{K_{11}}\right) \quad \textbf{Equation 7-24}$$

$$r_{12} = k_{12}\left(\theta_{O_2Mn}.\theta_{OH} - \frac{\theta_{O_2Mn(OH)}.\theta_*}{K_{12}}\right) \quad \textbf{Equation 7-25}$$

$$r_{13} = 3\left(\theta_{O_2Mn(OH)}.\theta_{OH} - \frac{\theta_{O_2Mn(H_2O)}.\theta_O}{K_{13}}\right) \quad \textbf{Equation 7-26}$$

Similar to the kinetics for CO dissociation, the surface reactions for the oxygen removal can modelled on the basis of the transition state theory. Hence, considering the vibrational partition function of the adsorbates ($q_{vib,i}$), the kinetic rates(r_i) and corresponding equilibrium constants(K_i) can be expressed as follows [68]:

$$k_i = \frac{k_B T}{h}\frac{q_{vib,TS,i}^{3N-1}}{q_{vib,IS,i}^{3N}} e^{\frac{-E_{act,i}}{k_B T}} \quad \textbf{Equation 7-27}$$

$$K_i = \frac{q_{vib,FS,i}^{3N}}{q_{vib,IS,i}^{3N}} e^{\frac{-\Delta E_{rxn,i}}{k_B T}} \quad \textbf{Equation 7-28}$$

It should be noted that the vibrational partition function has been considered for all 3N degrees of freedom, where N is the number of free atoms in the species of the initial (IS) and final (FS) states. On the other hand, 3N-1 degrees of freedom were considered for the transition state (TS).

The adsorption/desorption of the molecular species, H_2 and H_2O, were modelled as the Hertz-Knudsen(HK) type reactions as they can describe the transition from the mobile 3D gas phase to the restricted 2D surface and vice versa [129]. For this study, the adsorption of H_2 and H_2O were assumed to occur spontaneously, thus having zero-energy barrier. The reaction rate and equilibrium constants were hence evaluated as per Equation 7-29 to Equation 7-31 [68] respectively. The parameters for the Hertz-Knudsen equation include the area of the average surface site (A_{site}), the mass of the molecule (m_i), the sticking coefficient of the molecule (S_0) and the heat of adsorption (ΔE_{ads}).

$$k_{ads},i = \frac{A_{site}.S_0}{\sqrt{2\pi.m_i.k_B.T}} \qquad \textit{Equation 7-29}$$

$$K_{ads,H_2O} = \frac{q^{(9)}_{vib,H_2O*}}{q^{(3)}_{vib,H2O(g)}q^{(3)}_{trans,H2O(g)}q^{(3)}_{rot,H2O(g)}} e^{\frac{-\Delta E_{ads}}{RT}} \qquad \textit{Equation 7-30}$$

$$K_{ads,H_2} = \frac{\left(q^{(3)}_{vib,H*}\right)^2}{q_{vib,H_2(g)}q^{(3)}_{trans,H2(g)}q^{(2)}_{rot,H2(g)}} e^{\frac{-\Delta E_{ads}}{RT}} \qquad \textit{Equation 7-31}$$

Lastly, to complete the microkinetic model, a material balance expressed as a set of ordinary differential equations (ODEs) was derived based on the stoichiometry of the species for each reaction. Hence, to obtain the changes in fractional coverage of the different species, the set of ODEs was solved using the MKMCXX code for microkinetic models [129]. Final differences method was used to construct the Jacobian and absolute/relative tolerances of 10e-12 was implemented [68]. Also, with this study considering a thin film of Co in contrast to a Co nanoparticle, it was assumed a sticking probability of unity. Maintaining the basis of a low coverage of the adsorbates,the effect of lateral interactions between adsorbates was minimised.

7.3.2. Surface oxygen removal

From the microkinetic model, the time required for the complete removal of oxygen on the unpromoted and promoted slab was evaluated as shown in Table 7-1. Full surface oxygen (as O*) removal is a feworders of magnitude faster on the O_2Mn promoted surface in comparison to bare Co(111) slab, $10^{-1.3}$ vs $10^{2.9}$ seconds. Based on the coverage profiles under Figure 7-4 and Figure 7-5, it can be noted that in addition to the improved oxygen removal time, the promoted slab shortens the time for peak H* coverage and vacant sites availability. The promoted slab also displays both a lower degree of H* saturation and a lower vacant site availability. This could be attributed to the presence of the hydroxyl-based promoter intermediates on the surface which is further reduced to OMn over time. It can also be noted that there is no build-up of OH* and H_2O* on both the unpromoted and promoted surfaces, Figure 7-4[B] and Figure 7-5[B] and thus, indicate that the surface hydroxy formed rapidly reacts to form H_2O* which in turn rapidly desorbs to the gas phase. The presence of the ligand seems to also minimise both the delay in achieving peak hydroxyl coverage but also the magnitude of peak surface hydroxyl coverage. Therefore, enhancing the rate of H_2O* formation, desorption to the gas phase and the rate of vacant site availability. We can also note that the regeneration of the ligand to O_2Mn is limited as shown in Figure 7 5[C] owing to lack of surface oxygen. Instead, the OMn(OH) mops up the residual hydroxyl on the surface to form OMn(H_2O), Figure 7 5[D]. With lack of the subsequent oxidation step to $O_2Mn(H_2O)$, H_2O readily desorbs to the gas phase leaving the ligand in the reduced OMn state Figure 7 5[C].

Table 7-1: Summary of the time taken for the complete removal of chemisorbed oxygen on unpromoted and promoted Co(111) surface under Fischer-Tropsch conditions.

System	**Time for complete O* removal (s)**
Co(111)	$10^{2.9}$
Co(111)-O_2Mn	$10^{-1.3}$

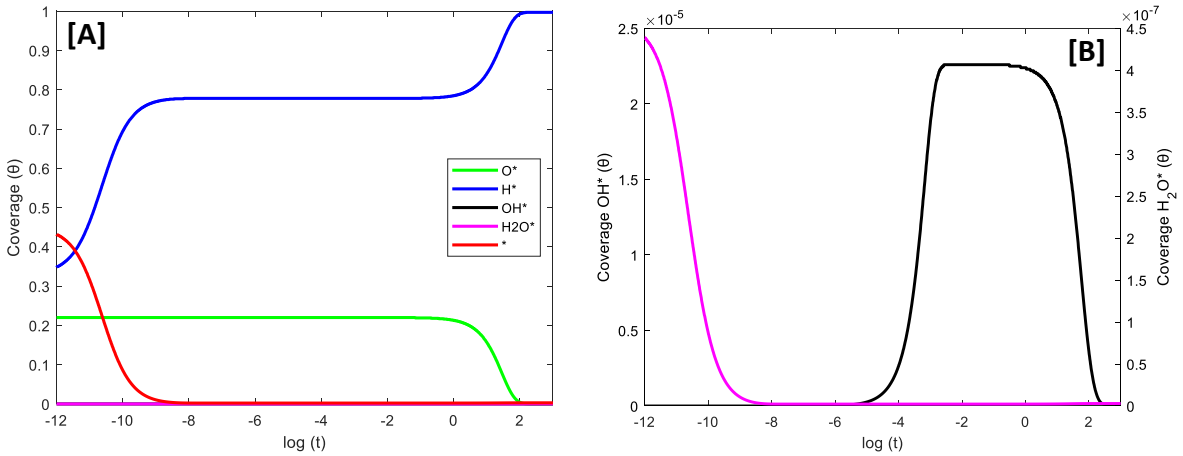

Figure 7-4: Rate of oxygen removal on clean p(3x3) Co(111). Coverage profile at 500K, p_{H2}=10 bar and p_{H2O}=2.5 bar. $\theta_{O^*,ini}$=0.22, $\theta_{H^*,ini}$=0.33 and $\theta_{*,ini}$=0.45- [A] Overall picture of coverage profile for oxygen removal, [B] Coverage profile for the conversion of OH* to H_2O^*

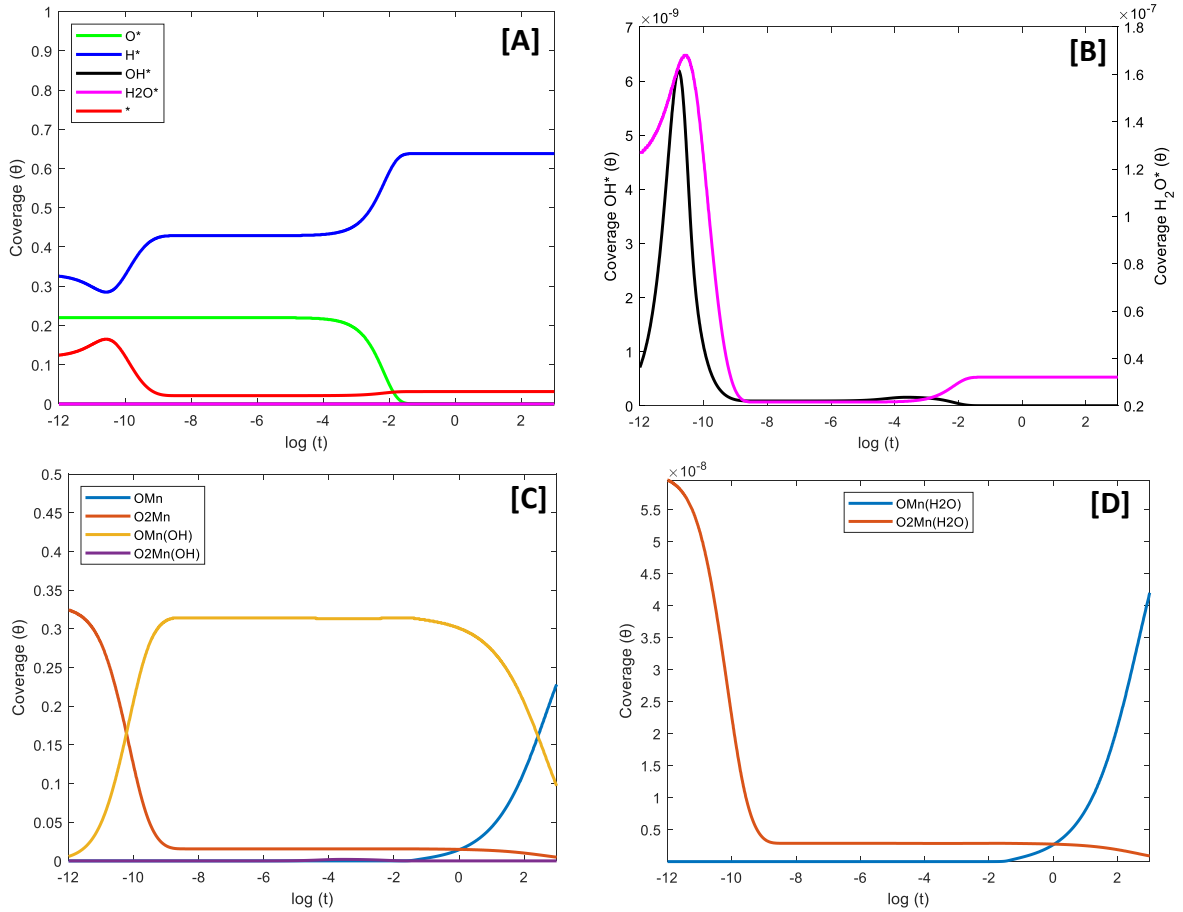

Figure 7-5: Rate of oxygen removal on O_2Mn promoted p(3x3) Co(111). Coverage profile at 500K, p_{H2}=10 bar and p_{H2O}=2.5 bar. $\theta_{O^*,ini}$=0.22, $\theta_{H^*,ini}$=0.33, $\theta_{*,ini}$=0.12 and $\theta_{O2Mn,ini}$=0.33- [A] Overall picture of coverage profile for oxygen removal, [B] Coverage profile for the conversion of OH* to H_2O^*, [C]/[D] Coverage profile of the ligand/ligand intermediates for an oxygen removal cycle.

7.3.3. Sensitivity Analysis

7.3.3.1. Effect of change in rate constant

To understand the correlation of the reaction steps given by under Equation 2-23 to Equation 7-13 to the oxygen removal process, a sensitivity analysis was performed by varying the rate constant for each reaction. The rate constants were varied by changing the forward and backwards activation barriers by factors of 0.1, 0.25, 0.5, 1, 2, 5 and 10 where 1 is the default calculated activation energy. The forward and backward rate constants were varied by the same factor thereby, ensuring the thermodynamic consistency of the model. Hence, the overall equilibrium constant remained unchanged.
From the model, it was found that changing the activation barrier for the gas phase adsorption and desorption of H_2 and H_2O has no effect on the rate of oxygen removal from the surface but rather affect the saturation coverages of H* and the availability of vacant sites.

As suggested by Govender et al. [68], changing the rate constant for the formation of OH* species, Equation 7-3, has significant impact in the rate of removal of surface oxygen. As shown in Figure 7-6, by increasing the rate constant, there is a shift in oxygen coverage as a function of time. Similarly, as the surface coverage of chemisorbed oxygen decreases at a faster rate, saturation of the surface with H* occurs in a shorter lapse. The same can be noted for the availability of the vacant sites on surface, whereby the increase in the rate constants shortens the time for the maximum number of vacant sites to be free. At factors of 0.1 and 0.25, a noticeable amount of OH* is formed as the concentration of surface O* decreases. This observation could be due to the faster OH* formation than consumption by the disproportionation reaction initially. As the maximum OH* concentration is reached, the rate disproportionation overcomes rate of hydroxyl formation and consequently, OH* is removed from the surface over time. At factors above 1, the changes in oxygen removal time, does not change much suggesting, that overcoming the higher barriers is difficult at 500 K.

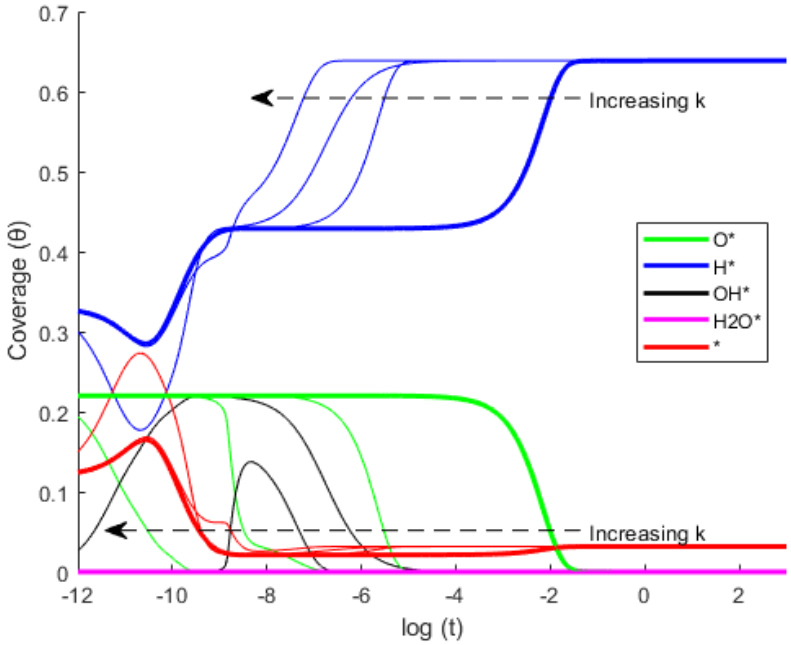

Figure 7-6: Rate of oxygen removal on O_2Mn promoted p(3x3) Co(111). Coverage profile at 500K, p_{H2}=10 bar and p_{H2O}=2.5 bar. $\theta_{O^*,ini}$=0.22, $\theta_{H^*,ini}$=0.33, $\theta_{*,ini}$=0.12 and $\theta_{O2Mn,ini}$=0.33; base profile in bold. Effect of increasing the rate constant k of the reaction O* + H* ↔ OH* + *.

OMn(OH) is a key ligand intermediate in the oxygen removal process as it introduces the pathway for promoted disproportionation reaction as given by Equation 7-9 and thereby is not only related to the removal of water to gas phase but also the regeneration of the O_2Mn ligand. Hence, valuable insights can be obtained by investigating the rate of formation of OMn(OH). From Figure 7-7 [A], increasing the rate constant given by decreasing the activation energy, result in the reduction in the total time required for oxygen removal from the catalyst surface. As with the formation of OH*, the increase in rate also shortens the time required for maximum H* coverage and vacant sites availability. It can be noted that the change in rate constant for OMn(OH) formation has a lesser impact on oxygen removal than OH* formation. This is because OH* is still the key precursor for both promoted and unpromoted disproportionation reactions. Furthermore, at factors less than 1, no additional improvement in oxygen removal time was observed. This is because at very low barriers the reaction is preferentially 'mopping' the surface H* species and therefore limiting the formation of OH* from reaction given by Equation 7-3. With the limited supply of surface hydroxyl species, the disproportionation reaction cannot occur, thus bottlenecking oxygen removal.

Disproportionation of surface hydroxyls to form water can also occur in the presence of $O_2Mn(OH)$, which as mentioned in section 7.2, can be formed from the reaction between the O_2Mn ligand and hydroxyl molecules formed via H-assisted CO dissociation. From Figure 7-7 [B], we note that increasing the rate constant by decreasing the activation barrier factor beyond 5 does not bring any improvement on the oxygen removal time in comparison to the formation of OMn(OH) where effect of increasing the rate constant only settles beyond a factor of 2. Thereby suggesting that at high k values, the formation of additional hydroxyl species via Equation 7-3 is limited and hence, bottlenecking the removal of surface oxygen as water.

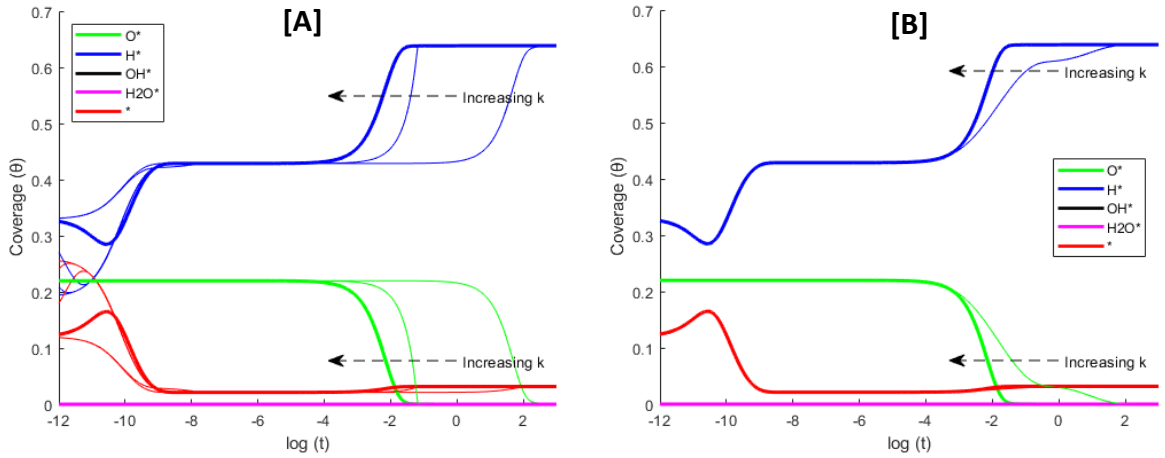

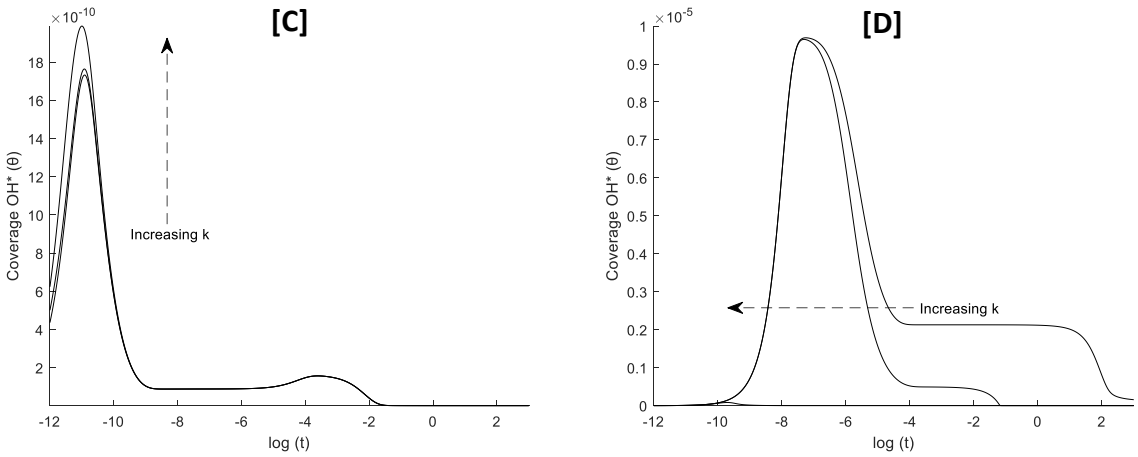

Figure 7-7: Rate of oxygen removal on O_2Mn promoted p(3x3) Co(111). Coverage profiles at 500K, p_{H2}=10 bar and p_{H2O}=2.5 bar. $\theta_{O^*,ini}$=0.22, $\theta_{H^*,ini}$=0.33, $\theta_{*,ini}$=0.34 and $\theta_{O2Mn,ini}$=0.33; base case in bold. [A] Effect of increasing the rate constant k on reaction $O_2Mn + H^* \leftrightarrow OMn(OH) + *$. [B] Effect of increasing the rate constant k of the reaction $O_2Mn + OH^* \leftrightarrow O_2Mn(OH) + *$. [C] Coverage profile for the formation of OH* at factors less than 1. [D] Coverage profile for the formation of OH* at factors above 1.

The rate of the disproportionation reaction, OH* + OH* ↔ H2O* + O*, was also subjected to a sensitivity analysis and a coverage profile as a function of time was generated (see Figure 7-8). By increasing the rate constant i.e decreasing the activation energy from a factor of 10 to 0.1, noticeable improvement in the oxygen removal time was only observed at factors less than 1, Figure 7-8. The easier is the formation of water from the reaction, the faster complete oxygen removal will occur. But it should be noted that although the dependence of oxygen removal as water can be attributed to the disproportionation reaction, the latter reaction is still limited by the hydrogenation of surface oxygen to hydroxyl. For high barrier (at factors above 1) of the disproportionation reaction, it can be suggested that the surface hydroxyls instead take part in the formation of hydroxyl-based ligands intermediates and are instead involved in the promoted disproportionation reaction. Hence, we can suggest that the hydrogenation surface oxygen becomes the rate limiting step and therefore, no further change in oxygen removal time was observed.

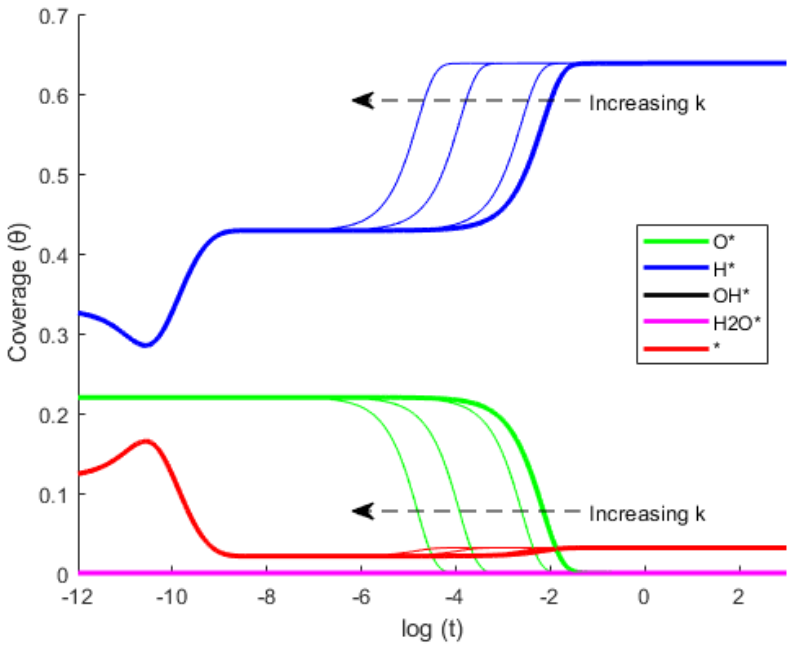

Figure 7-8: Rate of oxygen removal on O_2Mn promoted p(3x3) Co(111). Coverage profile at 500K, p_{H2}=10 bar and p_{H2O}=2.5 bar. $\theta_{O^*,ini}$=0.22, $\theta_{H^*,ini}$=0.33, $\theta_{*,ini}$=0.34 and $\theta_{O2Mn,ini}$=0.33; base case in bold. Effect of increasing the rate constant k of the reaction OH* + OH* ↔ H_2O* + O*.

As part of the sensitivity analysis, it is fair to consider the effect of increasing the rate constant for the disproportionation reaction involving the OMn(OH) intermediate. Changing the activation barrier by a factor less than 1, has insignificant effect on the rate of oxygen removal on the Co(111) surface as shown by the lack of coverage profile on the left of the default profile(in bold) in Figure 7-9 [A]. This observation was expected as the availability of OH* is still limited by the hydrogenation reaction given by Equation 7-3. Similarly, the availability of the OMn(OH) intermediate is also limited by the hydrogenation of O_2Mn to OMn(OH), Equation 7-8.

The disproportionation reaction of $O_2Mn(OH)$ and OH can also provide insights on oxygen removal on Co(111) in the presence of O_2Mn as it introduces another pathway for the formation of water. In contrast to the disproportionation involving OMn(OH), the reaction is more sensitive to changes in activation barriers as shown in Figure 7-9 [B]. A possible explanation would be that post the disproportionation reaction, there is a rapid desorption of H_2O to the gas phase from the ligand complex and therefore regenerating the O_2Mn ligand.

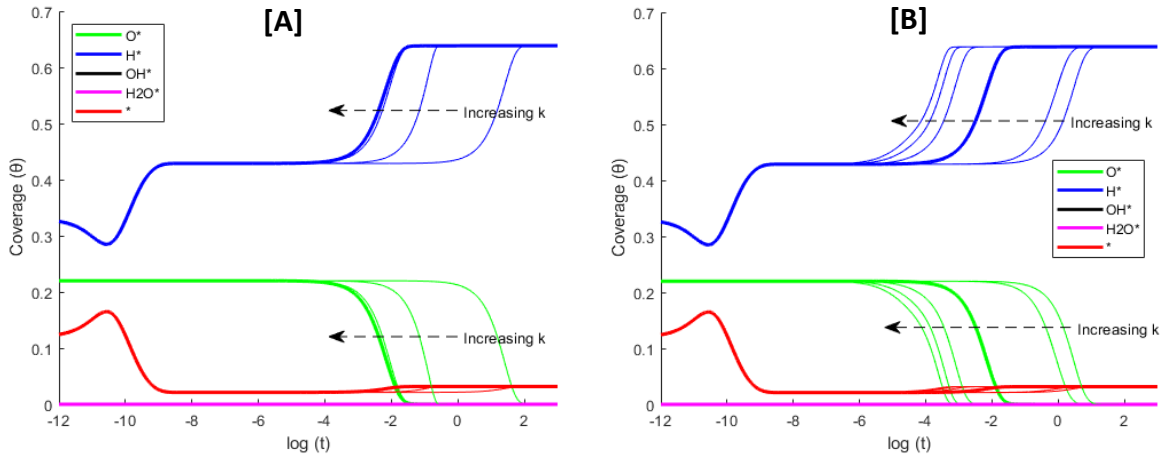

Figure 7-9: Rate of oxygen removal on O_2Mn promoted p(3x3) Co(111). Coverage profile at 500K, p_{H2}=10 bar and p_{H2O}=2.5 bar. $\theta_{O^*,ini}$=0.22, $\theta_{H^*,ini}$=0.33, $\theta_{*,ini}$=0.34 and $\theta_{O2Mn,ini}$=0.33; base case in bold. [A] Effect of increasing the rate constant k of the reaction OMn(OH) + OH* ↔ OMn(H_2O) + O*.). [B] Effect of increasing the rate constant k on reaction $O_2Mn(OH)$ + OH* ↔ $O_2Mn(H_2O)$ + O*.

The regeneration of the O_2Mn ligand from OMn, Equation 7-11, was also considered for a sensitivity analysis as upon desorption of H_2O from the OMn(H_2O) complex, Equation 7-6, OMn ligands will be present on the cobalt surface (see Figure 7-10). Thus, for the sequence of reactions taking place on Co(111) in the presence of O_2Mn to occur leading to surface oxygen removal, O_2Mn will have to be regenerated. Increasing the activation barrier for the re-formation of O_2Mn from OMn by a factor of greater than 2 results in a decrease in the rate of oxygen removal. This may be attributed to the slow formation of the O_2Mn complex involved in the oxygen removal. At a factor of 2 and less, deviation from the standard coverage profile is minimal as the reaction will be limited by the availability of surface O* which is rapidly depleted by the series of reactions on the surface.

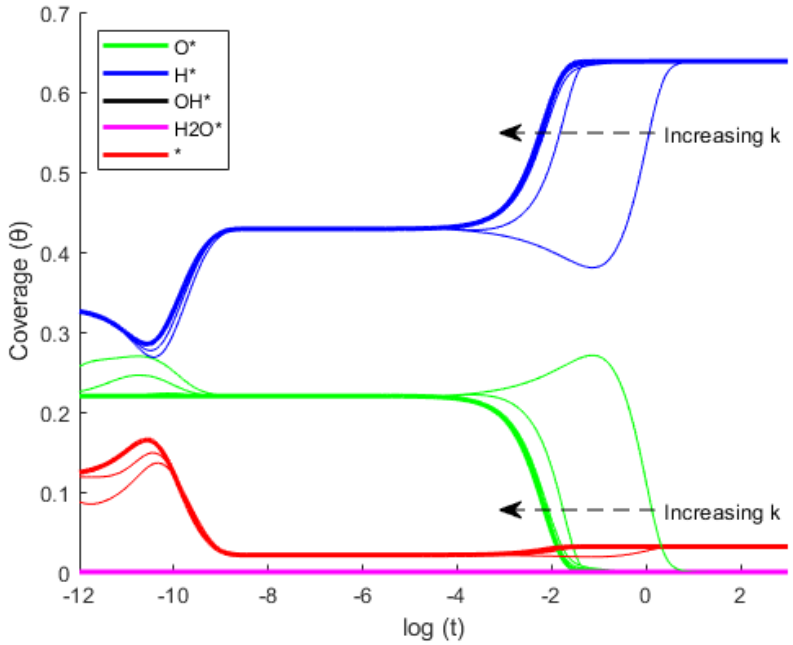

Figure 7-10: Rate of oxygen removal on O_2Mn promoted p(3x3) Co(111). Effect of increasing the rate constant k of the reaction OMn* + O* ↔ O_2Mn* + *. Coverage profile at 500K, p_{H2}=10 bar and p_{H2O}=2.5 bar. $\theta_{O*,ini}$=0.22, $\theta_{H*,ini}$=0.33, $\theta_{*,ini}$=0.34 and $\theta_{O2Mn,ini}$=0.33; base case in bold.

Based on the above, it was concluded that changing the rate constant for the hydrogenation of the chemisorbed oxygen to hydroxyl species has a greater impact on the rate of oxygen removal and can be considered as rate controlling step as supported by [68].

7.3.3.2. Effect of change in starting coverage

CO dissociation over cobalt-based Fischer-Tropsch catalysts may proceed via the OH-assisted pathway and the catalytic surface may be initially covered by hydroxyl species instead of oxygen [12], [68]. Therefore, instead of having a hydrogenation reaction as first step of the removal mechanism, OH* can initially react through the disproportionation reaction to form H_2O* and O*. While H_2O* can rapidly desorb to the gas phase as H_2O, the strongly bound O* will remain on the surface and therefore will have to undergo the same 2-step mechanism as O*[68]. From Figure 7-11, the time for total oxygen removal on the clean surface decreased $10^{2.9}$ to $10^{2.1}$, with OH* as starting reactant. Although the reduction in total time for removal, the difficult hydrogenation step given by Equation 7-3, to remove the O* produced from the disproportionation reaction is still required. It can be also noted that same peak coverage of H* is achieved when OH* is used as starting reactant when compared to both unpromoted and promoted base O* cases. From Figure 7-11, similar profiles for the vacant site coverage as the base O* cases were obtained. Thus, suggesting that the swap of starting reactants has negligible effect on the rate of oxygen removal on Co(111).

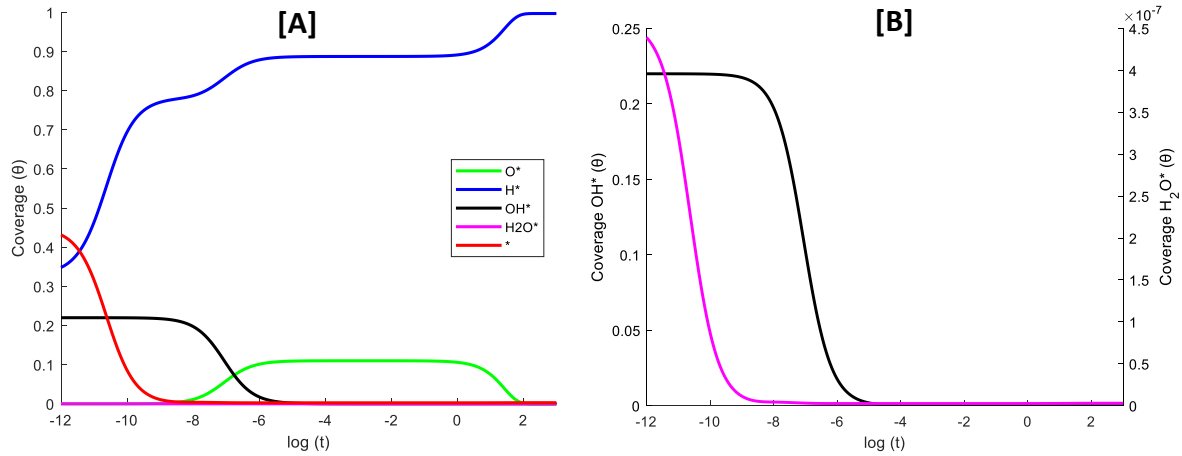

Figure 7-11: Rate of oxygen removal on p(3x3) Co(111). Effect of changing the staring species coverage. Coverage profile at 500K, p_{H2}=10 bar and p_{H2O}=2.5 bar. $\theta_{OH*,ini}$=0.22, $\theta_{H*,ini}$=0.33, $\theta_{*,ini}$=0.34 and $\theta_{O2Mn,ini}$=0.11; base case in bold. [A] Overall picture of coverage profile for oxygen removal, [B] Coverage profile for the conversion of OH* to H_2O*.

For the promoted system, the total time for oxygen removal shows a drastic decrease to $10^{-5.1}$ with OH* as starting reactant as shown in Figure 7-12[A]. With the slab pre-covered with the hydroxyl species, we can note that there is rapid conversion of O_2Mn to OMn(OH) as the reaction does not have to compete with the hydrogenation of surface O* as it was the case previously. Removal of those hydroxyls species are more facile shown by the rapid drop in OH* coverage in Figure 7-12[B] since the disproportionation in the presence of OMn(OH) is more favourable. It should also be noted that surface oxygen produced from the disproportionation reaction is rapidly taken by Equation 7-10 to form $O_2Mn(H_2O)$ as shown by Figure 7-12[D] where H_2O can desorb to regenerate O_2Mn. Hence, the path leading to hydroxyl removal as water can be cycled.

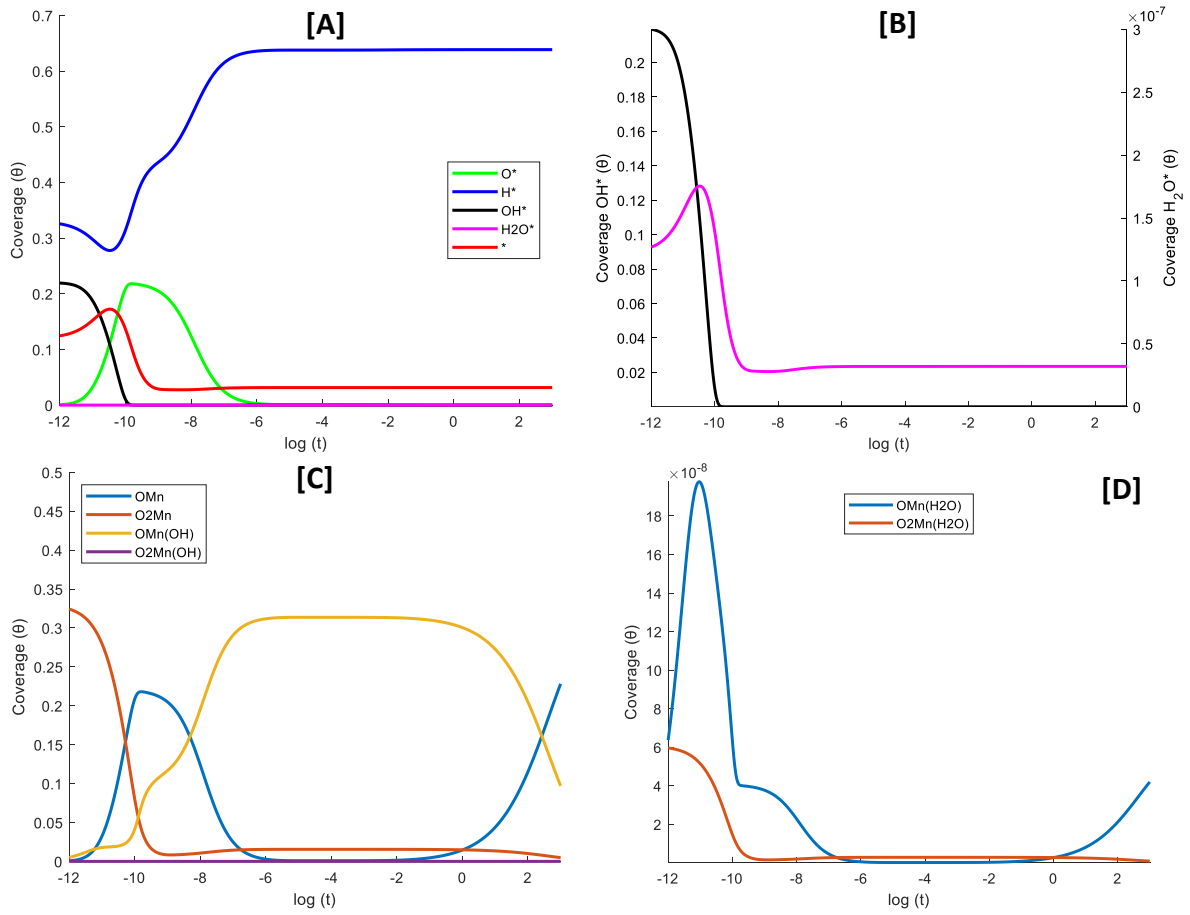

Figure 7-12: Rate of oxygen removal on O_2Mn promoted p(3x3) Co(111). Effect of changing the staring species coverage. Coverage profile at 500K, p_{H2}=10 bar and p_{H2O}=2.5 bar. $\theta_{OH^*,ini}$=0.22, $\theta_{H^*,ini}$=0.33, $\theta_{*,ini}$=0.12 and $\theta_{O2Mn,ini}$=0.33- [A] Overall picture of coverage profile for oxygen removal, [B] Coverage profile for the conversion of OH* to H_2O*, [C]/[D] Coverage profile of the ligand/ligand intermediates for an oxygen removal cycle

7.3.3.3. Effect of change in temperature

Finally, the effect of temperature on the rate of oxygen removal on the promoted surface was considered and a coverage profile shown by Figure 7-13 was plotted. With typical Fischer-Tropsch temperatures ranging from 473-553 K [118], increasing the temperature over the stated range can offer an improvement on oxygen removal time (min $10^{-1.7}$ and max $10^{-1.1}$). Interestingly, increasing the temperature has a more pronounced effect on the coverage profile of H* and the availability of vacant sites. As complete oxygen removal is achieved, higher temperatures favour the desorption of adsorbed atomic hydrogen as hydrogenation of O* and O_2Mn, Equation 7-3 and Equation 7-8, are no longer limiting. Thus, as seen in Figure 7-13, more vacant sites are available at higher temperatures. While operating at higher temperature may not be a feasible commercial option for such small change, the sensitivity analysis of temperature instead can instead be used to understand the behaviour of the promoted catalyst in case of sudden change in operating conditions.

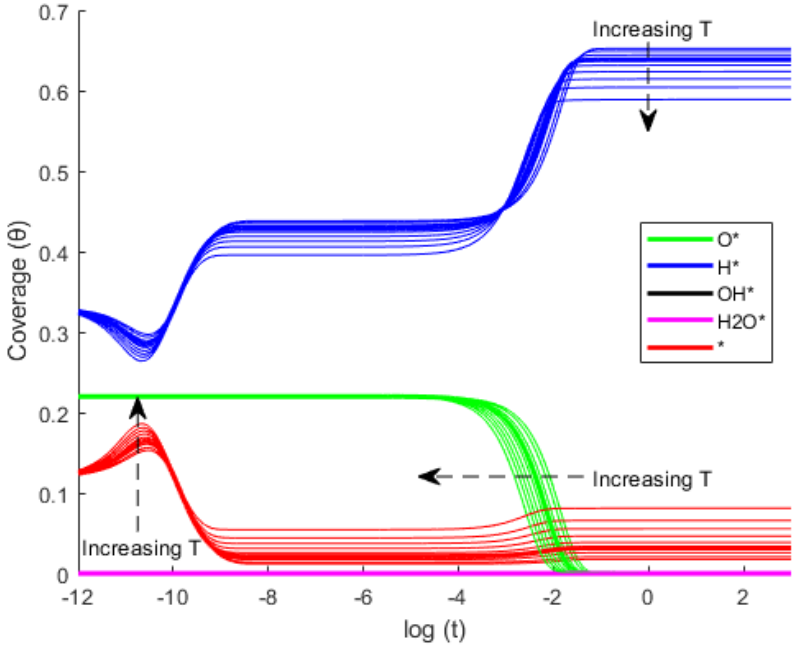

Figure 7-13: Rate of oxygen removal on O_2Mn promoted p(3x3) Co(111). Effect of changing the reaction temperature. Coverage profile for temperature range of 473-553 K, p_{H2}=10 bar and p_{H2O}=2.5 bar. $\Theta_{O^*,ini}$=0.22, $\Theta_{H^*,ini}$=0.33, $\Theta_{*,ini}$=0.34, $\Theta_{O2Mn,ini}$=0.33 and T=500 K; base case in bold.

8. Conclusions

8.1. General conclusions

The aim of the study was to devise suitable theoretical models to understand the effect of MnO_x as a promoter on Fischer-Tropsch reactions. With the adsorption of different Fischer-Tropsch species being the basis of the models, an optimised Co(111) slab with a lattice parameter of 3.551 Å was generated. To ensure that correct adsorption energies are calculated, the slab was geometrically optimised such that five layers of cobalt atoms, with the bottom two layer fixed and a vacuum gap of 12 Å was suitable. Computationally, the revised Perdew-Burke-Ernzerhof (RPBE) functional was considered since its suitability has been backed by theoretical studies involving the cobalt system with adsorbates at low coverage along with a cut-off energy of 400 eV and k-point grid of 9 x 9 x 1.

For the MnO_x models, the configurations given by OMn and O_2Mn were found to be thermodynamically feasible under Fischer-Tropsch conditions on the Co(111) surface. OMn would be the likely ligand at low ratios of H_2O to H_2 and O_2Mn would become the dominant species at high conversions. Co-adsorption in the presence of the dominant MnO_x species revealed useful information on stability of Fischer-Tropsch species. It was found that the presence of OMn on Co(111) further stabilised the adsorption of CO and both the presence of OMn and O_2Mn induces an elongation of the C-O bond in adsorbed CO. OMn also stabilised the dissociation products, co-adsorbed carbon and oxygen on Co(111), whereas the presence of O_2Mn does not seem to affect the dissociation equilibrium significantly. The same trend in the stability of HCO was observed. The presence of OMn improved the adsorption stability of the reactant species and the dissociation products, CH and O on the Co(111) surface. It is worth noting that no significant change in the C-O bond length occurred.

When considering the rate of CO dissociation, the presence of these ligands offers a slight enhancement by lowering the barrier for CO-dissociation from 2.59 eV on Co(111) to 2.55 eV in the presence of OMn and to 2.37 eV in the presence of O_2Mn. Hence, the presence of MnO_x on Co(111) results in a slightly faster direct CO dissociation than on a clean slab. It should however be noted that the direct CO-dissociation on Co(111) is very slow at typical Fischer-Tropsch conditions, even in the presence of MnO_x ligands. Hence, hydrogen-assisted CO dissociation is typically considered on these dense surfaces. In contrast to the direct CO dissociation, the H-assisted pathways proceeds with a significantly smaller activation barrier of 0.18 eV. But, the presence of presence of MnO_x ligands does not seem to facilitate the hydrogen-assisted dissociation via pathway considered and instead resulted in elevated barriers.

The oxygen removal model on Co(111) validated the disproportionation of surface hydroxyl species as the key reaction for the removal of surface oxygen as water. The presence of MnO_x ligands on Co(111) offers new pathways for oxygen removal involving hydroxylated surface manganese complexes, i.e., OMn(OH) and O_2Mn(OH), which can act as reactive intermediates in the oxygen removal. The microkinetic analysis showed that the removal of oxygen in the presence of O_2Mn on Co(111) was $10^{4.2}$ times faster than in the absence of this ligand under Fischer-Tropsch conditions. With the possibility of surface hydroxyls species being instead present on Co(111) following H-assisted CO dissociation, the presence of O_2Mn can drastically improves the surface oxygen removal time in comparison to an unpromoted slab covered with same amount of hydroxyl species. This could be attributed to the rapid conversion of O_2Mn to OMn(OH) as the reaction does not have to compete with the hydrogenation of surface oxygen as it was the case previously.

In summary, it can therefore be concluded that the proposed hypothesis is supported by the findings of this study. Although the presence of the manganese as promoter for cobalt-based catalysts may affect the CO adsorption, it did not affect the dominant indirect hydrogen-assisted CO dissociation pathway. Instead, the promotional effect of manganese maybe be related to the oxygen removal from the Co(111) surface.

With hydrogen-assisted CO dissociation being the dominant pathway on Co(111) and O_2Mn also enhancing the removal of surface hydroxyls via the same pathway as oxygen removal, it introduces the possibility of alternate CO dissociation pathway involving species such alcohols or carboxylic acids. The next possible step would be to devise a kinetic model that considered the different possible pathways of CO dissociation and perform a sensitivity analysis to assess the dominant pathways under various reactor conditions.

References

[1] H. Jahangiri, J. Bennett, P. Mahjoubi, K. Wilson, and S. Gu, “A review of advanced catalyst development for Fischer-Tropsch synthesis of hydrocarbons from biomass derived syn-gas,” *Catalysis Science and Technology*, vol. 4, no. 8. The Royal Society of Chemistry, pp. 2210–2229, 07-Jul-2014.

[2] N. Armaroli and V. Balzani, “The future of energy supply: Challenges and opportunities,” *Angewandte Chemie - International Edition*, vol. 46, no. 1–2. John Wiley & Sons, Ltd, pp. 52–66, 01-Jan-2007.

[3] G. Q. Chen and M. K. Patel, “Plastics derived from biological sources: Present and future: A technical and environmental review,” *Chemical Reviews*, vol. 112, no. 4. American Chemical Society, pp. 2082–2099, 11-Apr-2012.

[4] E. G. Pereira, J. N. Da Silva, J. L. De Oliveira, and C. S. MacHado, “Sustainable energy: A review of gasification technologies,” *Renewable and Sustainable Energy Reviews*, vol. 16, no. 7. Pergamon, pp. 4753–4762, 01-Sep-2012.

[5] U. Arena, “Process and technological aspects of municipal solid waste gasification. A review,” *Waste Manag.*, vol. 32, no. 4, pp. 625–639, Apr. 2012.

[6] A. de Klerk, “Fischer–Tropsch Process,” in *Kirk-Othmer Encyclopedia of Chemical Technology*, American Cancer Society, 2013, pp. 1–20.

[7] F. Morales and B. M. Weckhuysen, “Promotion Effects in Co-based Fischer–Tropsch Catalysis,” 2007, pp. 1–40.

[8] C. L. Tucker and E. van Steen, “Activity and selectivity of a cobalt-based Fischer-Tropsch catalyst operating at high conversion for once-through biomass-to-liquid operation,” *Catal. Today*, vol. 342, no. 15 February 2020, pp. 115–123, Feb. 2020.

[9] C. L. Tucker, “Waste to Fuel : Designing a cobalt based catalyst and process for once-through Fischer-Tropsch synthesis operated at high conversion,” University of Cape Town, 2020.

[10] G. Jacobs, T. K. Das, Y. Zhang, J. Li, G. Racoillet, and B. H. Davis, “Fischer-Tropsch synthesis: Support, loading, and promoter effects on the reducibility of cobalt catalysts,” *Appl. Catal. A Gen.*, vol. 233, no. 1–2, pp. 263–281, Jul. 2002.

[11] E. Ø. Pedersen, I. H. Svenum, and E. A. Blekkan, “Mn promoted Co catalysts for Fischer-Tropsch production of light olefins – An experimental and theoretical study,” *J. Catal.*, vol. 361, pp. 23–32, May 2018.

[12] A. Raub, H. Karroum, M. Athariboroujeny, and N. Kruse, “Chemical Transient Kinetics in Studies of the Fischer–Tropsch Reaction and Beyond,” *Catal. Letters*, vol. 151, no. 3, pp. 613–626, Mar. 2021.

[13] A. Dinse, M. Aigner, M. Ulbrich, G. R. Johnson, and A. T. Bell, “Effects of Mn promotion on the activity and selectivity of Co/SiO2 for Fischer-Tropsch Synthesis,” *J. Catal.*, vol. 288, pp. 104–114, 2012.

[14] G. R. Johnson, S. Werner, and A. T. Bell, “An Investigation into the Effects of Mn Promotion on the Activity and Selectivity of Co/SiO2 for Fischer-Tropsch Synthesis: Evidence for Enhanced CO Adsorption and Dissociation,” *ACS Catal.*, vol. 5, no. 10, pp. 5888–5903, Oct. 2015.

[15] R. Zennaro, M. Ricci, L. Bua, C. Querci, L. Carnelli, and A. D’Arminio Monforte, “Syngas: The Basis of Fischer-Tropsch,” in *Greener Fischer-Tropsch Processes for Fuels and Feedstocks*, Weinheim, Germany: Wiley-VCH Verlag GmbH & Co. KGaA, 2013, pp. 17–51.

[16] A. de Klerk and P. M. Maitlis, “What Can We Do with Fischer-Tropsch Products?,” in *Greener Fischer-Tropsch Processes for Fuels and Feedstocks*, Weinheim, Germany: Wiley-VCH Verlag GmbH & Co. KGaA, 2013, pp. 81–105.

[17] F. Morales and B. M. Weckhuysen, “Promotion Effects in Co-based Fischer-Tropsch Catalysis,” *Catalysis*, vol. 19, pp. 1–40, 2006.

[18] P. M. Maitlis, “What is Fischer-Tropsch?,” in *Greener Fischer-Tropsch Processes for Fuels and Feedstocks*, Weinheim, Germany: Wiley-VCH Verlag GmbH & Co. KGaA, 2013, pp. 1–15.

[19] O. Deutschmann, H. Knözinger, K. Kochloefl, and T. Turek, “Heterogeneous Catalysis and Solid Catalysts,” in *Ullmann’s Encyclopedia of Industrial Chemistry*, Weinheim, Germany: Wiley-VCH Verlag GmbH & Co. KGaA, 2009.

[20] B. Cornils, W. A. Herrmann, C.-H. Wong, and H.-W. Zanthoff, *Catalysis from A to Z*. .

[21] Z. Zsoldos, T. Hoffer, and L. Guczi, “Structure and catalytic activity of alumina-supported Pt-Co bimetallic catalysts. 1. Characterization by X-ray photoelectron spectroscopy,” *J. Phys. Chem.*, vol. 95, no. 2, pp. 798–801, 1991.

[22] L. A. Bruce, M. Hoang, A. E. Hughes, and T. W. Turney, “Ruthenium promotion of fischer-tropsch synthesis over coprecipitated cobalt/ceria catalysts,” *Appl. Catal. A, Gen.*, vol. 100, no. 1, pp. 51–67, Jul. 1993.

[23] G. Jacobs, J. A. Chaney, P. M. Patterson, T. K. Das, and B. H. Davis, “Fischer-Tropsch synthesis: Study of the promotion of Re on the reduction property of Co/Al2O3 catalysts by in situ EXAFS/XANES of Co K and Re LIII edges and XPS,” *Appl. Catal. A Gen.*, vol. 264, no. 2, pp. 203–212, Jun. 2004.

[24] A. Steynberg and M. Dry, *Fischer-Tropsch technology*. Elsevier, 2004.

[25] S. Vada, A. Hoff, E. ÅdnaneS, D. Schanke, and A. Holmen, “Fischer-Tropsch synthesis on supported cobalt catalysts promoted by platinum and rhenium,” *Top. Catal.*, vol. 2, no. 1–4, pp. 155–162, Mar. 1995.

[26] F. Diehl and A. Y. Khodakov, “Promotion of Cobalt Fischer-Tropsch catalysts with noble metals: A review,” *Oil and Gas Science and Technology*, vol. 64, no. 1. EDP Sciences, pp. 11–24, 01-Jan-2009.

[27] D. Nabaho, J. W. Niemantsverdriet, M. Claeys, and E. Van Steen, “Hydrogen spillover in the Fischer-Tropsch synthesis: An analysis of platinum as a promoter for cobalt-alumina catalysts,” *Catal. Today*, vol. 261, pp. 17–27, Mar. 2016.

[28] G. Jacobs, Y. Ji, B. H. Davis, D. Cronauer, A. J. Kropf, and C. L. Marshall, “Fischer-Tropsch synthesis: Temperature programmed EXAFS/XANES investigation of the influence of support type, cobalt loading, and noble metal promoter addition to the reduction behavior of cobalt oxide particles,” *Appl. Catal. A Gen.*, vol. 333, no. 2, pp. 177–191, Dec. 2007.

[29] J. S. Ledford, M. Houalla, A. Proctor, D. M. Hercules, and L. Petrakis, “Influence of lanthanum on the surface structure and CO hydrogenation acitivity of supported cobalt catalysts,” *J. Phys. Chem.*, vol. 93, no. 18, pp. 6770–6777, 1989.

[30] M. R. Hemmati, M. Kazemeini, J. Zarkesh, and F. Khorasheh, “Effect of lanthanum doping on the lifetime of Co/γ-Al 2O 3 catalysts in Fischer-Tropsch synthesis,” *J. Taiwan Inst. Chem. Eng.*, vol. 43, no. 5, pp. 704–710, Sep. 2012.

[31] B. A. Sexton, A. E. Hughes, and T. W. Turney, “An XPS and TPR study of the reduction of promoted cobalt-kieselguhr Fischer-Tropsch catalysts,” *J. Catal.*, vol. 97, no. 2, pp. 390–406, Feb. 1986.

[32] M. Schmal, D. A. G. Aranda, R. R. Soares, F. B. Noronha, and A. Frydman, “A study of

the promoting effect of noble metal addition on niobia and niobia alumina catalysts," *Catal. Today*, vol. 57, no. 3–4, pp. 169–176, Apr. 2000.

[33] G. R. Moradi, M. M. Basir, A. Taeb, and A. Kiennemann, "Promotion of Co/SiO2 Fischer-Tropsch catalysts with zirconium," *Catal. Commun.*, vol. 4, no. 1, pp. 27–32, Jan. 2003.

[34] L. Xu *et al.*, "The promotions of MnO and K2O to Fe/silicalite-2 catalyst for the production of light alkenes from CO2 hydrogenation," *Appl. Catal. A Gen.*, vol. 173, no. 1, pp. 19–25, Oct. 1998.

[35] C. K. Das, N. S. Das, D. P. Choudhury, G. Ravichandran, and D. K. Chakrabarty, "Hydrogenation of carbon monoxide on unsupported Fe-Mn-K catalysts for the synthesis of lower alkenes: promoter effect of manganese," *Appl. Catal. A, Gen.*, vol. 111, no. 2, pp. 119–132, Apr. 1994.

[36] S. T. Hussain, "Temperature-Programmed Desorption (Tpd) and Temperature-Programmed Reduction (Tpr) Studies of Alumina-Supported Ploycrystalline Ru/Mn Bimetallic System," *J. Chem. Soc. Pakistan*, vol. 15, no. 4, p. 110, 2011.

[37] G. L. Bezemer *et al.*, "Investigation of promoter effects of manganese oxide on carbon nanofiber-supported cobalt catalysts for Fischer-Tropsch synthesis," *J. Catal.*, vol. 237, no. 1, pp. 152–161, Jan. 2006.

[38] F. Morales, E. de Smit, F. M. F. de Groot, T. Visser, and B. M. Weckhuysen, "Effects of manganese oxide promoter on the CO and H2 adsorption properties of titania-supported cobalt Fischer-Tropsch catalysts," *J. Catal.*, vol. 246, no. 1, pp. 91–99, Feb. 2007.

[39] G. R. Johnson, S. Werner, and A. T. Bell, "An Investigation into the Effects of Mn Promotion on the Activity and Selectivity of Co/SiO 2 for Fischer−Tropsch Synthesis: Evidence for Enhanced CO Adsorption and Dissociation," *ACS Catal.*, vol. 5, no. 10, pp. 5888–5903, Oct. 2015.

[40] M. Van Doorslaer, M. Saeys, and G. T. K. K. Gunasooriya, "Elucidating the role of Mn promotion in Co-based Fischer-Tropsch synthesis Maarten Van Doorslaer," Ghent University, 2017.

[41] M. Gençoğlu, "Effects of manganese promotion on reactants and intermediates of Fischer Tropsch Synthesis on a model cobalt surface-a Density Functional Theory investigation," İzmir Institute of Technology, 2019.

[42] R. M. Martin, *Electronic Structure: Basic Theory and Practical Methods*. Cambridge University Press, 2004.

[43] E. Schrödinger, "An undulatory theory of the mechanics of atoms and molecules," *Phys. Rev.*, vol. 28, no. 6, pp. 1049–1070, Dec. 1926.

[44] M. Born and R. Oppenheimer, "Zur Quantentheorie der Molekeln," *Ann. Phys.*, vol. 389, no. 20, pp. 457–484, Jan. 1927.

[45] Peter W. Atkins and R. S. Friedman, *Molecular Quantum Mechanics*, 5th ed. Oxford: Oxford University Press, 2010.

[46] D. R. Hartree, "The Wave Mechanics of an Atom with a Non-Coulomb Central Field Part II Some Results and Discussion," *Math. Proc. Cambridge Philos. Soc.*, vol. 24, no. 1, pp. 111–132, 1928.

[47] J. C. Slater, "A simplification of the Hartree-Fock method," *Phys. Rev.*, vol. 81, no. 3, pp. 385–390, Feb. 1951.

[48] D. L. Strout and G. E. Scuseria, "A quantitative study of the scaling properties of the Hartree-Fock method," *J. Chem. Phys.*, vol. 102, no. 21, pp. 8448–8452, Jun. 1995.

[49] P. Hohenberg and W. Kohn, "Inhomogeneous electron gas," *Phys. Rev.*, vol. 136, no.

3B, p. B864, Nov. 1964.
[50] W. Kohn and L. J. Sham, “Self-consistent equations including exchange and correlation effects,” *Phys. Rev.*, vol. 140, no. 4A, pp. A1133–A1138, Nov. 1965.
[51] G. Kresse and J. Hafner, “Ab Initio Molecular Dynamcis for Liquid Metals.,” *Phys. Rev. B*, vol. 47, no. 1, p. 558, 1993.
[52] G. Kresse and J. Furthmüller, “Efficient iterative schemes for ab initio total-energy calculations using a plane-wave basis set,” *Phys. Rev. B - Condens. Matter Mater. Phys.*, vol. 54, no. 16, pp. 11169–11186, Oct. 1996.
[53] D. Joubert, G. Kresse, and D. Joubert, “From ultrasoft pseudopotentials to the projector augmented-wave method,” *Phys. Rev. B - Condens. Matter Mater. Phys.*, vol. 59, no. 3, pp. 1758–1775, Jan. 1999.
[54] G. Kresse, “The PAW and US-PP database,” *PowerPoint*, 2005.
[55] S. J. Clark *et al.*, “First principles methods using CASTEP,” *Zeitschrift fur Krist.*, vol. 220, no. 5–6, pp. 567–570, May 2005.
[56] J. M. Soler *et al.*, “The SIESTA method for ab initio order-N materials simulation,” *J. Phys. Condens. Matter*, vol. 14, no. 11, pp. 2745–2779, Mar. 2002.
[57] L. H. Thomas, “The calculation of atomic fields,” *Math. Proc. Cambridge Philos. Soc.*, vol. 23, no. 5, pp. 542–548, 1927.
[58] E. Fermi, “Statistical method to determine some properties of atoms,” *Rend. Accad. Naz. Lincei*, vol. 6, no. December, pp. 602–607, 1927.
[59] J. F. Janak, “Proof that ∂E∂ni=ε in density-functional theory,” *Phys. Rev. B*, vol. 18, no. 12, pp. 7165–7168, Dec. 1978.
[60] P. A. M. Dirac, “Note on Exchange Phenomena in the Thomas Atom,” *Math. Proc. Cambridge Philos. Soc.*, vol. 26, no. 3, pp. 376–385, 1930.
[61] J. H. Hetherington, “Observations on the statistical iteration of matrices,” *Phys. Rev. A*, vol. 30, no. 5, pp. 2713–2719, Nov. 1984.
[62] A. D. Becke, “Perspective: Fifty years of density-functional theory in chemical physics,” *J. Chem. Phys.*, vol. 140, no. 18, p. 18A301, Apr. 2014.
[63] J. P. Perdew, K. Burke, and M. Ernzerhof, “Generalized gradient approximation made simple,” *Phys. Rev. Lett.*, vol. 77, no. 18, pp. 3865–3868, Oct. 1996.
[64] J. P. Perdew *et al.*, “Atoms, molecules, solids, and surfaces: Applications of the generalized gradient approximation for exchange and correlation,” *Phys. Rev. B*, vol. 46, no. 11, pp. 6671–6687, Sep. 1992.
[65] B. Hammer, L. B. Hansen, and J. K. Nørskov, “Improved adsorption energetics within density-functional theory using revised Perdew-Burke-Ernzerhof functionals,” *Phys. Rev. B - Condens. Matter Mater. Phys.*, vol. 59, no. 11, pp. 7413–7421, Mar. 1999.
[66] W. Kohn, “Nobel lecture: Electronic structure of matter - Wave functions and density functional,” *Rev. Mod. Phys.*, vol. 71, no. 5, pp. 1253–1266, Oct. 1999.
[67] T. van Heerden and E. van Steen, “Metal–support interaction on cobalt based FT catalysts – a DFT study of model inverse catalysts,” *Faraday Discuss.*, vol. 197, pp. 87–99, 2017.
[68] S. Govender, T. G. Gambu, T. van Heerden, and E. van Steen, “Mechanistic pathways for oxygen removal on Pt-doped Co(111) in the Fischer-Tropsch reaction,” *Catal. Today*, vol. 342, pp. 142–151, Feb. 2020.
[69] H. J. Monkhorst and J. D. Pack, “Special points for Brillouin-zone integrations,” *Phys. Rev. B*, vol. 13, no. 12, pp. 5188–5192, Jun. 1976.
[70] P. Van Helden and I. M. Ciobëcă, “A DFT study of carbon in the subsurface layer of

cobalt surfaces," *ChemPhysChem*, vol. 12, no. 16, pp. 2925–2928, Nov. 2011.

[71] P. Van Helden, J. A. Van Den Berg, and C. J. Weststrate, "Hydrogen adsorption on co surfaces: A density functional theory and temperature programmed desorption study," *ACS Catal.*, vol. 2, no. 6, pp. 1097–1107, 2012.

[72] G. Kresse, M. Marsman, and Jürgen Furthmüller, "VASP the Guide," Vienna, Austria, 2018.

[73] F. Birch, "Finite Elastic Strain of Cubic Crystals*," *Phys. Rev.*, vol. 71, no. 11, pp. 809–824, 1947.

[74] N. W. Ashcroft and N. D. Mermin, *Solid state physics*, vol. 9, no. 1. Wiley, 1976.

[75] M. J. Mehl and D. A. Papaconstantopoulos, "Applications of a tight-binding total-energy method for transition and noble metals: Elastic constants, vacancies, and surfaces of monatomic metals," *Phys. Rev. B - Condens. Matter Mater. Phys.*, vol. 54, no. 7, pp. 4519–4530, 1996.

[76] A. R. West, *Solid State Chemistry and its Applications, 2nd Edition, Student Edition*. New York: Wiley, 2014.

[77] P. Van Helden, J. A. Van Den Berg, M. A. Petersen, W. Janse Van Rensburg, I. M. Ciobîcă, and J. Van De Loosdrecht, "Computational investigation of the kinetics and mechanism of the initial steps of the Fischer-Tropsch synthesis on cobalt," *Faraday Discuss.*, vol. 197, no. 0, pp. 117–151, 2017.

[78] J. Cheng, P. Hu, P. Ellis, S. French, G. Kelly, and C. M. Lok, "A DFT study of the transition metal promotion effect on ethylene chemisorption on Co(0 0 0 1)," *Surf. Sci.*, vol. 603, no. 17, pp. 2752–2758, 2009.

[79] Z. Zhang, Y. Li, C. Hou, C. Zhao, and Z. Ke, "DFT study of CO2 hydrogenation catalyzed by a cobalt-based system: An unexpected formate anion-assisted deprotonation mechanism," *Catal. Sci. Technol.*, vol. 8, no. 2, pp. 656–666, Jan. 2018.

[80] F. Borji, A. N. Pour, J. Karimi, M. Izadyar, Z. Keyvanloo, and M. Hashemian, "The molecular adsorption of carbon monoxide on cobalt surfaces: A DFT study," *Prog. React. Kinet. Mech.*, vol. 42, no. 1, pp. 89–98, Feb. 2017.

[81] C. Chen *et al.*, "High coverage CO adsorption and dissociation on the Co(0001) and Co(100) surfaces from DFT and thermodynamics," *Appl. Catal. A Gen.*, vol. 523, pp. 209–220, Aug. 2016.

[82] M. Rahal, M. Hilali, A. El Hammadi, M. El Mouhtadi, and A. El Hajbi, "Calculation of vibrational zero-point energy," *J. Mol. Struct. THEOCHEM*, vol. 572, no. 1–3, pp. 73–80, Sep. 2001.

[83] K. K. Irikura, "Computational Thermochemistry: Prediction and Estimation of Molecular Thermodynamics; National Institute of Standards and Technology," *ACS Symposium Series*, vol. 677. American Chemical Society, 1995.

[84] S. I. Sandler, *Chemical, Biochemical, and Engineering Thermodynamics*, 5th Editio. Wiley, 2017.

[85] G. Henkelman, B. P. Uberuaga, and H. Jónsson, "Climbing image nudged elastic band method for finding saddle points and minimum energy paths," *J. Chem. Phys.*, vol. 113, no. 22, pp. 9901–9904, Dec. 2000.

[86] D. Sheppard, R. Terrell, and G. Henkelman, "Optimization methods for finding minimum energy paths," *J. Chem. Phys.*, vol. 128, no. 13, p. 134106, Apr. 2008.

[87] D. Sheppard and G. Henkelman, "Paths to which the nudged elastic band converges," *J. Comput. Chem.*, vol. 32, no. 8, pp. 1769–1771, Jun. 2011.

[88] G. Henkelman and H. Jónsson, "A dimer method for finding saddle points on high

dimensional potential surfaces using only first derivatives," *J. Chem. Phys.*, vol. 111, no. 15, pp. 7010–7022, Oct. 1999.

[89] A. Heyden, A. T. Bell, and F. J. Keil, "Efficient methods for finding transition states in chemical reactions: Comparison of improved dimer method and partitioned rational function optimization method," *J. Chem. Phys.*, vol. 123, no. 22, p. 224101, Dec. 2005.

[90] G. Henkelman and H. Jónsson, "Nudged Elastic Band — Transition State Tools for VASP." [Online]. Available: https://theory.cm.utexas.edu/vtsttools/neb.html#id3. [Accessed: 18-Sep-2021].

[91] P. Xiao, D. Sheppard, J. Rogal, and G. Henkelman, "Solid-state dimer method for calculating solid-solid phase transitions," *J. Chem. Phys.*, vol. 140, no. 17, p. 174104, May 2014.

[92] H. Eyring, "The activated complex in chemical reactions," *J. Chem. Phys.*, vol. 3, no. 2, pp. 63–71, Nov. 1935.

[93] C. J. Weststrate, P. Van Helden, J. Van De Loosdrecht, and J. W. Niemantsverdriet, "Elementary steps in Fischer-Tropsch synthesis: CO bond scission, CO oxidation and surface carbiding on Co(0001)," *Surf. Sci.*, vol. 648, pp. 60–66, 2016.

[94] J. X. Liu, H. Y. Su, D. P. Sun, B. Y. Zhang, and W. X. Li, "Crystallographic dependence of CO activation on cobalt catalysts: HCP versus FCC," *J. Am. Chem. Soc.*, vol. 135, no. 44, pp. 16284–16287, Nov. 2013.

[95] W. Chen, B. Zijlstra, I. A. W. Filot, R. Pestman, and E. J. M. Hensen, "Mechanism of Carbon Monoxide Dissociation on a Cobalt Fischer-Tropsch Catalyst," *ChemCatChem*, vol. 10, no. 1, pp. 136–140, 2018.

[96] A. C. Kizilkaya, J. W. Niemantsverdriet, and C. J. Weststrate, "Oxygen Adsorption and Water Formation on Co(0001)," *J. Phys. Chem. C*, vol. 120, no. 9, pp. 4833–4842, 2016.

[97] A. M. Saib, M. Claeys, E. Van Steen, and E. Van Steen, "Silica supported cobalt Fischer-Tropsch catalysts: Effect of pore diameter of support," *Catal. Today*, vol. 71, no. 3–4, pp. 395–402, Jan. 2002.

[98] O. Kitakami, H. Sato, Y. Shimada, F. Sato, and M. Tanaka, "Size effect on the crystal phase of cobalt fine particles," *Phys. Rev. B - Condens. Matter Mater. Phys.*, vol. 56, no. 21, pp. 13849–13854, 1997.

[99] B. Yang, R. Burch, C. Hardacre, G. Headdock, and P. Hu, "Understanding the optimal adsorption energies for catalyst screening in heterogeneous catalysis," *ACS Catal.*, vol. 4, no. 1, pp. 182–186, Jan. 2014.

[100] H. Tang, A. Van Der Ven, and B. L. Trout, "Lateral interactions between oxygen atoms adsorbed on platinum (111) by first principles," *Mol. Phys.*, vol. 102, no. 3 PART II, pp. 273–279, 2004.

[101] A. N. Dobrotvorskaia, O. S. Pestsov, and A. A. Tsyganenko, "Lateral Interaction between Molecules Adsorbed on the Surfaces of Non-Metals," *Top. Catal.*, vol. 60, no. 19–20, pp. 1506–1521, 2017.

[102] A. J. R. Hensley *et al.*, "DFT-Based Method for More Accurate Adsorption Energies: An Adaptive Sum of Energies from RPBE and vdW Density Functionals," *J. Phys. Chem. C*, vol. 121, no. 9, pp. 4937–4945, Mar. 2017.

[103] J. Wellendorff *et al.*, "A benchmark database for adsorption bond energies to transition metal surfaces and comparison to selected DFT functionals," *Surf. Sci.*, vol. 640, pp. 36–44, Oct. 2015.

[104] H. Schulz, M. Claeys, and S. Harms, "Effect of water partial pressure on steady state Fischer-Tropsch activity and selectivity of a promoted cobalt catalyst," *Stud. Surf. Sci.*

Catal., vol. 107, pp. 193–200, 1997.
[105] R. F. W. Bader, Y. Tal, S. G. Anderson, and T. T. Nguyen-Dang, “Quantum Topology: Theory of Molecular Structure and its Change,” *Isr. J. Chem.*, vol. 19, no. 1–4, pp. 8–29, Jan. 1980.
[106] M. Yu and D. R. Trinkle, “Accurate and efficient algorithm for Bader charge integration,” *J. Chem. Phys.*, vol. 134, no. 6, p. 64111, 2011.
[107] G. Henkelman, A. Arnaldsson, and H. Jónsson, “A fast and robust algorithm for Bader decomposition of charge density,” *Comput. Mater. Sci.*, vol. 36, no. 3, pp. 354–360, 2006.
[108] E. Sanville, S. D. Kenny, R. Smith, and G. Henkelman, “Improved grid-based algorithm for Bader charge allocation,” *J. Comput. Chem.*, vol. 28, no. 5, pp. 899–908, 2007.
[109] W. Tang, E. Sanville, and G. Henkelman, “A grid-based Bader analysis algorithm without lattice bias,” *J. Phys. Condens. Matter*, vol. 21, no. 8, pp. 84204–84211, 2009.
[110] T. A. Manz and N. G. Limas, “Introducing DDEC6 atomic population analysis: Part 1. Charge partitioning theory and methodology,” *RSC Adv.*, vol. 6, no. 53, pp. 47771–47801, May 2016.
[111] T. A. Manz and N. G. Limas, “DDEC6: A Method for Computing Even-Tempered Net Atomic Charges in Periodic and Nonperiodic Materials,” 2015.
[112] N. G. Limas and T. A. Manz, “Introducing DDEC6 atomic population analysis: Part 4. Efficient parallel computation of net atomic charges, atomic spin moments, bond orders, and more,” *RSC Adv.*, vol. 8, no. 5, pp. 2678–2707, Jan. 2018.
[113] N. G. Limas and T. A. Manz, “Introducing DDEC6 atomic population analysis: Part 2. Computed results for a wide range of periodic and nonperiodic materials,” *RSC Adv.*, vol. 6, no. 51, pp. 45727–45747, May 2016.
[114] T. A. Manz and N. G. Limas, “Chargemol program for performing DDEC atomic population analysis.” 2017.
[115] E. Van Steen, M. Claeys, M. E. Dry, J. Van De Loosdrecht, E. L. Viljoen, and J. L. Visagie, “Stability of nanocrystals: Thermodynamic analysis of oxidation and re-reduction of cobalt in water/hydrogen mixtures,” *J. Phys. Chem. B*, vol. 109, no. 8, pp. 3575–3577, Mar. 2005.
[116] W. Warayanon, S. Tungkamani, H. Sukkathanyawat, M. Phongaksorn, T. Ratana, and T. Sornchamni, “Effect of Manganese Promoter on Cobalt Supported Magnesia Catalyst for Fischer-Tropsch Synthesis,” in *Energy Procedia*, 2015, vol. 79, pp. 163–168.
[117] E. Ø. Pedersen and E. A. Blekkan, “Noble Metal Promoted CoMn Catalysts for Fischer–Tropsch Synthesis,” *Catal. Letters*, vol. 148, no. 4, pp. 1027–1034, Apr. 2018.
[118] B. Zijlstra, R. J. P. Broos, W. Chen, H. Oosterbeek, I. A. W. Filot, and E. J. M. Hensen, “Coverage Effects in CO Dissociation on Metallic Cobalt Nanoparticles,” *ACS Catal.*, vol. 9, no. 8, pp. 7365–7372, Aug. 2019.
[119] X. Q. Gong, R. Raval, and P. Hu, “CO dissociation and O removal on Co(0 0 0 1): A density functional theory study,” *Surf. Sci.*, vol. 562, no. 1–3, pp. 247–256, Aug. 2004.
[120] N. Balakrishnan, B. Joseph, and V. R. Bhethanabotla, “Effect of platinum promoters on the removal of O from the surface of cobalt catalysts: A DFT study,” *Surf. Sci.*, vol. 606, no. 5–6, pp. 634–643, Mar. 2012.
[121] S. Liu, Y.-W. Li, J. Wang, and H. Jiao, “Mechanisms of H2O and CO2 Formation from Surface Oxygen Reduction on Co(0001),” *J. Phys. Chem. C*, vol. 120, no. 34, pp. 19265–19270, Sep. 2016.
[122] K. Momma and F. Izumi, “VESTA 3 for three-dimensional visualization of crystal,

volumetric and morphology data," *J. Appl. Crystallogr.*, vol. 44, no. 6, pp. 1272–1276, Dec. 2011.

[123] T. Chen and T. A. Manz, "Bond orders of the diatomic molecules," *RSC Adv.*, vol. 9, no. 30, pp. 17072–17092, 2019.

[124] T. A. Manz, "Introducing DDEC6 atomic population analysis: Part 3. Comprehensive method to compute bond orders," *RSC Adv.*, vol. 7, no. 72, pp. 45552–45581, 2017.

[125] M. Zhuo, K. F. Tan, A. Borgna, and M. Saeys, "Density functional theory study of the co insertion mechanism for Fischer-Tropsch synthesis over co catalysts," *J. Phys. Chem. C*, vol. 113, no. 19, pp. 8357–8365, May 2009.

[126] X.-Q. Gong, R. Raval, and P. Hu, "CO dissociation and O removal on Co(0 0 0 1): a density functional theory study," *Surf. Sci.*, vol. 562, no. 1–3, pp. 247–256, Aug. 2004.

[127] X.-Q. Gong, R. Raval, and P. Hu, "CHx hydrogenation on Co(0001): A density functional theory study," *J. Chem. Phys.*, vol. 122, no. 2, p. 024711, Jan. 2005.

[128] N. Balakrishnan, B. Joseph, and V. R. Bhethanabotla, "Effect of Pt and Ru promoters on deactivation of Co catalysts by C deposition during Fischer-Tropsch synthesis: A DFT study," *Appl. Catal. A Gen.*, vol. 462–463, pp. 107–115, Jul. 2013.

[129] I. A. W. Filot, R. A. Van Santen, and E. J. M. Hensen, "The optimally performing Fischer-Tropsch catalyst," *Angew. Chemie - Int. Ed.*, vol. 53, no. 47, pp. 12746–12750, Nov. 2014.

Appendix

A. Computational Method

A.1 Sample calculation input files

[A]

```
# General Setup
  System = Co_111_CO    # Define working system
  GGA    = RP
  PREC   = Accurate   # Options: Accurate, Normal, Medium, High, Low
  ENCUT  = 400        # Kinetic Energy Cutoff in eV
  ISTART = 0          # Job: 0-new  1-cont  2-samecut
  ICHARG = 2          # initial charge density: 1-file 2-atom 10-cons 11-DOS
  ISPIN  = 2          # Spin Polarize: 1-No 2-Yes
  MAGMOM = 1*1.0 1*1.0 80*2.0     # Using a higher MAGMOM than 1.5
  LCHARG = .False.    # do not write CHGCAR
  LWAVE  = .False.    # do not write WAVECAR
  MAXMIX = 150

# Electronic Relaxation (SCF)
  NELM     = 100       # Max Number of Elec Self Cons Steps
    NELMIN = 2         # Min Number of ESC steps
    NELMDL = -12       # Number of non-SC at the beginning, negative for surfaces
  EDIFF    = 1.0E-05  # Stopping criteria for ESC
  LREAL    = Auto     # Real space projection. Auto for system with more than 8 atoms
  ALGO     = Fast     # Electronic algorithm minimization

# Ionic Relaxation
  EDIFFG   = -1.0E-02    # Stopping criteria for ionic self cons steps
  NSW      = 600         # Max Number of ISC steps: 0- Single Point
  IBRION   = 2           # Ionic Relaxation Method: 0-MD 1-qNewton-RaphsonElectronic 2-CG
#no stress tensor calculations
  ISIF     = 2           # Stress and Relaxation: 2-Ion 3-cell+ion
  POTIM    = 0.5         # scaling constant, 0.5 for for IBRION=1,2,3 and 5
  SIGMA    = 0.05         # Insulators/semiconductors=0.1  metals=0.05
  ISMEAR   = 0          # Partial Occupancies for each Orbital
                         # -5 DOS, -2 from file, -1 Fermi Smear, 0 Gaussian Smear
# Parallelization
  NCORE    = 20
  LPLANE   = .TRUE.
  LSCALU   = .FALSE.
  NSIM     = 4
```

[B]

```
# Electronic Relaxation (SCF)
  NELM     = 100       # Max Number of Elec Self Cons Steps
    NELMIN = 2         # Min Number of ESC steps
    NELMDL = -12       # Number of non-SC at the beginning, negative for surfaces
  EDIFF    = 1.0E-06  # Stopping criteria for ESC
  LREAL    = Auto     # Real space projection. Auto for system with more than 8 atoms
  ALGO     = Fast     # Electronic algorithm minimization

# Ionic Relaxation
  EDIFFG   = -1.0E-02    # Stopping criteria for ionic self cons steps
  NSW      = 600         # Max Number of ISC steps: 0- Single Point
  IBRION   = 5           # Ionic Relaxation Method: 0-MD 1-qNewton-RaphsonElectronic 2-CG
#no stress tensor calculations
  ISIF     = 2           # Stress and Relaxation: 2-Ion 3-cell+ion
  POTIM    = 0.015         # scaling constant, 0.5 for for IBRION=1,2,3 and 5
  SIGMA    = 0.05         # Insulators/semiconductors=0.1  metals=0.05
  ISMEAR   = 0          # Partial Occupancies for each Orbital
                         # -5 DOS, -2 from file, -1 Fermi Smear, 0 Gaussian Smear
```

Figure A.1-1: Sample VASP INCAR file for [A] optimisation of geometries, [B] vibrational analysis

[A]

```
# Ionic Relaxation
  EDIFFG   = -1.0E-02    # Stopping criteria for ionic self cons steps
  NSW      = 0           # Max Number of ISC steps: 0- Single Point
  IBRION   = 2           # Ionic Relaxation Method: 0-MD 1-qNewton-RaphsonElectronic 2-CG
#no stress tensor calculations
  ISIF     = 2           # Stress and Relaxation: 2-Ion 3-cell+ion
  POTIM    = 0.5         # scaling constant, 0.5 for for IBRION=1,2,3 and 5
  SIGMA    = 0.05         # Insulators/semiconductors=0.1  metals=0.05
  ISMEAR   = 0          # Partial Occupancies for each Orbital
                         # -5 DOS, -2 from file, -1 Fermi Smear, 0 Gaussian Smear
# NEB
  IMAGES  = 8
  ISYM    = 0
  SPRING  = -5
  IOPT    = 7
  LCLIMB = .TRUE. #CI_NEB
```

[B]

```
# Ionic Relaxation
  EDIFFG   = -1.0E-02    # Stopping criteria for ionic self cons steps
  NSW      = 600         # Max Number of ISC steps: 0- Single Point
  IBRION   = 3           # Ionic Relaxation Method: 0-MD 1-qNewton-RaphsonElectronic 2-CG 3-Molecular Dynamics(DIMER calc)
#no stress tensor calculations
  ISIF     = 2           # Stress and Relaxation: 2-Ion 3-cell+ion
  POTIM    = 0         # scaling constant, 0.5 for for IBRION=1,2,3 and 5, 0 for DIMER
  SIGMA    = 0.05         # Insulators/semiconductors=0.1  metals=0.05
  ISMEAR   = 0          # Partial Occupancies for each Orbital
                         # -5 DOS, -2 from file, -1 Fermi Smear, 0 Gaussian Smear
# DIMER
  ICHAIN  = 2
  DdR     = 0.005
  DRotMax = 1
  DFNMin  = 0.01
  DFNMin  = 1.0
# Optimisers
  IOPT    = 2
```

Figure A.1-2: Modification of the INCAR files for [A] cNEB calculations, [B] DIMER calculations

B. Adsorption of species on Co(111)

B.1 Vibrational modes for lowest energy configurations

Table B.1-1Vibrational frequencies in cm^{-1} of C, CO, H, O, OH and H2O on Co(111)

C	CO	H	O	OH	H_2O
477.30699	127.10631	834.14292	343.92392	243.17850	22.85334
477.68802	129.36325	841.58855	347.75479	250.59303	68.71913
563.72389	214.71730	1099.63421	466.64197	388.15331	82.06949
	215.66979			487.34101	125.95642
	320.39617			490.77423	385.77228
	1718.13797			3706.87571	389.76767
					1568.81537
					3615.76300
					3728.51847

Table B.1-2: Vibrational frequencies in cm^{-1} of optimised MnO_x ligands on Co(111)

MnO	MnO_2	MnO(OH)	MnO_3	MnO_2(OH)	$MnO(OH)_2$
25.48236	104.29497	80.65499	120.69550	46.27753	76.36722
123.92032	147.52530	107.21895	124.01666	80.28197	102.01273
183.92301	196.76737	122.32831	154.80163	107.09676	116.72380
228.76123	237.88598	165.96403	169.78128	145.83203	137.51179
353.07582	262.07135	194.80823	216.52852	158.59399	166.52993
413.94518	342.40581	263.37151	218.37620	251.91150	217.12104
	363.91214	373.05866	307.96161	277.69545	226.43466
	466.62774	451.74801	309.75611	287.11710	274.48457
	477.02558	510.99200	337.50670	369.83091	365.56215
		540.19993	497.24977	375.10003	387.78552
		628.89171	497.47648	410.50356	403.73583
		3701.71321	567.93143	430.40748	481.98118
				628.83114	505.82745
				693.32438	587.40482
				3714.54086	679.66710
					692.78016
					3670.03973
					3676.52802

C. Adsorption of Species on MnO_x promoted Co(111)

C.1 Vibrational modes for lowest energy configurations

Table C.1-1: Vibrational frequencies in cm^{-1} of C, CO, H, O, OH and H_2O on OMn promoted Co(111)

C	CO	H	O	OH	H_2O
101.37451	76.53446	70.87805	104.29497	80.65499	43.66033
141.24548	130.32359	123.83053	147.52530	107.21895	86.59334
186.87559	144.20194	187.20408	196.76737	122.32831	103.17120
198.52977	177.55268	232.25079	237.88598	165.96403	120.83586
280.10987	243.27942	360.07948	262.07135	194.80823	171.72250
336.24981	271.22296	397.02738	342.40581	263.37151	195.45912
472.97483	346.54483	467.61741	363.91214	373.05866	242.67849
475.26598	352.95984	872.80244	466.62774	451.74801	317.50100
660.69815	380.23317	1121.36590	477.02558	510.99200	354.46379
	439.35109			540.19993	503.74909
	525.97066			628.89171	561.25464
	1350.03670			3701.71321	604.84485
					1558.56829
					3259.52013
					3666.32670

Table C.1-2: Vibrational frequencies in cm^{-1} of C, CO, H, O, OH and H_2O on O_2Mn promoted Co(111)

C	CO	H	O	OH	H_2O
128.82448	102.02890	101.13954	120.69550	46.27753	2.72389
155.96563	111.09488	147.44035	124.01666	80.28197	45.91007
203.11413	150.93592	194.79366	154.80163	107.09676	56.25180
230.75440	170.41616	235.85673	169.78128	145.83203	90.19109
258.31814	212.08712	262.13542	216.52852	158.59399	147.14600
340.60538	250.93418	340.75055	218.37620	251.91150	166.13741
358.22434	270.53542	363.61004	307.96161	277.69545	237.40549
400.65176	291.43580	470.45538	309.75611	287.11710	245.87058
412.58943	311.94155	479.90594	337.50670	369.83091	260.32005
449.76814	373.77477	788.09936	497.24977	375.10003	343.41813
459.81467	386.16252	900.83931	497.47648	410.50356	358.94891
613.26229	405.25279	1110.50878	567.93143	430.40748	438.98750
	422.30784			628.83114	459.35856
	435.08136			693.32438	465.67468
	1514.58190			3714.54086	507.61425
					1594.70677
					3634.81019
					3730.20452

D. Microkinetic Model

D.1 Transition States

$O^* + H^* \leftrightarrow OH^* + {}^*$	$OH^* + OH^* \leftrightarrow H_2O^* + O^*$	$OH^* + H^* \leftrightarrow H_2O^* + {}^*$
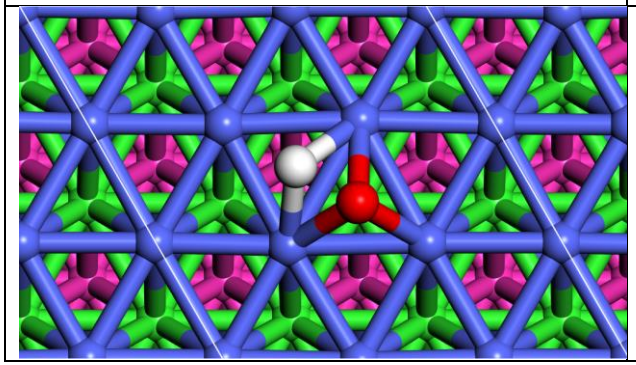	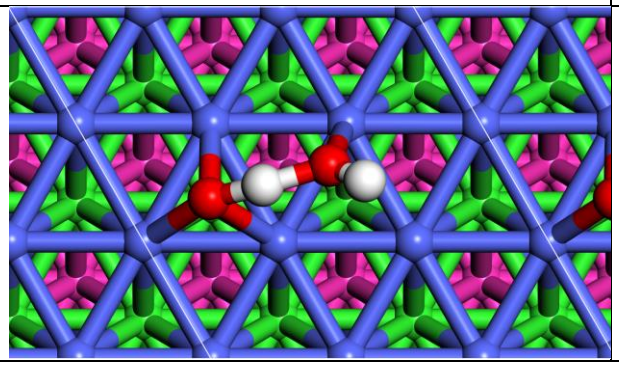	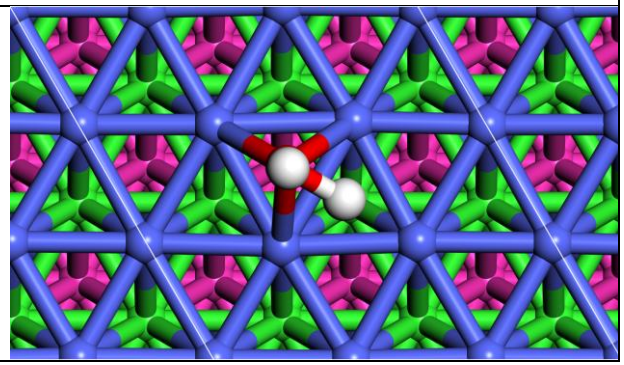

$O_2Mn + H^* \leftrightarrow OMn(OH) + {}^*$	$OMn(OH) + OH^* \leftrightarrow OMn(H_2O) + O^*$	$OMn(H_2O) + O^* \leftrightarrow O_2Mn(H_2O) + {}^*$
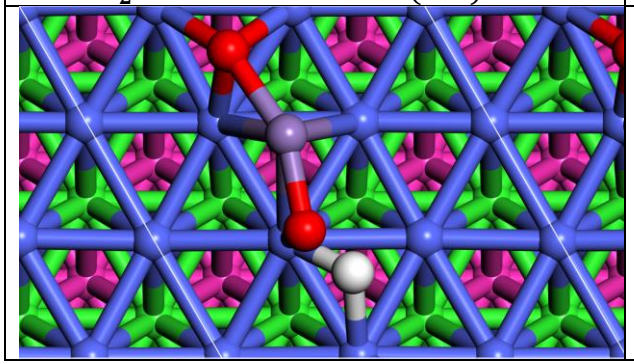	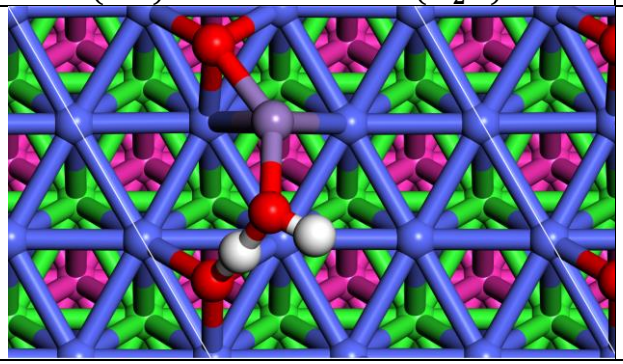	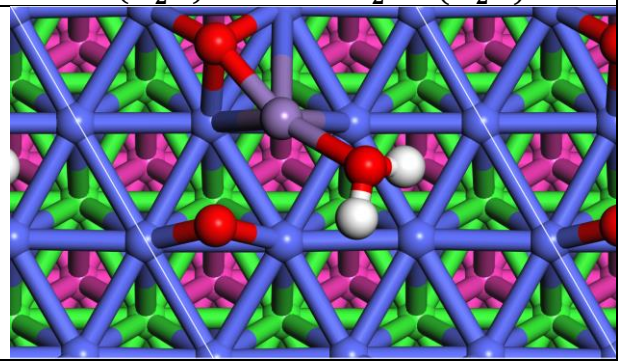

$OMn + O^* \leftrightarrow O_2Mn + ^*$	$O_2Mn + OH^* \leftrightarrow O_2Mn(OH) + ^*$	$O_2Mn(OH) + OH^* \leftrightarrow O_2Mn(H_2O) + O^*$
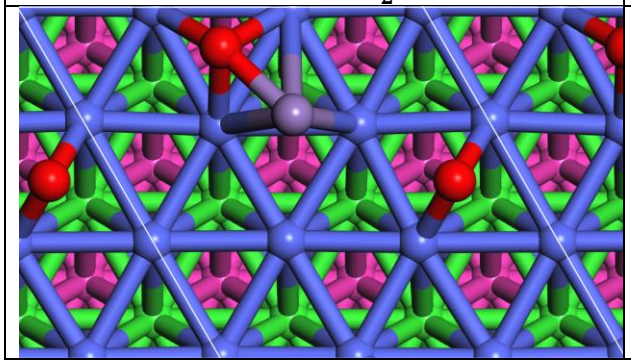	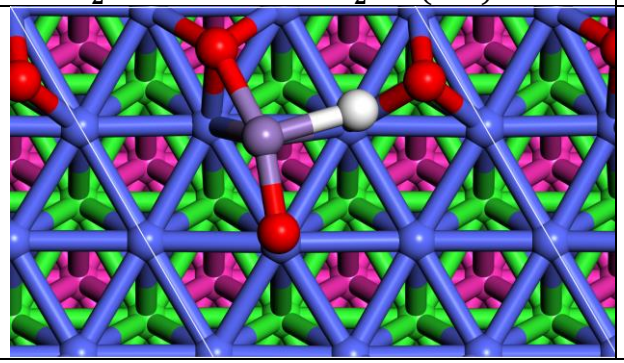	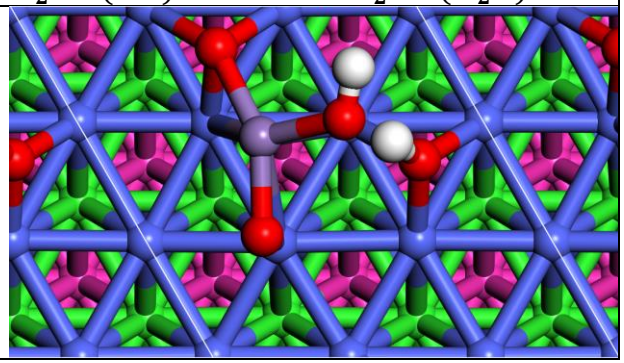

Figure D.1-1: Transition states for the reaction steps involved in the removal of oxygen on promoted p(3x3) Co(111)